

Tsz Chung Cheung

# The Relationship between Hydroxyl Content and Viscosity of Fused Silica for the Czochralski Process

June 2019







Norwegian University of  
Science and Technology

# The Relationship between Hydroxyl Content and Viscosity of Fused Silica for the Czochralski Process

**Tsz Chung Cheung**

Materials Science and Engineering

Submission date: June 2019

Supervisor: Kjell Wiik, IMA

Co-supervisor: Astrid Marie Flattum Mugerud, The Quartz Corp  
Paul Inge Dahl, SINTEF  
John Atle Bones, SINTEF

Norwegian University of Science and Technology  
Department of Materials Science and Engineering



## Preface

This master thesis was carried out as a part of the course, TMT4920 - Materials Technology, Master's Thesis, at the Department of Materials Science and Engineering, Gløshaugen, Norwegian University of Science and Technology during the spring semester of 2019. It was an extension of a previous project called "Next Generation of Quartz Crucible for Production of Czochralski Solar Cells", carried out in Autumn 2018. This project was carried out under the supervision from NTNU, SINTEF Industri, and The Quartz Corp.

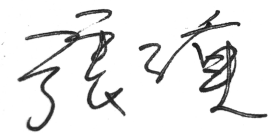
I would like to express my sincere gratitude to my supervisor, Professor Kjell Wiik at IMA, NTNU (Trondheim, Norway), for his professional guidance on this project. He has been providing useful guidance as well as sharing technical knowledge from his specialization background. I am also grateful to Astrid Marie Flattum Muggerud at The Quartz Corp (TQC) (Drag, Norway), for the permission to work with the interesting samples from TQC. Her advices and decisions made on different stages of this project are gratefully acknowledged. I also want to thank Paul Inge Dahl and John Atle Bones at SINTEF Industri (Trondheim, Norway) for their technical supports and helpful feedbacks throughout the project. The works from Ove Paulsen at SINTEF Industri, on building the setup for viscosity measurement, which is one of the cores of this project, must not be forgotten. The helps from Stein Rørvik SINTEF Industri (Trondheim, Norway), on the bubble characterization must also be acknowledged.

The technical advices and trainings of XRD, and different equipment involved provided by Babak Khalaghi, Kristin Høydalsvik Wells, Silje Marie Dale, Kara Poon and Mikalai Zhuk are also gratefully appreciated.

Last, but not least, I would like to thank all my classmates in Materialteknologi for these 2 wonderful years and my family for their supports.

Trondheim, June 2019

Tsz Chung Cheung



## Synopsis

High purity fused silica crucibles are commonly used in the production of monocrystalline silicon ingots with the Czochralski (CZ) process in the solar cell industry. Due to the formation of cristobalite at the CZ temperature, the crucibles are not reusable after the heating cycle. Consequently, a higher yield from each crucible is desired, leading to a demand of bigger fused silica crucible. Therefore, crucibles of higher quality and greater stability are needed. Understanding of some critical characteristics of the crucible material like the impurities and their influences is fundamental for improving the quality of the crucible.

The aim of this project has been to show the relationship between OH-content and viscosity of fused silica by data and to investigate the effect of drying parameters for quartz sand on the hydroxyl (OH) content and viscosity of fused silica. The importance of this project stems from the fact that these properties are critical for the performance of the crucible during the CZ process, while the existing studies are lacking the data from direct measurement of these properties. It is anticipated that either higher drying temperature and longer drying period will result in a lower OH-content and an increased viscosity of the fused silica.

A process involving both drying and melting of high purity quartz sands was established to produce fused silica samples based on combinations of different drying temperatures and periods. The OH-content and the viscosity of the samples were measured by FTIR spectrometer and a novel viscosity measurement setup respectively. The bubble distribution in the samples were also studied by Micro X-Ray computation tomography ( $\mu$ -CT).

The majority of the results aligns with the hypothesis that lower OH-content leads to a higher viscosity. A considerable difference in the OH-content was observed from the samples dried at different temperatures for a shorter period (i.e. 1 hour). The difference in OH-content was insignificant among samples dried for a longer period (i.e. 24 hours). The results are able to show the anticipated relationship between OH-content and viscosity. It highlights the importance of optimal drying parameters for quartz sands for the mechanical properties of fused silica, and, thus, the mechanical performance during CZ process.

## Sammendrag

Kvartsglass av høy kvalitet brukes i digler til produksjon av monokrystallinske silisium "ingots" i solcelleindustrien. Monokrystallinske wafere blir laget i slike digler ved Czochralski (CZ)-prosessen. Digelen kan ikke gjenbrukes etter en oppvarmingsyklus på grunn av dannelse av kristobalitt ved CZ-temperaturen. Det er ønskelig å maksimere utbytte per digel, noe som fører til etterspørsel etter større digler av kvartsglass. Derfor kreves en digel med høyere kvalitet og bedre stabilitet. Forståelsen av de kritiske karakteristikene til digelmaterialet, som for eksempel urenheter og hvordan disse påvirker viskositeten, er av fundamental betydning for å forbedre kvaliteten til digelen.

Hovedformålet med denne masteroppgaven har vært å undersøke effekten av tørkingsparametrene til kvartssand mht. hydroksyl(OH)-innhold og viskositet til kvartsglasset, samt vise forholdet mellom OH-innhold og viskositet til kvartsglass. Viktigheten av dette prosjektet underbygges av det faktum at disse egenskapene er kritiske for ytelsen til digelen under CZ-prosessen, samtidig som eksisterende studier mangler data fra direkte målinger av disse egenskapene. Det antas at enten høyere tørkingstemperatur eller lengre tørkingsperiode vil føre til lavere OH-innhold og høyere viskositet av kvartsglass.

En prosess ble etablert for å produsere prøver av silikaglass. Prosessen bestod av både varmebehandling og smelting av kvartssand med høy kvalitet, basert på ulike kombinasjoner av varighet av temperatur under størkning. Måling av hydroksylinnhold i silikaglass ble gjort med FTIR spektrometer. Et eksperimentelt oppsett for å måle viskositet av kvartsglass ble utviklet. I tillegg ble bobler i glassene karakterisert med Micro X-Ray Computational Tomography ( $\mu$ -CT).

De fleste resultatene styrket hypotesen om at viskositet av kvartsglass øker med lavere hydroksyl-innhold. For tørkeperiode på 1 time ble en betydelig forskjell i OH-innhold mellom prøver ved ulike tørketemperatur observert. For tørkeperiode på 24 timer var forskjellene ikke signifikante. Resultatene bekrefter den antatte sammenhengen mellom OH-innhold og viskositet. De fremhever viktigheten av optimale tørkeparametre for kvartssand, for å forbedre de mekaniske egenskapene til silikaglass, og dermed den mekaniske ytelsen under CZ-prosessen.

# Contents

<b>1</b>	<b>Introduction</b>	<b>1</b>
1.1	Background . . . . .	1
1.2	Aim and scope of the work . . . . .	3
<b>2</b>	<b>Theory</b>	<b>4</b>
2.1	Si-O system (silica) . . . . .	4
2.2	Kinetics of phase transformation of silica . . . . .	6
2.2.1	Quartz → cristobalite transformation . . . . .	6
2.2.2	Glass formation . . . . .	9
2.2.3	Devitrification of fused silica . . . . .	10
2.3	Water species in silica . . . . .	13
2.3.1	Hydrolytic weakening of silica . . . . .	13
2.3.2	The behavior of water diffusion . . . . .	15
2.4	Fused silica for Czochralski process . . . . .	17
2.4.1	Manufacture and composition of commercial fused silica crucibles . . . . .	17
2.4.2	Effects of devitrification . . . . .	19
2.4.3	Bubbles . . . . .	20
2.5	Characterization . . . . .	22
2.5.1	Measuring hydroxyl content in fused silica . . . . .	22
2.5.2	Viscosity measurement . . . . .	24
2.5.3	Bubble density characterization . . . . .	26
<b>3</b>	<b>Experimental</b>	<b>27</b>
3.1	Materials and apparatus . . . . .	27
3.2	Procedure . . . . .	28
3.2.1	Fused silica production . . . . .	28
3.2.2	drying of quartz sand . . . . .	30

3.2.3	Fused silica sample cutting . . . . .	31
3.2.4	OH-content measurement . . . . .	32
3.2.5	Viscosity measurement . . . . .	34
3.2.6	Bubble characterization . . . . .	37
3.2.7	X-ray diffraction . . . . .	37
<b>4</b>	<b>Results</b>	<b>39</b>
4.1	Validating experiments . . . . .	39
4.1.1	Production of fused silica . . . . .	39
4.1.2	Viscosity measurement . . . . .	41
4.2	Heat treatment . . . . .	42
4.3	Fused silica production . . . . .	44
4.4	OH-content . . . . .	45
4.5	Viscosity . . . . .	48
4.6	Bubble characterization . . . . .	54
4.6.1	Bubble volume . . . . .	54
4.6.2	Bubble distribution along Z-axis . . . . .	55
4.6.3	Number of bubbles . . . . .	56
4.6.4	Local examination . . . . .	57
<b>5</b>	<b>Discussion</b>	<b>59</b>
5.1	Validating experiments . . . . .	59
5.1.1	Development of experimental setup . . . . .	59
5.1.2	Development of melting procedure for fused silica . . . . .	60
5.2	OH-content in fused silica . . . . .	60
5.2.1	Trend in OH-contents along Z-axis of fused silica . . . . .	61
5.2.2	OH-contents in commercial fused silica crucibles . . . . .	62
5.3	Viscosity of fused silica . . . . .	63
5.3.1	Activation energy of viscous flow . . . . .	63

5.3.2	Comparison between commercial and lab-produced samples . . . . .	64
5.4	Relationship between OH-content and viscosity of fused silica . . . . .	65
5.4.1	Effect of cristobalite formation . . . . .	65
5.5	Possible effects of entrapped bubbles on viscosity . . . . .	66
5.6	Bubbles of fused silica samples and commercial fused silica crucible . . . . .	67
<b>6</b>	<b>Conclusion</b>	<b>69</b>
<b>7</b>	<b>Further work</b>	<b>70</b>
	<b>References</b>	<b>75</b>
<b>A</b>	<b>Appendices</b>	<b>i</b>
A.1	Matlab script for OH content calculation . . . . .	i
A.2	FTIR Spectra . . . . .	i
A.3	The measured loadings for each viscosity measurement . . . . .	viii
A.4	3D images of bubbles in a volume of 1.8 x 1.8 x 1.8 mm <sup>3</sup> at a corner on XY plane . . . . .	ix
A.5	Viscosities and OH contents in commercial fused silica crucibles provided by TQC . . . . .	x



## Figure

1.1	Schematic overview of the CZ growth process [2] . . . . .	1
2.1	Difference $\Delta G$ [cal/mol] in the thermodynamic potential between various forms of silica, using high cristobalite as reference, with different transition temperatures marked with arrows [10] . . . . .	5
2.2	Linear thermal expansion of quartz, tridymite, cristobalite, and silica glass [13] . . . . .	6
2.3	Transformation of Madagascar quartz at 1500°C, reprinted from [15] . . . . .	8
2.4	Schematic of specific volume against temperature . . . . .	9
2.5	A fused silica sample, fired at 1400°C for one hour, with a large white spot at the centre part, which a drop of tap water was placed on the surface before the heating . . . . .	11
2.6	$\equiv\text{Si-OH}$ group hydrogen-bonded with $\equiv\text{Si-O-Si}\equiv$ linkage [31] . . . . .	13
2.7	Left: Effects of hydroxyl ion content on viscosity of soda-lime-silica glass. Hydroxyl ion content of A: 110 ppm, B: 356 ppm, C: 763 ppm. Right: activation energy of viscous flow against hydroxyl content [33] . . . . .	14
2.8	IR transmission spectra of fused silica after being heat treated for 2 hours [35] . . . . .	15
2.9	Absorbance spectra of different quartz sand samples with the wavenumber from 3800 to 3700 $\text{cm}^{-1}$ . The peaks are corresponding to the "free" OH. Actual sample name was hidden due to commercial reason [38] . . . . .	17
2.10	Left: A patented quartz crucible manufacturing for CZ-silicon production [39]. Right: A finished fused silica crucible for CZ process [40] . . . . .	18
2.11	Viscosity of a type of commercial fused quartz in a temperature range of 1000° to 2000°C. Data provided by Momentive <sup>TM</sup> . . . . .	19
2.12	Bubble size distribution of, Left: sample A, Right: sample B [44] . . . . .	22
2.13	Geometry and coordinate system of (a) flat-ended, (b) spherical and (c) conical indentations [47] . . . . .	24
3.1	Crucible for fused silica production . . . . .	28

3.2	Heating profile for melting of quartz sand. Variables $T$ and $t$ represent the drying temperature and holding time shown in Table 3.3 . . . . .	29
3.3	Furnace compartment . . . . .	30
3.4	Schematic of coarse sample cutting; Left: side view of the sample, Right: top view of the sample. *Thickness of the coarse cutting blade was ca. 3 mm . . . . .	31
3.5	Schematic of fine sample cutting; Left: after removal of top and bottom layers and the sides, Right: after further separated into 4 samples for different experiments, with the remarks of the purposes for each sample. Thickness of the fine cutting blade was ca. 0.5 mm . . . . .	31
3.6	Cutting of fused silica sample. Left: coarse cutting, Right: fine cutting . . . . .	32
3.7	The main components in the FTIR compartment during the measurement of OH-contents in fused silica samples . . . . .	33
3.8	Examination positions on a fused silica sample . . . . .	34
3.9	Viscosity measurement setup, Left: External components, Right: Internal components. Elements contributing to total loading weight are marked by letter a to e . . . . .	35
3.10	Heating profile for viscosity measurement . . . . .	36
4.1	A silica glass sample after a trial melting test with 1 hour holding period at 1800°C. Left: a sample in a cracked alumina crucible. Right: a part of the sample consisting of molybdenum lining, cristobalite, and glass . . . . .	39
4.2	XRD pattern of the melting crucible wall after the melting of quartz, with the mullite reference in red . . . . .	40
4.3	XRD patterns of the top surfaces of 3 trial silica glasses (The quartz sand was heat treated at 600°C for 1 hour) in normalized intensity . . . . .	40
4.4	Creep of a trial fused silica sample (dried at 600°C for 1 hour) at each temperature step over time . . . . .	41
4.5	A trial fused silica sample with a thick, complete layer of cristobalite after a validating viscosity measurement. Left: indented surface. Right: cross-section . . . . .	42
4.6	XRD patterns of two dried quartz sands (100-24 and 1100-24) in normalized intensity, with pure quartz reference in red . . . . .	43

4.7	The appearance of sample 600-01 before cutting . . . . .	44
4.8	XRD spectra of the surfaces of all FTIR sample #1 except 100-24 . . . . .	45
4.9	The transmittance at different measured positions (shown in Figure 3.8) of sample 900-01(1)	45
4.10	OH-contents in all FTIR samples #1 (shown in Figure 3.5). The viscosity measurement was performed at the same Z-position . . . . .	47
4.11	OH-contents in different vertical positions of all fused silica samples . . . . .	47
4.12	The displacement behavior of 900-01(1) at each temperature step over time in hour, with a zoom-in illustration of the relaxation period at the beginning of 1400°C . . . . .	48
4.13	The creep rates of 900-01(1) at all temperature steps . . . . .	49
4.14	The indented surface of 600-01(2) after viscosity measurement in normalized intensity, with cristobalite reference in red . . . . .	51
4.15	Effects of different drying temperatures (for 1 hour) on viscosity, with the activation energies $E_a$ of viscosity for 600-01(2) . . . . .	52
4.16	Effects of different drying temperatures (for 24 hour) on viscosity . . . . .	53
4.17	Effects of drying time (at 900°C) on viscosity . . . . .	53
4.18	Effects of drying time (at 1100°C) on viscosity . . . . .	54
4.19	Bubble volume and bubble amount distribution from the top to bottom surface, along Z-axis	55
4.20	Bubble diameter distribution of the three examined fused silica samples . . . . .	56
4.21	Cumulative bubble diameter distribution of the three examined fused silica samples . . . . .	57
4.22	3D view of the entrapped bubbles in a volume of $1.8 \times 1.8 \times 1.8 \text{ mm}^3$ at the centre of X-Y plane	58
A.1	The transmittance at different measured positions (shown in Figure 3.8) of sample 600-01(1)	i
A.2	The transmittance at different measured positions (shown in Figure 3.8) of sample 600-01(2)	ii
A.3	The transmittance at different measured positions (shown in Figure 3.8) of sample 600-01(3)	ii
A.4	The transmittance at different measured positions (shown in Figure 3.8) of sample 900-01(2)	iii
A.5	The transmittance at different measured positions (shown in Figure 3.8) of sample 900-01(3)	iii
A.6	The transmittance at different measured positions (shown in Figure 3.8) of sample 900-24(1)	iv
A.7	The transmittance at different measured positions (shown in Figure 3.8) of sample 900-24(2)	iv
A.8	The transmittance at different measured positions (shown in Figure 3.8) of sample 900-24(3)	v

A.9	The transmittance at different measured positions (shown in Figure 3.8) of sample 1100-01(1)	v
A.10	The transmittance at different measured positions (shown in Figure 3.8) of sample 1100-01(2)	vi
A.11	The transmittance at different measured positions (shown in Figure 3.8) of sample 1100-01(3)	vi
A.12	The transmittance at different measured positions (shown in Figure 3.8) of sample 1100-24(1)	vii
A.13	The transmittance at different measured positions (shown in Figure 3.8) of sample 1100-24(2)	vii
A.14	The transmittance at different measured positions (shown in Figure 3.8) of sample 1100-24(3)	viii
A.15	3D view of the entrapped bubbles in a volume of $1.8 \times 1.8 \times 1.8 \text{ mm}^3$	ix
A.16	The viscosities of commercial fused silica crucibles that were heat treated at different temperatures, provided by TQC. HT1 and HT4 represent the lowest and highest temperature respectively [25]	x
A.17	The OH contents in some commercial fused silica crucibles that were heat treated at different temperatures, provided by TQC. BC and BF represent the OH contents in bubble-composite and bubble-free layer respectively. HT1 and HT4 represent the lowest and highest temperature respectively [25]	xi

## Table

2.1	Polymorphs of SiO <sub>2</sub> [5] . . . . .	4
2.2	Observations of devitrification of clear silica glass under different atmospheres. For all the conditions, the samples were heated at 1300°C for 72 hours [24] . . . . .	11
2.3	Contamination levels in the types of silica used by Yamahara <i>et al.</i> (wt ppb) [28] . . . . .	13
2.4	Concentrations of impurities of quartz powder QPSR and QPKY (ppm) . . . . .	20
2.5	Process parameters used for silica glass production and the bubble concentration in the silica glass samples produced from two different quartz sands with different treatment [43] .	21
2.6	The effects of fusion temperature and ratio (GLP/O <sub>2</sub> ) R <sub>z</sub> on bubble concentration (#/mm <sup>3</sup> ) in the silica glass produced from leached QPSR . . . . .	21
3.1	Concentration of impurities in quartz sand A (wt ppm) [51] . . . . .	27
3.2	Equipment details of all experiments . . . . .	28
3.3	Drying profile prior to melting, with heating rate of 200°C per hour in ambient air . . . . .	30
3.4	Polishing steps . . . . .	33
3.5	XRD configuration parameter for measuring both heat treated quartz sands and fused silica	38
4.1	Weight loss of quartz sands after drying . . . . .	43
4.2	The OH-contents in all fused silica samples (Three parallels for each sample) . . . . .	46
4.3	Viscosities (on log scale) of all fused silica samples at each temperature step (two parallels for each sample) . . . . .	49
4.4	Creep rates at different temperature steps and the indented depth from the beginning of 1400°C step to the end of 1550°C . . . . .	50
4.5	Activation energies of viscosity for all the samples in different temperature ranges (kJ/mol) .	51
4.6	Total bubble volume and calculated porosity of samples that were heat treated for 1 hour . .	55
4.7	Bubble concentration in the analyzed volume . . . . .	56
4.8	Properties of bubbles in a smaller analyzed volume (1.8 x 1.8 x 1.8 mm <sup>3</sup> ) at different positions on XY plane . . . . .	58
A.1	Loadings for each viscosity measurement . . . . .	viii

A.2 Summary of the OH contents in commercial crucibles provided by TQC. BC and BF represent the OH contents in bubble-composite and bubble-free layer respectively. HT1 and HT4 represent the lowest and highest temperature respectively [25] . . . . . xi

## 1 Introduction

### 1.1 Background

The demand for clean, renewable, and carbon free energy sources is increasing nowadays. The availability and environmental friendliness of solar power have caused it to be one of the most popular options under the renewable energy category, and its development has been accelerating since the 1990's. Silicon-based solar cells have been dominating the solar cell market for decades. However, the solar cell production industry still faces a lot of challenges. Due to the requirement of extremely pure materials for the photovoltaic cell [1], the fused silica crucible, which is commonly used for monocrystalline silicon production by a process called Czochralski (CZ) process, plays a very important role in ensuring a high quality silicon ingot. In the production of monocrystalline solar cells, the latest process developments have yielded higher amounts of crystals from each crucible, thus requiring larger sized crucibles. Therefore, the crucibles should also be of higher quality and greater stability in order to minimize the negative effects on the silicon.

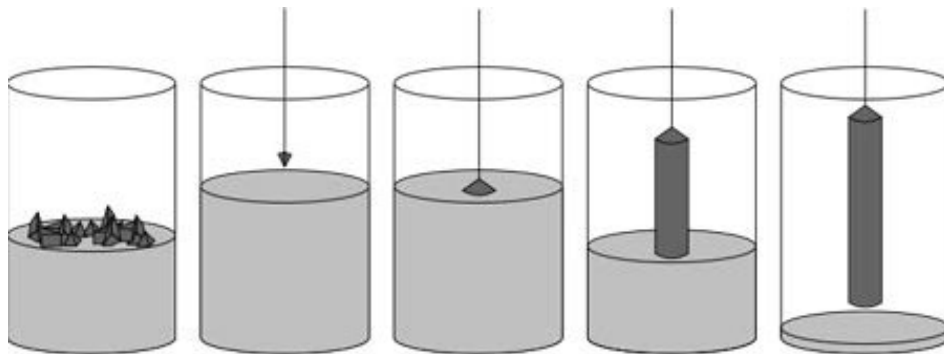


**Figure 1.1** Schematic overview of the CZ growth process [2]

Figure 1.1 shows the schematic of the general CZ process. First, high purity silicon is melted in a fused silica crucible which is placed on a graphite support, at a temperature which is higher than silicon's melting point ( $1414^{\circ}\text{C}$ ), normally ca.  $1500^{\circ}\text{C}$ . The melting process is performed with an inert atmosphere (typically argon) in a chamber, which is typically made of steel with graphite insulation in order to facilitate the removal of  $\text{SiO}$ . When the desired doping species is added, depending on the type of the final ingot and

the melt is stable, a rod mounted monocrystalline seed with typical crystal orientation of (100) or (111) is dipped into the molten silicon. It is then slowly pulled upwards with a reverse rotation to that of the crucible. This way, a monocrystalline ingot is grown with the same crystallographic orientation as the seed crystal.

At such a high temperature, there are a lot of uncontrollable and unexpected events. Examples of interactions between the crucible and the silicon ingot include the migration of entrapped gas bubbles from the crucible and the flaking of the formed cristobalite. They can cause potential structural loss of the silicon ingot and the contamination of the ingot, and they have been studied by the industry for decades. Besides, typically 1 - 2 mm of the inner wall will be dissolved into silicon melt during the process. Most of these problems can be related to the viscosity of the crucible. The viscosity of a material decreases with the increase of temperature. Consequently, the fused silica crucible softens at elevated temperatures. It will eventually sag during CZ process, as it can no longer mechanically support the upper part of the crucible. The softening of the crucible initiates the migration of entrapped gas and foreign particles from the crucible towards the silicon ingot. To some extent, the viscosity of fused silica crucible is dependent on the water content (mainly in the form of hydroxyl) of the crucible. The incorporation of water into fused silica lowers its viscosity [3]. This negative impact can be related to the drying process and the melting of the quartz sand, which can greatly influence the resulting water content of the fused silica crucible. A better understanding of these properties of fused silica appears to be important in order to solve these observed problems, and the knowledge can eventually contribute to improve the quality of the solar cells and enhance the efficiency of electric power generation.

It is noticed that the relationship between viscosity and water (Hydroxyl) content in fused silica has not been deeply investigated. The existing studies are also lacking the data of direct measurements of these characteristics that support this relationship, explicitly for fused silica. Considering the importance of these two properties for the crucible performance during CZ process, a quantitative study will be useful for improving the quality of the crucibles.



## 1.2 Aim and scope of the work

The aim of this work was to investigate the effect of different drying parameters (temperature and period) for quartz sands on the viscosity and hydroxyl (OH) content of fused silica. A set of data from the direct measurement of these properties of fused silica was created in order to highlight the relationship between viscosity and hydroxyl (OH) content of fused silica, which will be highly beneficial to the industry.

As an extension of the previous project with commercial fused silica crucible samples, this work involves the fused silica samples produced at NTNU, that are made of high purity quartz sand provided by The Quartz Corp. The fused silica samples were prepared by melting the high purity quartz sands with different drying temperatures and periods, by the use of laboratory-scale equipment. Validating melting tests and viscosity measurements were done before the main tests started, due to the use of novel experimental setup and new process. Their results were considered to improve and finalize the experimental of this project. A setup involving a high temperature furnace, a displacement sensor, and so on, which was built by O. Paulsen (SINTEF Industri), was used for viscosity measurement. OH-content measurement was performed with Infrared spectroscopy. Entrapped gas bubble characterization was also performed by Micro X-Ray computation tomography with the assistance from S. Rørvik (SINTEF Industri). Studies on the kinetics of phase transformations, as well as the theories behind the viscosity measurement and Infrared spectroscopy were also carried out. Literature studies will be presented first in this report. It will be followed by the explanations of experimental procedures, results, and discussions.

## 2 Theory

### 2.1 Si-O system (silica)

In the Si-O system, silica or silicon dioxide ( $\text{SiO}_2$ ) is the only thermodynamically stable compound. Under atmospheric pressure, there are three stable crystalline forms of this compound: quartz, tridymite, and cristobalite [4]. All the silica phases under atmospheric or low pressure are summarized in Table 2.1.

**Table 2.1** Polymorphs of  $\text{SiO}_2$  [5]

<b>Quartz - tridymite - cristobalite group</b>	<b>Form</b>	<b>Crystal symmetry</b>
Atmospheric and low pressure	$\alpha$ -quartz	Trigonal
	$\beta$ -quartz	Hexagonal
	* $\alpha$ -tridymite	Orthorhombic
	* $\beta$ -tridymite	Hexagonal
	$\alpha$ -cristobalite	Tetragonal
	$\beta$ -cristobalite	Cubic
	Melanophlogite	Cubic
	Moganite	Monoclinic
	Vitreous silica	-

\*Not stable in pure Si-O system

The  $\text{SiO}_4$  tetrahedron is the basic building block in all silica crystalline structures. A  $\text{SiO}_4$  tetrahedron is a silicon atom with four oxygen atoms at all four corners. The Si-O bonds have predominantly covalent character. The phase transitions of silica can be distinguished by displacive and reconstructive. Displacive transformations like  $\alpha$ - to  $\beta$ -variant of quartz and cristobalite involve only alterations of angles and bond lengths without any breakage of chemical bonds for stabilizing the crystal structure. Therefore, displacive transformation can take place instantaneously upon heating or cooling. Reconstructive transformation, such as quartz to cristobalite, requires the chemical bonds to be broken. The process of complete transformation requires a relatively long period. Rapid temperature change often results in incomplete rebuilding of chemical structures [6].

The relevant phases to be considered in this project include quartz, tridymite, cristobalite, and silica

---

glass. The thermodynamic stabilities of these phases, with respect to temperature, is shown in Figure 2.1. Cristobalite appears to be the stable phase above 1027°C, as the formation of tridymite requires the presence of particular impurities [7]. If pure quartz is heated directly, it passes the tridymite phase and starts transforming to  $\beta$ -cristobalite directly at a lower temperature, instead of transforming at the theoretical temperature which is 1470°C. Cristobalite can also form below 1000°C from silica glass [8]. The cristobalite formation temperature is strongly influenced by the atmosphere and impurity contents in silica. The effects of these factors and the kinetics of this transition will be discussed more deeply in Section 2.2. However,  $\beta$ -cristobalite formed below the theoretical temperature is a metastable phase. It will slowly alter to another polymorph which is more stable at that temperature range [9]. Considering the tridymite phase, cristobalite will still be the thermodynamically stable phase at above 1470°C, as shown in Figure 2.1.  $\beta$ -cristobalite phase will undergo high to low transition by displacive transformation upon cooling (below ca. 250°C). It will exist as  $\alpha$ -cristobalite at room temperature.

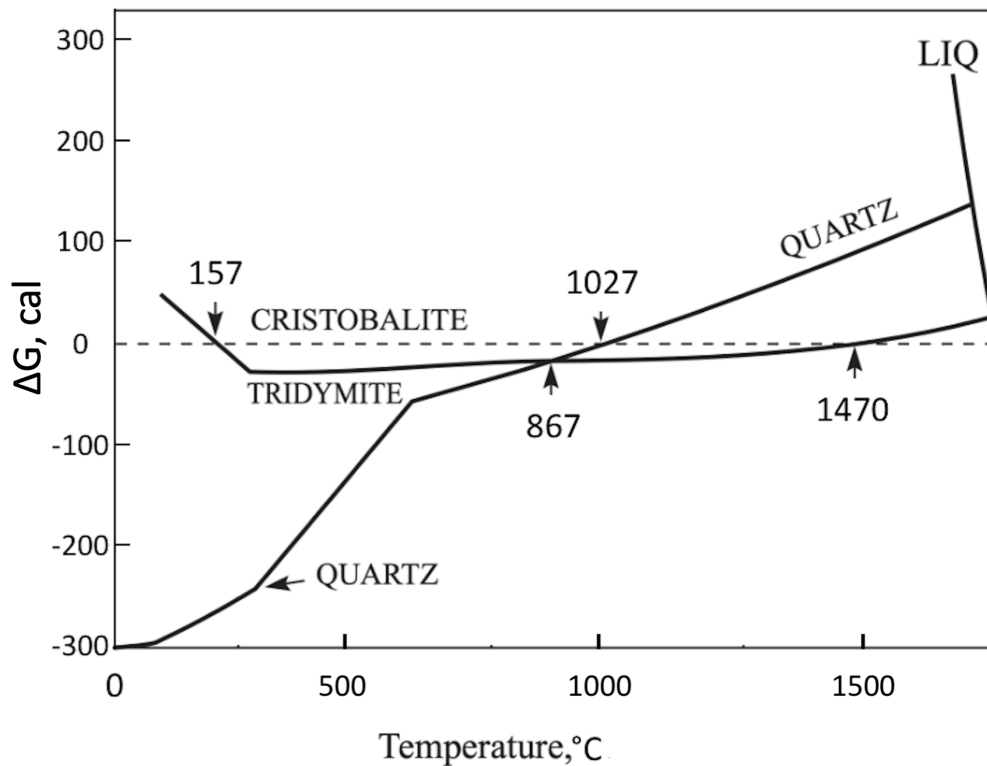


**Figure 2.1** Difference  $\Delta G$  [cal/mol] in the thermodynamic potential between various forms of silica, using high cristobalite as reference, with different transition temperatures marked with arrows [10]

Figure 2.2 shows the significant volume expansion associated with displacive transformations as well as the differences in such expansion among different polymorphs.  $\alpha$ - and  $\beta$ -cristobalite have average bulk thermal expansion values of  $91.7 \times 10^{-6} \text{ }^\circ\text{C}^{-1}$  ( $28^\circ\text{C} - 218^\circ\text{C}$ ) and  $6 \times 10^{-6} \text{ }^\circ\text{C}^{-1}$  ( $400^\circ\text{C} - 1200^\circ\text{C}$ ) [11][12]. The material with such notably different values of thermal expansion coefficient will likely experience mechanical failures such as cracking upon cooling when it undergoes the transition of high to low cristobalite. The difference of the expansions of the relevant polymorphs, quartz and cristobalite, is severe at the temperature range of  $208^\circ\text{C}$  to  $573^\circ\text{C}$ . Silica glass has a significantly lower thermal expansion coefficient of  $0.5 \times 10^{-6} \text{ }^\circ\text{C}^{-1}$  in the temperature range of  $20^\circ\text{C} - 900^\circ\text{C}$ .

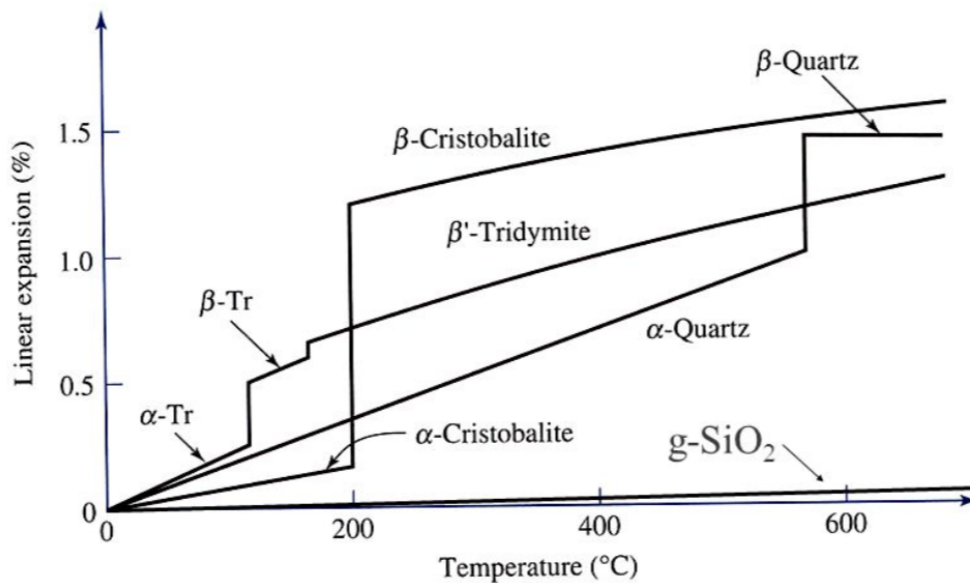


**Figure 2.2** Linear thermal expansion of quartz, tridymite, cristobalite, and silica glass [13]

## 2.2 Kinetics of phase transformation of silica

### 2.2.1 Quartz $\rightarrow$ cristobalite transformation

At room temperature,  $\text{SiO}_2$  exists as  $\alpha$ -quartz under atmospheric pressure. It undergoes  $\alpha$ - to  $\beta$ -transition at  $573^\circ\text{C}$ . At  $870^\circ\text{C}$ ,  $\beta$ -quartz transforms to  $\beta$ -tridymite, and then to  $\beta$ -cristobalite at  $1470^\circ\text{C}$ . Theoretically,  $\beta$ -cristobalite is a phase that is thermodynamically stable over  $1470^\circ\text{C}$  until it melts at  $1705^\circ\text{C}$ .

Quartz  $\rightarrow$  cristobalite is an important transformation to be considered when pure quartz is heated, as the

tridymite phase is normally neglected, as discussed in Section 2.1. Mariani and Hobbs [14] suggested that this transformation must involve about one third of the bonds to be broken and reformed. The consequence of this event is that the quartz phase is driven further from the crystalline state. The contribution on bond breaking from the presence of water should also be acknowledged, and it will be discussed in Section 2.3. Chaklader and Roberts [15] also established that this transformation is indirect, and an intermediate transition phase is involved, which is described in Equation 2.1. The transition phase was found to be non-crystalline by XRD and DTA.



Chaklader and Roberts [15] performed heating at different temperatures (1500°, 1550°, 1600°, and 1650°C) with different types of quartz. The amount of transition phase was calculated by subtracting the percentage amount of total crystalline phase (quartz and cristobalite) from 100. From their results, the total amount of quartz and cristobalite was less than 100%, indicating that there was another present phase other than these crystalline phases. Figure 2.3 illustrates the conversion process with a transition phase during the transformation of Madagascar quartz. The quartz slowly transformed to the transition phase at the beginning, followed by a more rapid conversion that represented the propagation of the nucleated zones. The much slower formation of cristobalite can also be observed in Figure 2.3. Even all the quartz phase was consumed after 8 hours, the amount of cristobalite was only ca. 78%. This transition behaviour was also reported in the investigation by Kjelstadli [16]. Various types of quartz were heated up to 1600°C for different periods of time (15 - 60 mins), which were very short compared to other studies, which their tests typically lasted for over 10 hours. The resulting materials consisted of higher amount of the amorphous transition phase than that of the cristobalite phase. By considering that such a short heating was probably just the beginning period of a complete cristobalite transformation, the formation of cristobalite is predicted to be extremely slow until there is enough amount of transition phase, or more accurately, high enough availability of critical-sized nuclei of cristobalite in the transition phase.

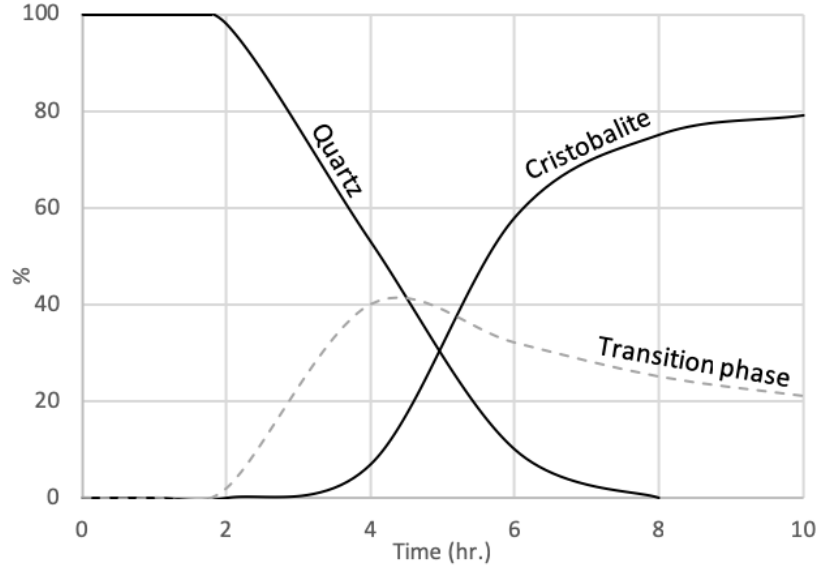


**Figure 2.3** Transformation of Madagascar quartz at 1500°C, reprinted from [15]

Mitra [17] carried out a similar study on the phase transformation of two types of high-purity quartz. A model was developed to describe the rate of the formation of the transition phase and cristobalite phase. The conversion of quartz to the transition phase was found to follow the rate described by Equation 2.2:

$$A_f = \left(1 - \frac{ut}{r_0}\right)^3 \quad (2.2)$$

where  $A_f$  is a fraction of the remaining unconverted quartz after time  $t$ ,  $u$  is the radial velocity of decomposition (i.e. the linear rate of propagation of quartz to transition phase boundary), and  $r_0$  is the initial average radius of the present particles.

Mitra [17] assumed that the formation rate of cristobalite is proportional to the relative amount of present transition phase, and the formation takes place throughout the body instead of the surface only. The difference of the densities of quartz and transition phase ( $2.65\text{g/cm}^2$  and  $2.30\text{g/cm}^2$  respectively) induces stress and cracks in the material's body, as the transition phase occupies a greater volume. Moreover, this reconstructive transformation (quartz  $\rightarrow$  transition phase) which involves the breakage of chemical bonds would cause severe fragmentation in the transition phase. It was observed that the partially converted quartz particles, which the cristobalite is absent, could easily be crushed into powder by applying pressure

by hands. This implies that there would be high amount of well-distributed internal nucleation centres. These are the reasons of the formation of cristobalite internally [18].

### 2.2.2 Glass formation

Fused silica, or quartz glass, is often needed for specific applications, even both quartz and fused silica are considered as extremely pure materials [19]. Production of fused silica requires a minimum temperature of  $1710^{\circ}\text{C}$ , which is the melting point of silica. In general, glass is formed by cooling a liquid of a raw material without any re-crystallization. This process is illustrated by a qualitative specific volume - temperature plot which can be seen in Figure 2.4. Upon cooling, nucleation and crystallization are possible events. In this case, there will be an abrupt change in specific volume at the melting point, and the cooled material will become crystal. If no crystallization takes place during cooling, volume will decrease at a linear rate until it reaches the glass transformation range, where there is a decrease in the coefficient of expansion. By further cooling the material, glass will form [20]. Glass transition temperature (denoted by  $T_g$  in Figure 2.4) is the intersection point between the curves of the glassy state and the supercooled liquid (or rubbery state). When the temperature of the material drops to the glass transition range, the viscosity of the material drastically increases, resulting in a glass with extreme high viscosity, which exhibits solid-like mechanical properties.

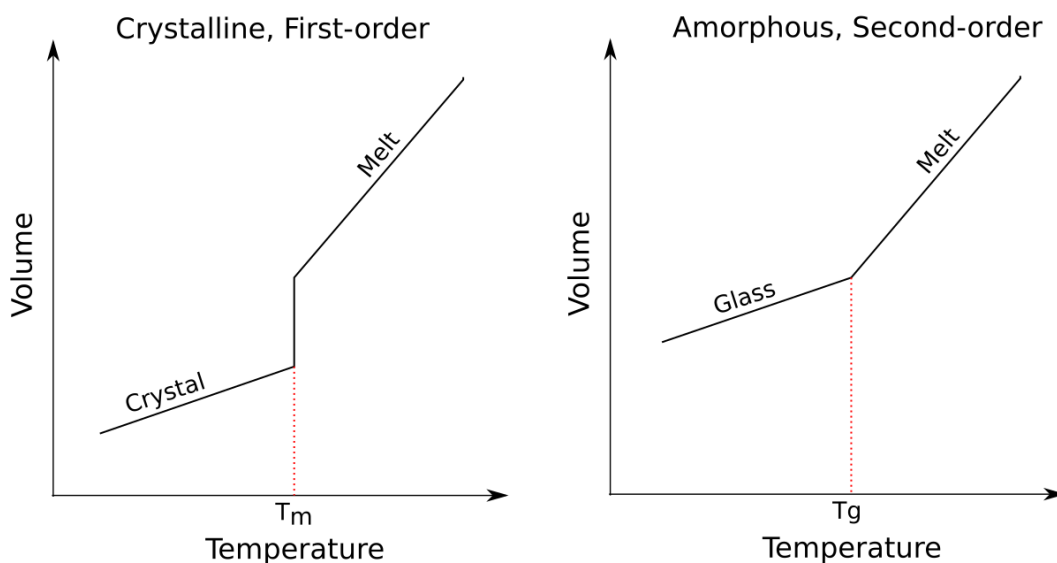


**Figure 2.4** Schematic of specific volume against temperature

The cooling rate strongly influences the glass formation. Normally, if the glass forming liquid is cooled with a high enough rate, the crystallization at around the melting point is avoided and, thus, the final state of the material will be glass. It is because the relaxation time of the system at the glass transition range exceeds the period of the experiment, so the crystallization is avoided. If a sufficiently slow cooling rate is adopted, crystallization may take place regionally [21]. However, silica is known as a good glass former. Silica glass can still form even the cooling rate is extremely low [22].

### 2.2.3 Devitrification of fused silica

For any substance, its crystalline is always more stable than glass state. Devitrification of fused silica is one of the limiting factors in high-temperature applications, and of great interest in this work due to its effects on the fused silica at high temperatures. Due to hysteresis, reheating the glass would lead to a different property changing behaviour compared to cooling, as discussed in Section 2.2.2. The main difference between reheating the glass and cooling is that the glass transition temperature is higher. It normally takes place at temperatures over 1150°C. It is also possible for the process to take place below 1000°C with the presence of impurities. The general devitrification mechanism begins at present random nuclei, and they permeates through the whole fused silica eventually. The product of devitrification of fused silica is  $\beta$ -cristobalite, which is structurally more stable. The formed  $\beta$ -cristobalite undergoes a transition towards a metastable phase, followed by a high to low transition at ca. 227°C [23].

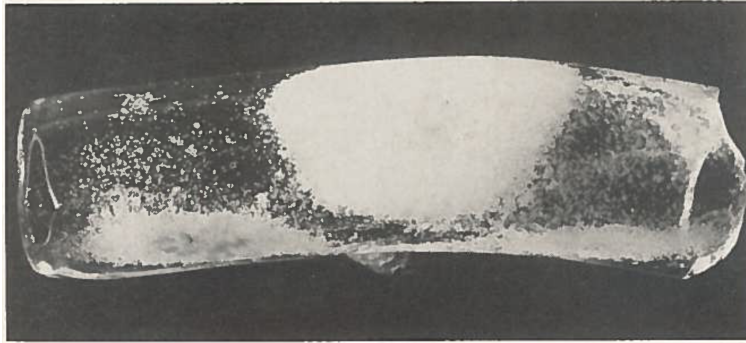
Most of the studies used the thickness of cristobalite layer on the surface or physical appearance as an index to quantify the effect of devitrification. One commercial report from Tosoh [24] pointed that devitrification occurred only under specific conditions for their silica glass products made of high purity quartz sand. The occurrence of devitrification was highly dependent to the atmosphere and presence of impurities. Table 2.2 summarizes the observations of the effects of devitrification under different conditions. The effect of devitrification was observed with the presence of oxygen whereas devitrification did not take place when the samples were heated under atmospheres where oxygen and water were absent. From the previous works of this project [25], the nucleation of cristobalite was observed to take place mainly at the surface, and rarely in the interior.



**Table 2.2** Observations of devitrification of clear silica glass under different atmospheres. For all the conditions, the samples were heated at 1300°C for 72 hours [24]

Gas composition	Observations	Devitrification thickness ( $\mu\text{m}$ )
Air	Complete devitrified surface	250
Dried O <sub>2</sub>	50% devitrified surface	100 ~150
Industrial N <sub>2</sub>	Devitrified surface	-
N <sub>2</sub> (O <sub>2</sub> and H <sub>2</sub> O removed)	Not devitrified surface	-
H <sub>2</sub> (O <sub>2</sub> and H <sub>2</sub> O removed)	Not devitrified surface	-

Ainslie *et al.* [26] investigated the factors that influence the devitrification kinetics of fused silica. General Electric fused silica with a commercial designation 204A was used for most of the quantitative measurements. In addition to heating the fused silica with different gas composition which is similar with Tosoh's works [24], the effect of different sample treatments was also investigated. A drop of tap water was added on the surface of a flame polished specimen before it was fired at 1400°C for one hour. A severe nucleation of cristobalite in the middle part of the sample can clearly be seen in Figure 2.5. The nucleation was catalyzed by the mineral residue after water evaporated. The experiment was repeated by using distilled water instead of tap water. The resulting sample showed much less nucleation than that with tap water.

**Figure 2.5** A fused silica sample, fired at 1400°C for one hour, with a large white spot at the centre part, which a drop of tap water was placed on the surface before the heating

The impurity contents also manipulate the devitrification rate of fused silica. In the solar cell industry, a coating of alkaline-earth element solution at inner surface of the fused silica crucible is often used to promote devitrification (formation of cristobalite) of fused silica crucible. An incomplete layer of

cristobalite will develop and exist as islands with brownish rings that can possibly flake. This act can avoid flaking of the formed cristobalite and, as a result, contamination of the silicon ingot. A complete layer of cristobalite also acts as a wall to avoid the migration of entrapped gas bubbles in the crucible towards the silicon ingot. Hence, dislocation and contamination in the silicon ingot can be minimized. Huang [27] studied the effects of  $Ba^{2+}$  doping on the crucible surface on the cristobalite growth. It was concluded that a white, smooth cristobalite layer was obtained when the concentration of  $Ba^{2+}$  doping was higher than 100 ppm. With the doping, the Ba atoms are incorporated in the network of  $SiO_4$  tetrahedra, or only exist in the interstitial sites. In both cases, the nucleation process will still be enhanced by the presence of  $Ba^{2+}$ . In the former case, the growth rate will also be enhanced due to the fact that the bond energy between Ba and oxygen atoms is lower than that between Si and oxygen atoms, and consequently the energy barrier for devitrification becomes lower.

White spots with brown edges is a common appearance observed when devitrification of fused silica takes place on the surface of fused silica crucible during CZ process. Yamahara *et al.* [28] studied the density of the brownish spots caused by devitrification in relation to the raw material quality. Three different types of fused silica samples were prepared by electrical fusion of three different powders including natural quartz, synthetic silica, and Al-doped synthetic silica powder. The contamination levels in the silica powders (except Al-doped) were given and are summarized in Table 2.3. The contamination levels in the Al-doped were almost the same as those in the synthetic silica glass powder, except aluminium content which was 7.9 ppm. All the fused silica samples were exposed to silicon at 1500°C and 1600°C with argon atmosphere. It was observed that the density of brownish spots in Natural Quartz glass was significantly higher than that of the rest of the samples. The number of devitrification spots formed in the interior of the bulk of Natural Quartz glass was also noticeably larger than that of the rest of the samples. Silicate glass incorporated with alkaline earth elements exhibited a higher tendency of crystallization. It implies that such kind of impurities should be kept at a minimum level to avoid devitrification. It was also suggested that aggregates with high concentration of impurities, which can be the nucleation sites for devitrification, is one of the main reasons for the formation of brownish spots. More evenly distributed impurities in higher concentrations can be tolerated, compared to locally accumulated impurities.

**Table 2.3** Contamination levels in the types of silica used by Yamahara *et al.* (wt ppb) [28]

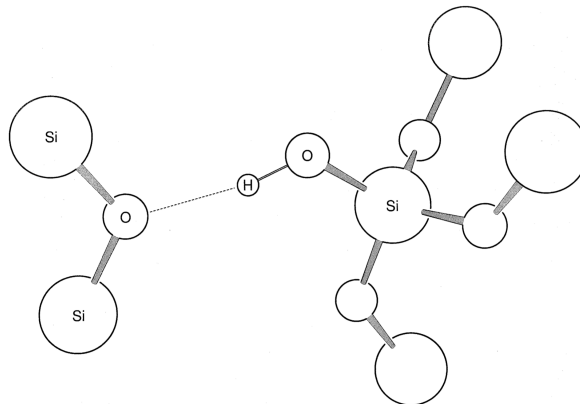
Silica type	Na	K	Ca	Al	Fe	Cu	Mn	Ti	P	As	B	Ge	U	Th
Natural quartz	225	94	560	6800	180	1.3	4.8	1500	130	2.1	70	630	1.4	4.0
Synthetic silica	10	2	5	1	20	<0.5	<0.5	<1	5	0.03	3	8.8	<0.06	<0.3

## 2.3 Water species in silica

Water present in glass is often considered as impurity because it extensively affects the physical properties as well as the behaviour crystallization of the glass. It is possible for water to be incorporated in quartz. Water can exist in quartz through fluid inclusion, and be absorbed into the walls along the microfractures within the quartz bulk, which is called free water [29]. Besides, it can be incorporated into  $\text{SiO}_4$  network by forming chemical bonds with the host species and reacting to form OH bonds with silicon atoms.

### 2.3.1 Hydrolytic weakening of silica

Existing water can weaken the mechanical properties of quartz and cause mechanical defects [30]. Hydroxyl is introduced to silica glass which is produced by melting quartz sand in an environment where hydrogen is present. Hydroxyl ( $\text{OH}^-$ ) groups dominates among other water species when silica glass is hydrated over  $550^\circ$  [3]. OH-groups are incorporated in the quartz network, which is illustrated in Figure 2.6.

**Figure 2.6**  $\equiv\text{Si-OH}$  group hydrogen-bonded with  $\equiv\text{Si-O-Si}\equiv$  linkage [31]

The water in silica generally undergoes the reaction shown in Equation 2.3 [32]:



Some Si-O bonds are replaced by non-bridging  $\text{OH}^-$ . The silica network is weakened when water is incorporated into silicate structure, due to the reduced number of bridging oxygen atoms. It results in a higher atom mobility, and, thus, a lower viscosity, higher thermal expansion, and higher possibility of local crystallization.

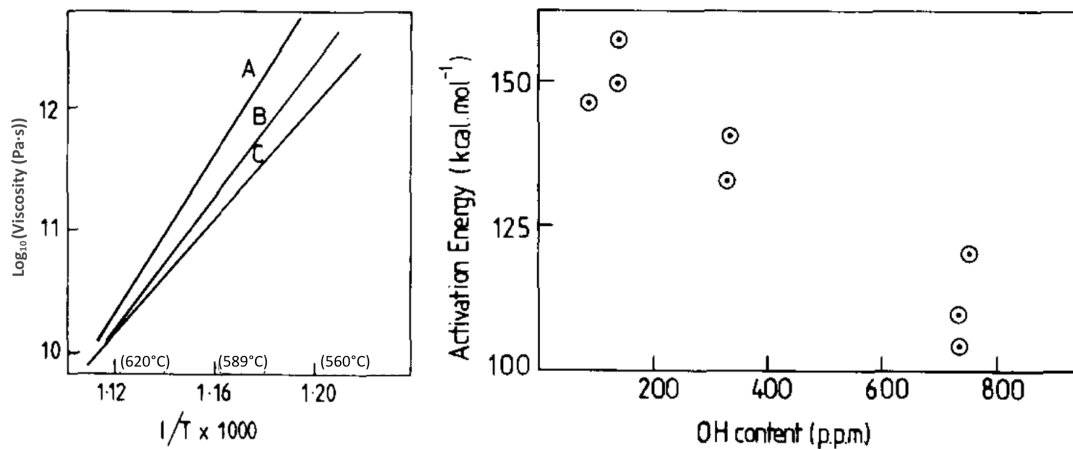


**Figure 2.7** Left: Effects of hydroxyl ion content on viscosity of soda-lime-silica glass. Hydroxyl ion content of A: 110 ppm, B: 356 ppm, C: 763 ppm. Right: activation energy of viscous flow against hydroxyl content [33]

There has been investigation on the effects of water content in glass on its physical properties such as viscosity, fracture strength, glass transition temperature, and so on [34]. Mcmillan [33] presented the results of the measurement of the viscosity of soda-lime-silica glass with different hydroxyl ion contents (110, 356, and 763 ppm). The viscosity of the glasses was measured in the temperature range of ca. 550°C to 620°, by fibre extension. The results showed that the viscosity of the glass (C) with the highest hydroxyl content was the lowest at all temperature steps. However, the difference of the viscosity between glasses decreased as the temperature increased, which also aligned with the results from the previous works of this project [25]. Figure 2.7 illustrates the relationship between the activation energy of viscous flow and OH-content. During CZ process, a fused silica crucible with a lower viscosity will result in a more severe

sagging at the pulling temperatures. Besides, the entrapped gas bubbles in the crucible could grow and migrate towards silicon melt more rapidly when the crucible softens at elevated temperature.

### 2.3.2 The behavior of water diffusion

Transport of water both from and into the glass are important events to be considered. Zhou [35] examined the effect of heat treatment of fused silica (with thickness of 1 mm) with the presence of hydrogen on the samples' OH-contents. Same type of fused silica was heat treated at different temperatures. The OH levels of different samples were then measured by an infrared spectrometer, and the time dependence of dehydroxylation was studied. The results of the investigation are shown in Figure 2.8.

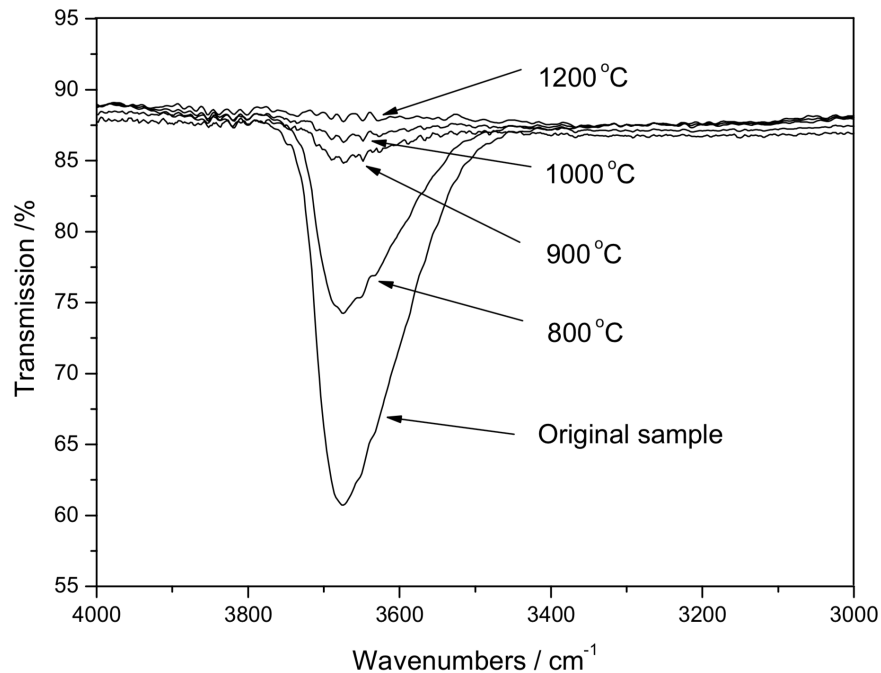
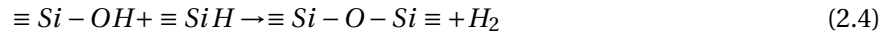


**Figure 2.8** IR transmission spectra of fused silica after being heat treated for 2 hours [35]

It is clear that the concentration of OH in silica glass reduced as the heat treatment temperature increased. It was also found that 90% of OH was removed after ca. 1 hr at 1000°C, while only 45% of OH was removed at 800°C for the same period. It can be deduced that a higher heat treatment temperature will probably give a steeper curve for OH-content removal. It was assumed that the OH was removed through the release of hydrogen from the glass, by considering the measured amount of water and hydrogen released during

the heat treatment. This reaction is shown in Equation 2.4.



This hydroxyl removal process involves the breakage of SiO-H bond and the diffusion of the molecular hydrogen. The observed difference of the activation energies for the dehydroxylation process at different temperature ranges ( $254 \text{ kJmol}^{-1}$  at  $700^\circ - 900^\circ\text{C}$ ,  $32 \text{ kJmol}^{-1}$  at  $900^\circ - 1100^\circ\text{C}$ ) gives the information about which reaction is dominating the process of dehydroxylation. Referring to the binding energy of SiO-H and the activation energy for the diffusion of molecular hydrogen in silica glass, the dominating process of dehydroxylation in the range of  $700^\circ - 900^\circ\text{C}$  is the breakage of SiO-H bond, while that in the range of  $900^\circ - 1100^\circ\text{C}$  is the diffusion of molecular hydrogen.

A thin water layer can form on quartz surface in an atmosphere where water vapor is present. Water molecules in the atmosphere attach to the functional groups present at the surface of quartz through hydrogen bonding. Water adsorption at the surface of synthetic or purified quartz sand was expected to be less severe as a great amount of functional groups was removed [36]. Silanol (Si-OH) group is one of the species that can be found at the surface of quartz when it is exposed to water. The silanol groups are the major sites for water adsorption on silica, due to its ability to donate or accept hydrogen bonds with different strengths. Higher amount of silanol groups results in a more serious water adsorption at the surface of quartz.

Gee *et al.* [37] analyzed the amount of silanol groups present at the surface of quartz. Around half of the amount of silanol groups were removed at  $500^\circ\text{C}$ . A minimum amount of silanol groups at the surface was observed when the quartz was heated to a temperature above  $1000^\circ\text{C}$ . The actual amount of remaining OH groups at the surface was estimated to be ca.  $0.4/\text{\AA}^2$ . A general conclusion that the amount of silanol groups decreases with the increase of the temperature was drawn.

Ulvensøen [38] investigated the effects of different drying parameters (temperature and period) for high purity quartz sands on their hydroxyl groups and water adsorption behaviors. The quartz sand sample was the same as the one in this project, and the drying matrix was the same as the one shown in Table 3.3.

The measurement was done by Diffuse Reflectance Infrared Fourier Transform Spectroscopy (DRIFTS). An environment where water was present was created to study the water adsorption behaviour of different dried quartz sands. The results showed that the water adsorption was severe for sample 100°C 24hr and 600°C 1hr, which is shown in Figure 2.9. For the quartz sands that were heat treated at 900°C or above, the water adsorption was very little. The less water absorption observed for samples which the sands were dried at 900°C or above was related to the removal of more isolated silanol groups above that temperature.

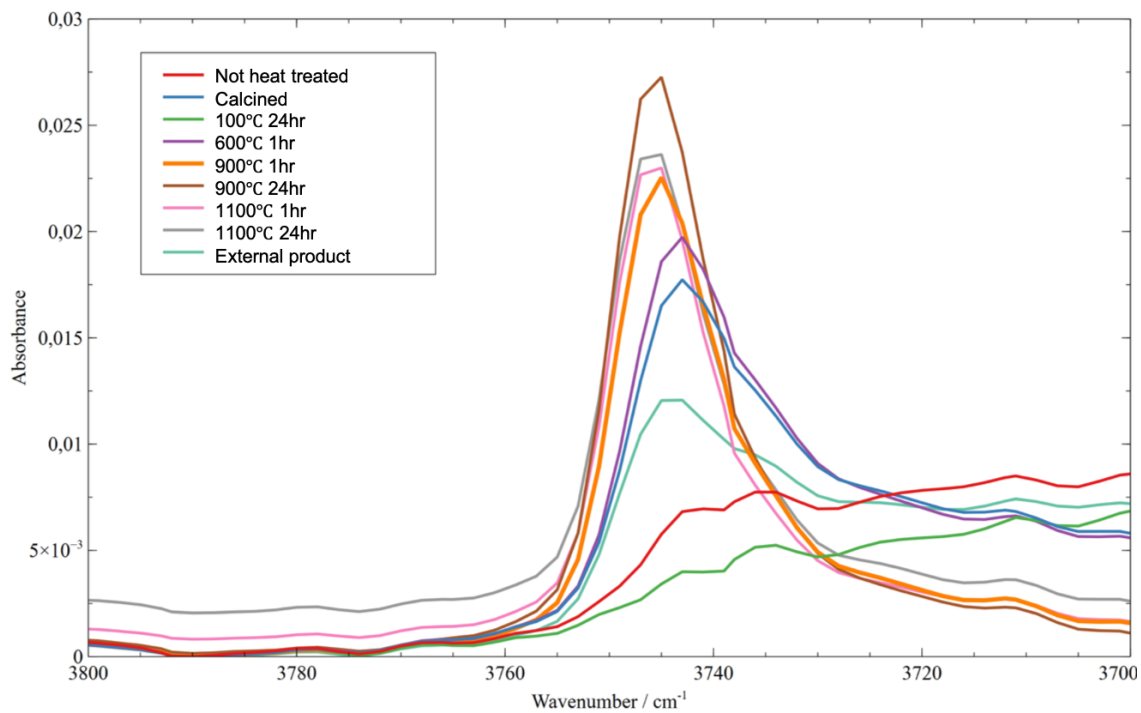


**Figure 2.9** Absorbance spectra of different quartz sand samples with the wavenumber from 3800 to 3700  $\text{cm}^{-1}$ . The peaks are corresponding to the "free" OH. Actual sample name was hidden due to commercial reason [38]

## 2.4 Fused silica for Czochralski process

### 2.4.1 Manufacture and composition of commercial fused silica crucibles

The manufacturing process of commercial fused silica crucibles are normally confidential, but the general production process could be found in different published patents. The purity of the raw material is one of the most critical factors in the production of fused silica with any fusion technology, which greatly

affects the quality of the product. The general preparation steps of quartz powder before the fusion involve sieving and often purification in acid leaching, followed by washing with de-ionized water and drying.

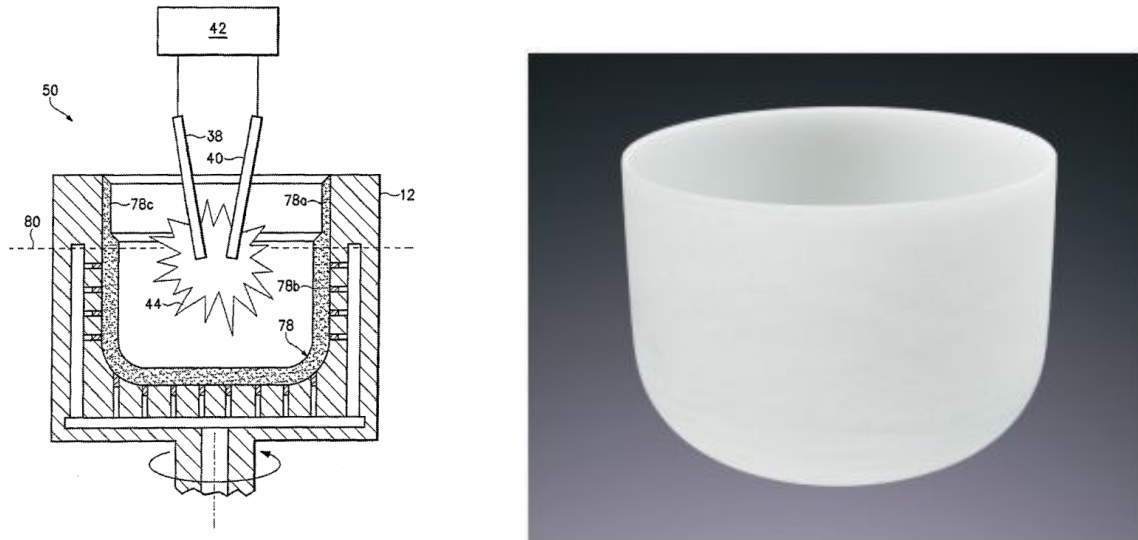


**Figure 2.10** Left: A patented quartz crucible manufacturing for CZ-silicon production [39].  
Right: A finished fused silica crucible for CZ process [40]

Figure 2.10 shows the manufacturing setup for a quartz-glass crucible and a finished crucible. First, silica is fed by a spatula into a rotating graphite mould (12). The rotating mould generates centrifugal force and keeps the silica against the mould walls. Then, the electrodes are lowered into the crucible. A high temperature electric arc generated by the electrode (38, 40) causes the sintering of the quartz sand, and the sands fuse into amorphous glass gradually. During the fusion process, a vacuum is applied from the outer surface of the mould, which sucks out the entrapped air and ensures a bubble-free inner layer of the crucible, as the melting front is moving towards the outer layer of the crucible. Half way through the production process, the vacuum is turned off, and, as a consequence, the bubble composite layer forms and exists as the outer layer of the crucible [39].

Figure 2.11 shows the viscosity of a commercial fused quartz product at different temperatures. Focusing on the viscosity at the CZ pulling temperature range (typically 1400°C to 1600°C), it can be seen that the viscosity range is ca. 8.5 - 10.5 log(Pa·s).



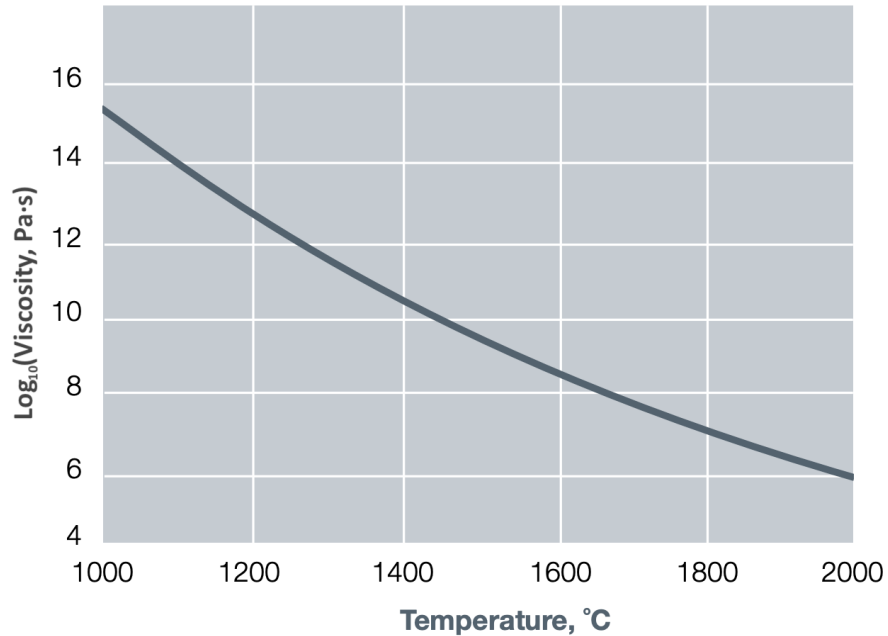


**Figure 2.11** Viscosity of a type of commercial fused quartz in a temperature range of 1000° to 2000°C. Data provided by Momentive<sup>TM</sup>

#### 2.4.2 Effects of devitrification

As discussed in Section 2.2.3, cristobalite develops on the surface and possibly at the interior when the fused silica is re-heated. Cristobalite exists as a white, brittle, and non-transparent layer on the surface of the fused silica.

Formation of cristobalite layer could be favorable for the CZ process. As the viscosity of the crucible decreases at elevated temperatures, the presence of the cristobalite layer mechanically assists the crucible to maintain its shape. These occurrences come with a condition that cristobalite should exist as a complete layer that covers the quartz crucible surface. The achievement of a complete layer of cristobalite is limited by the presence of foreign particles on the inner surface of the crucibles. The particles may act as nucleation centres and cristobalite exists as islands instead of a continuous layer. These cristobalite "islands" can be detached as particles into the silicon melt, which introduces structural loss-like dislocation in the ingot and causes reduced mechanical properties of the silicon. Besides, the high porosity of the cristobalite layer can cause the impurities and bubbles to enter the silicon melt during the pulling process. Devitrification agents (typically Ba<sup>2+</sup> are commonly used to coat or dope the surface of the material in

order to obtain an even cristobalite layer, as discussed in Section 2.2.3.

The transition to  $\beta$ -cristobalite is irreversible. After the devitrification takes place, the fused silica experiences transformation from  $\beta$ -cristobalite to  $\alpha$ -cristobalite. Due to the structural transformation from cubic to tetragonal, it results in a severe decrease in volume as shown in Figure 2.2. Structural defects such as cracks will likely form in the cristobalite layer because of the shrinkage of cristobalite and the thermal expansion coefficient mismatch of the whole material which both silica glass and cristobalite phases are present [41]. This cooling effect is the main reason for the fused silica crucible to become non-reusable after each pulling cycle, and it incurs a high cost (ca. 30% of the total cost [42]) to the production of silicon ingots.

### 2.4.3 Bubbles

The common impurities in the quartz powder shown in Table 2.3 have major effects on bubble formation during the fusion process. Acid leaching is often required to reduce the contaminants in quartz powder. Guerra *et al.* [43] studied the difference of bubble concentration of fused silica produced by two types of quartz powders (QPSR and QPKY) with different treatments. QPSR was sieved to obtain the quartz powder in a specific particle size range (# 80-120 mesh). Part of QPSR was used without further purification process, and the another part was purified by acid leaching. For the imported commercial quartz powder, QPKY, the as-received powder was used without any additional treatment. The concentrations of the impurities of these two as-received quartz powders are provided in Table 2.4.

**Table 2.4** Concentrations of impurities of quartz powder QPSR and QPKY (ppm)

Sample	Al	Ca	Fe	K	Li	Na	Ti	Others	Total
QPSR	10.6	35.7	2.2	ND	1.3	ND	1.0	5.3	56.0
QPKY	6.0	0.2	0.3	0.4	0.3	0.9	4.5	NA	NA

ND - Not detected, NA - Not available

The production of the fused silica was done by Verneuil process (flame fusion). The quartz powder was thrown directly in the flame, and the growing ingot formed. Two critical glass production parameters and

the bubble contents in the silica glasses are shown in Table 2.5. The bubble content in the silica glass produced from QP.KY, which in general has lower impurity contents, was significantly lower. The reduction in the average bubble content after the leaching process was identified. The bubble contents in QP.SR glass were reduced to the same levels as the average content in the QP.KY glass after the leaching process.

**Table 2.5** Process parameters used for silica glass production and the bubble concentration in the silica glass samples produced from two different quartz sands with different treatment [43]

Sample	Ratio (LPG/O <sub>2</sub> )	Temperature (°C)	Bubble (#/mm <sup>3</sup> )
QP.KY (as-received)	0.30	1550	0.38 ± 0.15
QP.SR (sieved)	0.26	1750	3.05 ± 0.39
QP.SR (leached)	0.26	1700	0.33 ± 0.04

The bubble content in the leached QP.SR was also presented with a matrix consisting of different fusion temperatures and the ratios of GLP/O<sub>2</sub>, which can be seen in Table 2.6. It was noticed that these parameters also have major influence on the resulting bubble concentration in the glass. The glass with the lowest bubble concentration was produced at 1600°C with the ratio of GLP to O<sub>2</sub> of 0.23.

**Table 2.6** The effects of fusion temperature and ratio (GLP/O<sub>2</sub>) R<sub>z</sub> on bubble concentration (#/mm<sup>3</sup>) in the silica glass produced from leached QP.SR

T (°C) / R <sub>z</sub>	0.23	0.26
1600	0.25 ± 0.08	1.08 ± 0.6
1700	0.76 ± 0.11	1.11 ± 0.23
1800	0.89 ± 0.27	0.59 ± 0.14

The bubble characteristics of two quartz crucible samples from two different suppliers (A and B) was studied by Paulsen *et al.* [44]. It was completed by the use of Micro X-Ray Computational Tomography ( $\mu$ -CT) with 3D analysis. The porosities of both as received samples were found to be ca. 0.4%. The numbers of bubbles per volume in A and B were 34 and 54 mm<sup>-3</sup> respectively. These findings indicate that sample B had more but smaller bubbles compared to sample A, considering that they had very similar porosities. Referring to bubble size distribution of A and B from 3D analysis, which is shown in Figure 2.12, the peaks of bubble diameters of as received A and B occurred at ca. 20  $\mu$ m. The bubble volumes were

measured again after the crucible samples were heat treated at 1400°C for 24 hours. After the heating, the bubble volumes of sample A and B were found to increase for 76% and 95% respectively. Their bubble size distributions also changed from 30 - 70  $\mu\text{m}$  to 50 - 120  $\mu\text{m}$ .

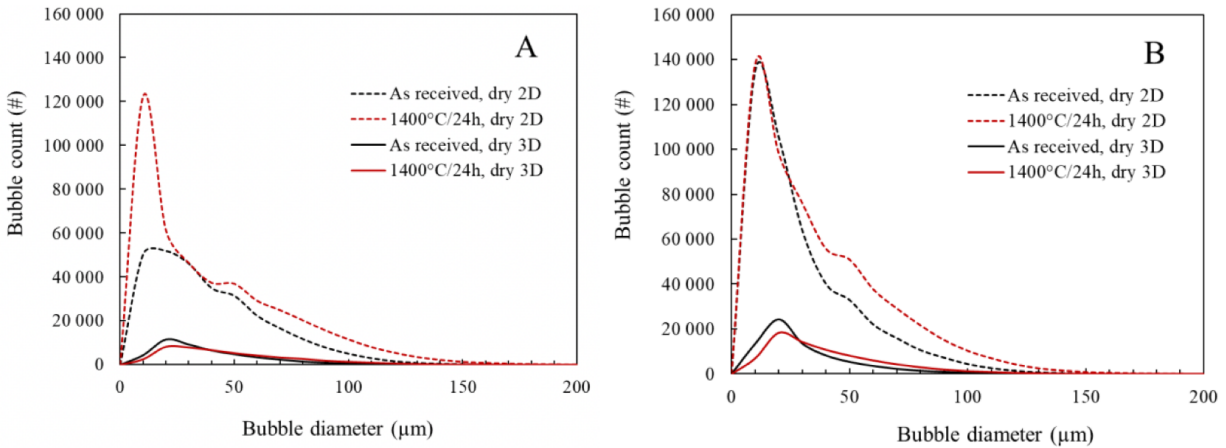


**Figure 2.12** Bubble size distribution of, Left: sample A, Right: sample B [44]

The effect of storage conditions (humidity) for fused silica crucible was also studied. One of the crucible samples was kept in an oven at 200°C for 72 hours, while the another one was kept in distilled water at 20°C for 72 hours. The crucible samples' bubbles were characterized before and after they were being heated at 1400°C for 24 hours. The results showed that there was not a notable difference in their bubble distributions between the "dry" and "wet" treated crucible samples. As the entrapped gas bubbles in the crucible contribute to the sagging of crucible at high temperature range, the results indicated that the humidity of the storing environment of the crucibles does not have significant effect on the crucible performance during CZ process.

## 2.5 Characterization

### 2.5.1 Measuring hydroxyl content in fused silica

Fourier Transform-Infrared Spectroscopy (FTIR) is a characterization technique which is used to obtain the infrared spectrum of a liquid, solid or gaseous material. When a light beam strikes a sample, different molecules in the sample selectively absorb light at specific wavelengths, depending on molecules' vibration

energy levels. The absorption causes the change of the dipole moment of the molecules, as the vibration energy levels of the molecules excite from the ground state to the excited state. The loss in intensity at different wavelengths gives a spectrum with absorption peaks that indicate the present molecular groups in the matrix [45]. For FTIR, instead of using a monochromatic light source, a poly-chromatic beam with many frequencies is used. The frequencies are then changed several times to obtain new data points. Afterwards, all the data are processed by Fourier-Transformation in a computer and an IR-spectrum is generated.

A typical FTIR spectrometer consists of a light source, sample compartment, interferometer, detector, amplifier, A/D converter, and a computer. The Michelson interferometer, a configuration of mirrors, is used in FTIR. The light beam passing through the interferometer is splitted into two by a beam splitter. One of them is transmitted towards the fixed mirror, and the another one is transmitted towards the moving mirror.

Measuring the OH-content of the fused silica is one of the focuses in this work. Sloots (on behalf of Philips Lighting) [46] summarized the methods that can be used for measuring the low OH-content in fused silica. A spectrometer named Bruker Vertex 80v with special configuration was found to be capable to detect the OH level under 0.05 ppm with a quick measuring time (1 min). This method was adopted in many similar projects and also the previous work of this project. The calculation of the OH-content involves the usage of a Matlab's script, which has the features of baseline calculation, peak search, and the calculation of the OH-content. With the thickness of the sample, the optical density  $\beta$  could be calculated with Beer Lambert's law, shown in Equation 2.5:

$$\beta = \frac{1}{d} \times \log\left(\frac{1}{T_{min}}\right) \quad (2.5)$$

The calculation of OH-content was done by multiplying the optical density by a conversion factor, shown in Equation 2.6 and 2.7:

$$OH(ppm) = \beta \times factor \quad (2.6)$$

$$f_{factor} = \frac{M_{OH} \times 10.000}{e_{OH} \times \rho_{glass}} \quad (2.7)$$

where the molar weight of OH,  $M_{OH} = 17 \text{ g/mol}$ , the density of glass,  $\rho_{glass} = 2.21 \text{ g cm}^{-3}$ , and the absorption coefficient,  $e_{OH} = 77.5 \text{ mol}^{-1} \text{ cm}^{-1}$ .

### 2.5.2 Viscosity measurement

Viscosity is a measure of resistance to motion (flow) under applied force. The viscosity of the quartz crucible is dependent on the OH level of the crucible.

A suitable type of visco-meters should be adopted according to the viscosity range of the measured sample. A fused silica crucible has a viscosity of typically over  $6.6 \log(\text{Pa}\cdot\text{s})$  above the softening point. With this range of viscosity, the suitable methods include the penetration method and the beam bending method.

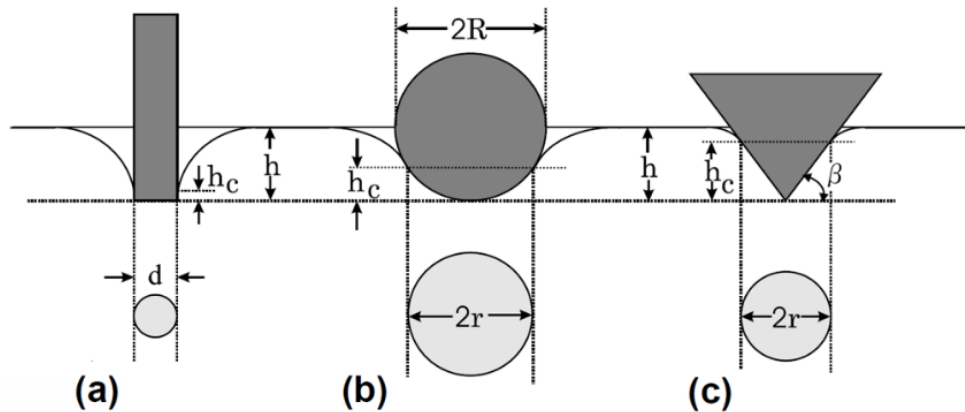


**Figure 2.13** Geometry and coordinate system of (a) flat-ended, (b) spherical and (c) conical indentations [47]

The penetration method can be further classified into different groups according to the shape of indentors. Penetration can be performed by a circular rod with a flat, sphere, or cone end. Due to the simplicity and the adaptation to the available equipment, a circular rod with a flat end was the best option for the samples in this project [48]. Equation 2.8 shows the relationships between indentation rate, viscosity, and geometry factor, which is illustrated in Figure 2.13. With the steady state indentation rate and the rod diameter, the viscosity can be calculated by Equation 2.9.

$$v_s = \frac{2(1-\nu)P_0}{k_f \pi d} \frac{1}{\eta} \quad (2.8)$$

$$\eta = \frac{(1-\nu)P_0}{2d v_s} \quad (2.9)$$

where  $v_s$  is the rate of indentation at steady state,  $\nu$  is the Poisson's ratio of the glass,  $k_f$  is a constant which equals to  $4/\pi$ ,  $\eta$  is the glass viscosity,  $P_0$  is the indentation load, and  $d$  is the rod diameter.

The viscosity can also be expressed by Arrhenium equation (Equation 2.10):

$$\eta = \eta_0 e^{E_a/RT} \quad (2.10)$$

where  $E_a$  is the activation energy for viscos flow,  $R$  is the universal gas constant ( $8.314 \text{ J}\cdot\text{K}^{-1}\text{mol}^{-1}$ ),  $T$  is the temperature in Kelvin, and  $\eta_0$  is a constant.

A straight line is expected by plotting viscosity in log scale with the slope  $E_a/R$  (Equation 2.11). The activation energy of viscous flow can be calculated with the results from the measurement.

$$\ln \eta = \ln \eta_0 + \frac{E_a}{R} \frac{1}{T} \quad (2.11)$$

Viscous flow is often considered as a thermally activated process. The molecules need to overcome the activation energy barrier ( $E_a$ ) created by the resistance of the surrounding units [49]. Activation energy of viscous flow decreases with the increase of temperature. The major change of activation energy of viscous flow occurs near the glass transition temperature. The rate of change depends on the enthalpy of formation of disordered lattice defects (i.e. broken bonds) [50].

### 2.5.3 Bubble density characterization

There is a lot of different techniques that are suitable for bubble density measurement. For fused silica, Micro X-Ray computational tomography ( $\mu$ -CT) has been used for this purpose.  $\mu$ -CT is a prevalent technology that offers non-destructive imaging of morphological structures investigation. It involves the recording of 2D images, and the 2D images can be combined to generate a 3D reconstruction. The main components of a typical  $\mu$ -CT include a penetrating ionizing radiation, a sample manipulator, and a detector.

Paulsen *et al.* [44] studied the bubble distribution in the quartz crucibles for CZ process by  $\mu$ -CT. The adopted model of  $\mu$ -CT (Nikon XT H225ST NC) offers the possibility to detect bubbles that have a diameter of as small as 9  $\mu$ m. The accuracy of the number of bubbles and bubbles' volumes was evaluated by comparing the 2D and 3D analysis. It was concluded that both 2D and 3D analysis gave accurate estimation of bubble volume. For the number of bubbles, 3D analysis is preferred as 2D analysis gave up to 9 times higher number of bubbles than the actual number.



### 3 Experimental

#### 3.1 Materials and apparatus

Quartz sand A was the only raw material involved in this project. It was used for producing fused silica by drying with different parameters (See Table 3.3) and melting. The quartz sand A involved in this project was solely supplied by TQC, and stored in a plastic container. The actual name of the quartz sand was abbreviated due to commercial reasons. In the following sections, the fused silica samples will be referred by their drying temperatures and periods directly, followed by the number of the parallel experiment. For example, the fused silica sample that was dried at 900°C for 1 hour, was be named 900-01.

Table 3.1 shows the chemical analysis of quartz sand A, provided by TQC. This type of quartz sand is very suitable for the production of crucibles for CZ purpose [51].

**Table 3.1** Concentration of impurities in quartz sand A (wt ppm) [51]

	Typical Value
Al	13
B	≤0.1
Ca	0.5
Co	≤0.01
Cr	≤0.01
Cu	≤0.01
Fe	0.2
K	0.5
Li	0.4
Mg	<0.1
Mn	<0.1
Na	0.8
Ni	≤0.01
Ti	1.2

The summary of the apparatus and equipment involved in this work is presented in Table 3.2. Both

ENTECH furnaces are owned by SINTEF Industri, and maintained by P. I. Dahl (Senior Research Scientist at SINTEF Industri) throughout this project. The novel setup used for viscosity measurement was built by O. Paulsen (Former senior scientist at SINTEF Industri), and it is currently not commercially available.

**Table 3.2** Equipment details of all experiments

Equipment	Application	Model & brand
High temperature furnace	drying of quartz sands	Nabertherm HTC 03-14
High temperature furnace	Melting of heat-treated quartz sands	ENTECH-ECF 20/18
Cut-off machine	Fine sample cutting	Struers Minitom
Polishing machine	Sample polishing	Labopol-21
Ultrasonic bath	Sample cleaning	Branson 3800
XRD	Phase composition analysis	Bruker D8 Focus
FTIR	OH level measurement	Bruker Vertex 80v
$\mu$ -CT	Bubble characterization	Nikon XT H225ST
High temperature furnace (with displacement transducer)	Viscosity measurement	ENTECH-STX/17

### 3.2 Procedure

#### 3.2.1 Fused silica production

The production of fused silica samples involved two major processes, which were drying and melting. The purpose of drying was to reduce the water content in the quartz sand before they were melted. The drying and melting of quartz sand were completed in the same experiment and oven. The production of all the silica samples (except 100-24) were performed by filling a self-produced alumina crucible with pressed raw material quartz sand A until the sand reached the ventilation windows. This production was done in an open furnace (i.e. with ambient air). The overall heating profile for the



**Figure 3.1** Crucible for fused silica production

experiment is shown in Figure 3.2. The temperature of the furnace firstly stopped at a drying temperature for a drying period, according to the combinations in the matrix shown in Table 3.3. Afterwards, the temperature was increased directly to the melting temperature (1800°C). The furnace was kept at 1800°C for 5 hours. Different cooling rates were used in different temperature ranges during cooling. A higher rate (300°C/hour) was used until the melt reached the glass formation range (1300°C). A much lower rate (50°C/hour) was used from 1300°C to 1000°C for annealing, followed by a rate of 200°C/hour until room temperature. A new crucible (except the top alumina plate) was used for each test.

Drying and melting during the production of sample 100-24 were performed separately in two different ovens. The reason is that the melting oven is not capable to keep the temperature stable below 400°C. drying was performed with the method described in Section 3.2.2. After the drying was finished, the heat treated sand was melted in the melting furnace (ENTECH-ECF 20/18). The heating profile used for melting was the same as shown in Table 3.2, except that the drying step was skipped.

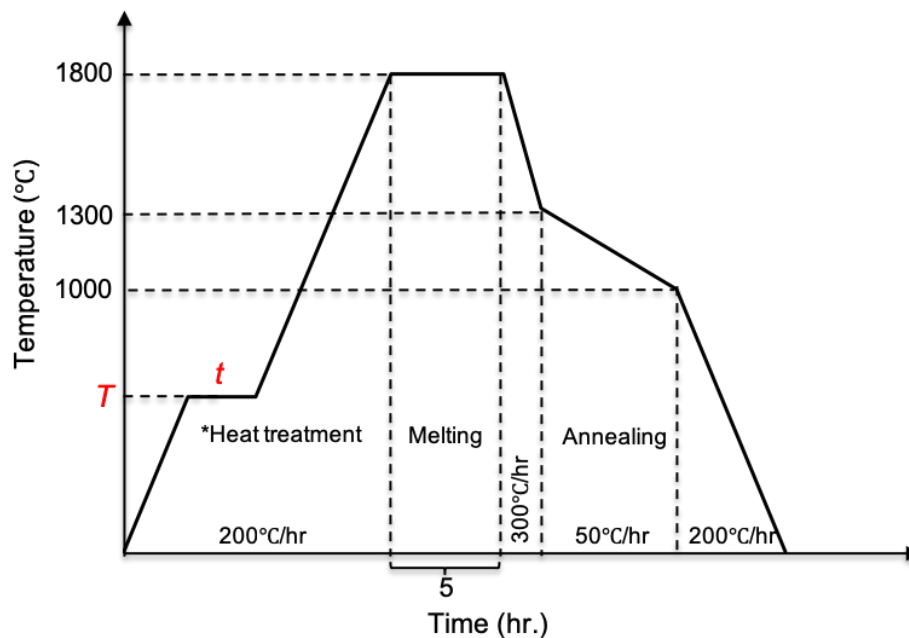


**Figure 3.2** Heating profile for melting of quartz sand. Variables  $T$  and  $t$  represent the drying temperature and holding time shown in Table 3.3

The crucible used for melting consisted of an alumina body cut from a long alumina tube, with a top and bottom alumina plate, as shown in Figure 3.1. The production of the crucible body was handled by P. I.

Dahl (Senior Research Scientist at SINTEF Industri). The crucible body had an outer and inner diameters of ca. 85 mm and 75 mm respectively, and a height of ca. 100 mm. The thicknesses of the top and bottom alumina plates were ca. 3 mm and 8 mm respectively. 4 ventilation windows at 2 sides at the top part of the body were made. Each window had a height of ca. 2 mm and an arc length of ca. 60 mm. The highest and lowest window located at ca. 5 mm and 25mm, respectively, from the top of the crucible body.

**Table 3.3** Drying profile prior to melting, with heating rate of 200°C per hour in ambient air

Sample notation	Temperature $T$ (°C)	Holding time $t$ (hr.)
<b>100-24</b>	100	24
<b>600-01</b>	600	1
<b>900-01</b>	900	1
<b>900-24</b>	900	24
<b>1100-01</b>	1100	1
<b>1100-24</b>	1100	24

### 3.2.2 drying of quartz sand

A part of quartz sand was without melting for extra characterization and future use. The quartz sand was dried in an cylindrical alumina crucible with an outer diameter of 50 mm, covered with an alumina lid with a thickness of 3 mm (with a small gap during drying for ventilation), as shown in Figure 3.3. Each drying was run in the open furnace in parallel with 2 crucibles. The crucibles were washed and brushed with soap before each drying. The crucibles were filled with pressed quartz sand A until the crucibles were full. The weights of the quartz sands before and after the drying

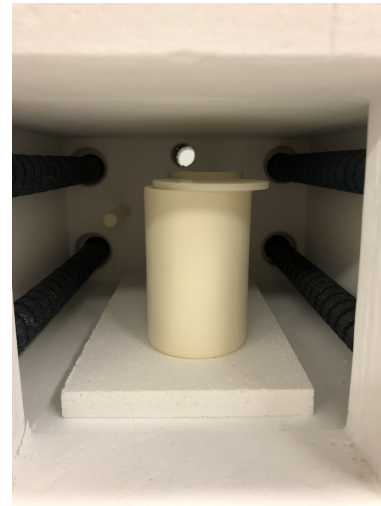


**Figure 3.3** Furnace compartment

were measured. The quartz sands were heated according to the matrix shown in Table 3.3. After the drying was finished, the crucibles with the dried sands were removed from the furnace at 100°C, and immediately placed inside the desiccator until they were completely cooled to avoid re-absorption of water. Same crucibles were used for drying with all profiles. The dried sands were stored in air-tight plastic containers.

### 3.2.3 Fused silica sample cutting

The fused silica samples were in cylindrical shapes before they were cut, as illustrated in Figure 4.7. It was firstly separated from the crucible. Figure 3.4 shows the concept of the samples extraction. The top layer (surface layer) of the fused silica with the thickness of 5 mm was separated for each sample. The dimension of remaining part (bulk layer) varied among different samples, depending on how much the glass flaked during cutting. The sides of the sample were also separated.

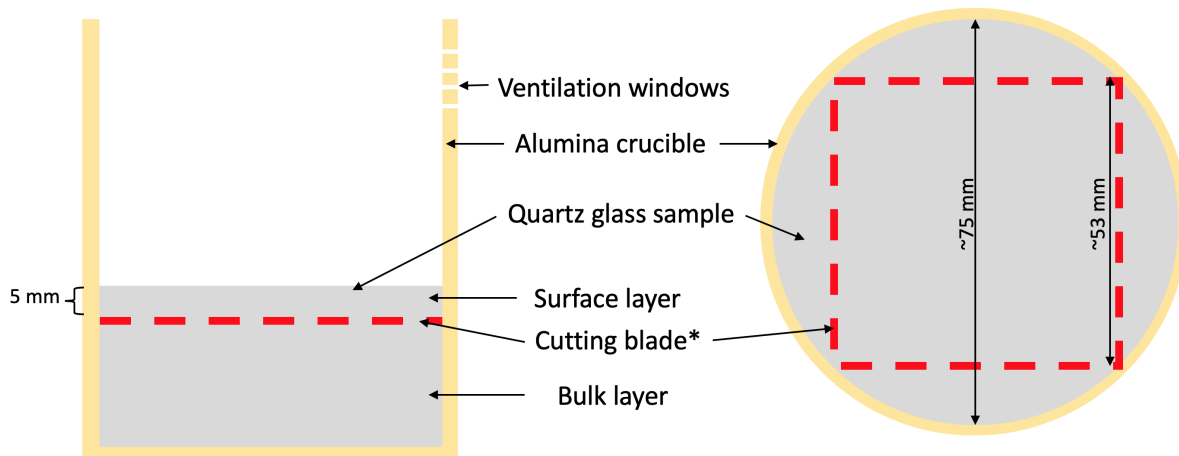


**Figure 3.4** Schematic of coarse sample cutting; Left: side view of the sample, Right: top view of the sample. \*Thickness of the coarse cutting blade was ca. 3 mm

Only the center part of the glass was used for characterization. The centre part was further cut into 4 cubes, which is illustrated in Figure 3.5. The vertical distances from the surface of the samples to the removed top surface was measured.

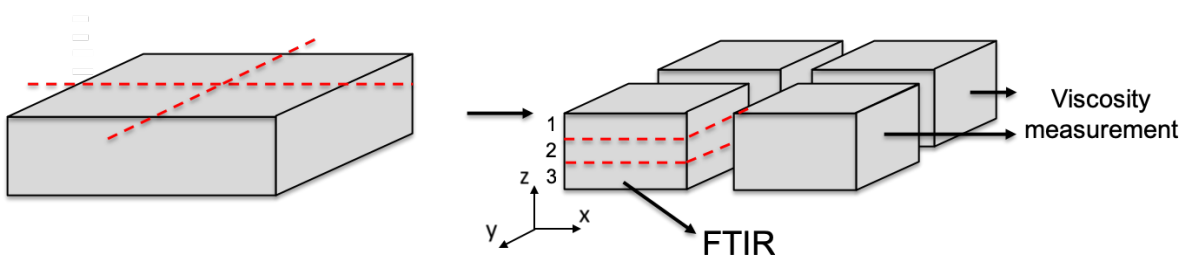


**Figure 3.5** Schematic of fine sample cutting; Left: after removal of top and bottom layers and the sides, Right: after further separated into 4 samples for different experiments, with the remarks of the purposes for each sample. Thickness of the fine cutting blade was ca. 0.5 mm

### 3. EXPERIMENTAL

---

Coarse cutting was performed by P. I. Dahl (Senior Research Scientist at SINTEF Industri), followed by fine cutting according to the dimension required for each characterization method. Figure 3.6 shows how the coarse and fine cutting of fused silica sample were done.



**Figure 3.6** Cutting of fused silica sample. Left: coarse cutting, Right: fine cutting

#### 3.2.4 OH-content measurement

One of the fused silica cubes were further separated into 3 slices by a high precision cutter for FTIR, as shown in Figure 3.5, The yield samples were marked with number 1 to 3. Number 1 represented the slice that is closer to the top surface of the glass and number 3 represented the slice that is closer to the bottom. The yielded 3 samples had a thickness of ca. 2.5 mm. The dimension of each sample was maintained at ca. 15 x 15 x 2 mm (L x W x H). Polishing of both sides of the samples was performed. The polishing was done manually with SiC paper. The polishing steps are presented in Table 3.4. After the polishing, the samples were cleaned with laboratory ethanol in an ultrasonic cleaner for 10 minutes.

OH levels of the 3 slices for each sample were measured by FTIR. The prepared fused silica samples were taped onto the sample holder of the setup in the FTIR spectrometer compartment, which is shown in Figure 3.7. The measured position was confirmed by observing the position of red laser dot on the sample. The equipment was filled with liquid nitrogen for cooling. The compartment was evacuated to a

**Table 3.4** Polishing steps

Grid	Duration (min./side)
120	0.5
320	1
500	1
800	1.5
1200	2
2400	2
4000	3

pressure of ca. 2.1 hPa for each measurement. The thickness of each measured position was measured, and the calculation of the OH level at each position was done with the corresponding thickness in order to minimize the calculation error.

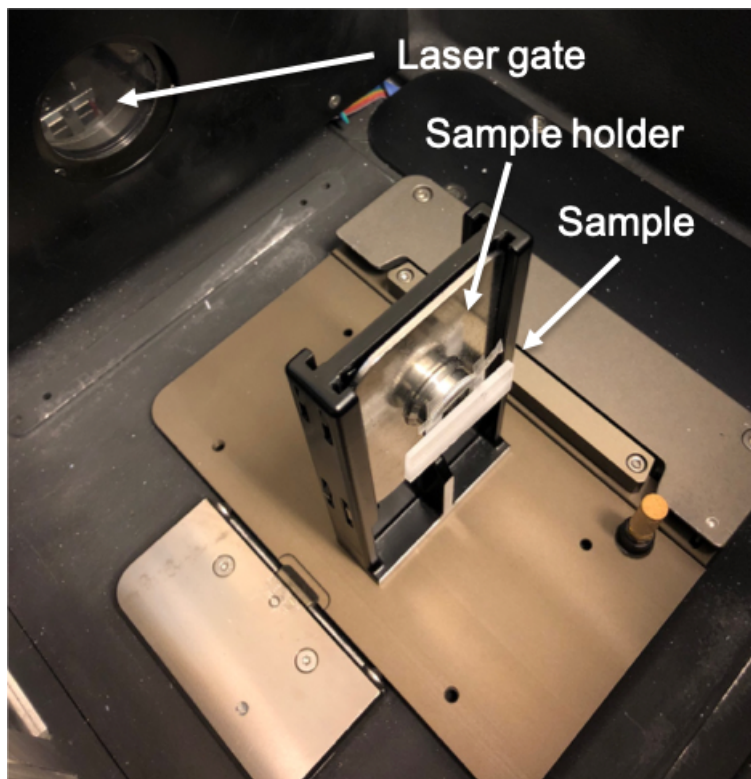


**Figure 3.7** The main components in the FTIR compartment during the measurement of OH-contents in fused silica samples



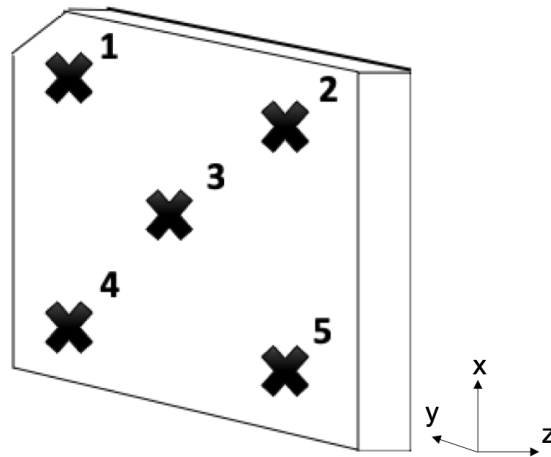


**Figure 3.8** Examination positions on a fused silica sample

The OH level was calculated by processing the spectrometry raw data by running a script in a programming software Matlab. The script can be found in Appendix A.1 [46]. The script uses a baseline fitting function to calculate the minima depth  $T_{min}$ . The data within the range of  $3365\text{ cm}^{-1}$  to  $3850\text{ cm}^{-1}$  were used for calculation.

### 3.2.5 Viscosity measurement

Two viscosity measurements were performed in parallel for each sample. After the cutting, the surface of each sample, which was closer to the top, was polished manually by SiC paper. The polishing steps were the same as the one adopted for FTIR's sample preparation, which are shown in Table 3.4. The dimension of each sample was maintained at ca.  $15 \times 15 \times 10\text{ mm}$  (L x W x H). The top (polished) and bottom surfaces were kept as parallel as possible, by measuring the thicknesses of four corners. The samples were cleaned with laboratory ethanol in an ultrasonic cleaner for 10 minutes, after the polishing.

An experimental setup including a high temperature furnace, a displacement transducer (LVDT), and a type-B thermocouple, which is owned by SINTEF, was used for the measurement. The setup is shown in Figure 3.9.



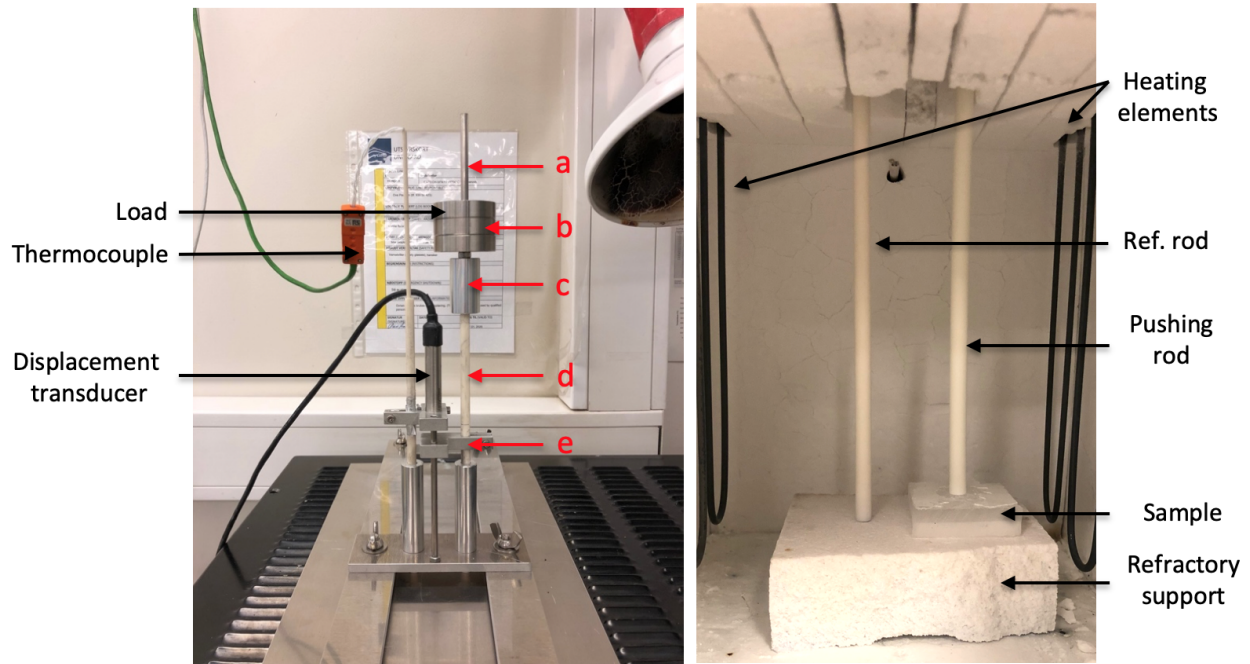


**Figure 3.9** Viscosity measurement setup, Left: External components, Right: Internal components. Elements contributing to total loading weight are marked by letter a to e

Before each experiment started, the tip of the pushing rod which was in contact with the sample was cut due to the reaction with the previous sample. The pushing rod was also checked visually, and it was replaced with a new one if the rod bended. Afterwards, the total loading weight and the diameter of the pushing rod were measured. For each test, a fused silica sample was placed on the support, and the polished surface was in contact with the pushing rod.

The compartment was heated up with a heating profile shown in Figure 3.10. The experiment was done in ambient air environment. There were four temperature steps for the measurement, which were 1400°, 1450°, 1500°, and 1550°C. The dwell for the first two temperature steps was 1 hour, and that for the last two temperature steps was 0.3 hour. The furnace compartment was first heated up to 1050°C at the rate of 250°C per hour. Afterwards, 400°C per hour was used until the last temperature step (1550°C) was finished. 300°C per hour was used as the cooling rate of the compartment until it reached the room temperature.

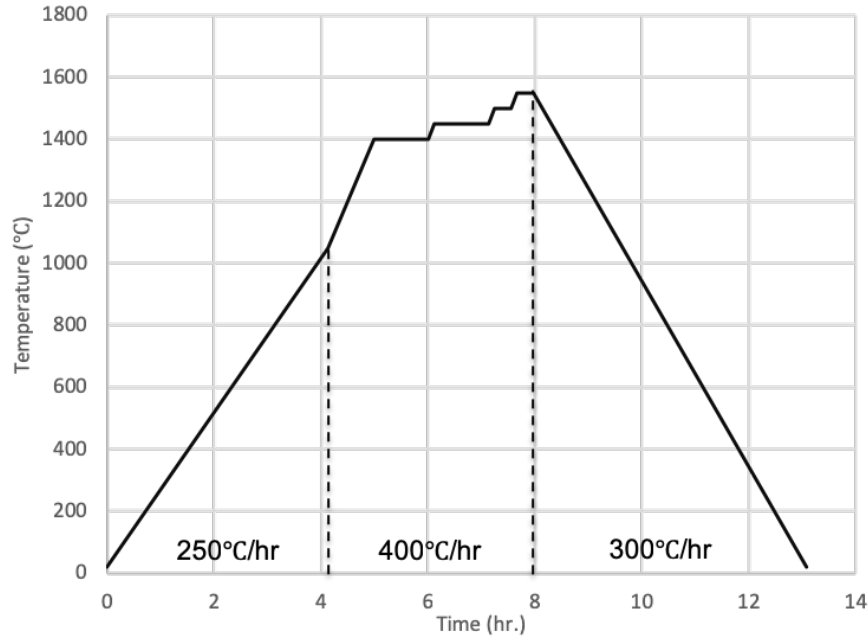


**Figure 3.10** Heating profile for viscosity measurement

Temperature and VDC (represented by  $x$ ) were two output data from the viscosity measurement. In order to obtain the correct displacement of the pushing rod, a polynomial, which is shown in Equation 3.1, was used for the calibration of the displacement transducer. The calibration was done by the supplier of the displacement transducer, and the information was provided by O. Paulsen (Former senior scientist at SINTEF Industri). The net creep in mm was calculated by subtracting the initial position ( $t = 0$ ) by the position at time (denoted by  $t$ ).

$$Pos = A_0 + x \times (A_1 + x \times (A_2 + x \times (A_3))) \quad (3.1)$$

where  $A_0$  is -0.1063,  $A_1$  is 1.224,  $A_2$  is -0.00643, and  $A_3$  is 0.000777.

A plot of displacement in meter against the time in second at each temperature step was made to obtain the creep rate at each temperature step. As the creep was not stable at the beginning of each step, only the last 90 data points at each temperature step were taken for calculation. Trendline function in Excel was used to obtain the creep rates (slopes). Equation 2.9 was applied for calculating the viscosity. The Poisson's ratio and rod diameter used in this measurement were 0.2 and 6.4 mm respectively. The loading

was measured before every test and updated for calculation of the viscosity. Components that contributed to the loading are indicated in Figure 3.9 by letter a to e.

#### 3.2.6 Bubble characterization

The bubble distribution and density of 3 fused silica samples (600°C for 1 hour, 900°C for 1 hour, and 1100°C for 1 hour) were studied by  $\mu$ -CT, which is capable to generate 3D reconstruction of all bubbles by scanning the whole sample. The samples for FTIR (number 1) were used for this characterization, and no further preparation was needed. Variations of the samples' dimensions were tolerated as only a fixed volume ( $15 \times 15 \times 1.8 \text{ mm}^3$ ) was examined at image analyzing stage afterwards.

All the samples were stacked and placed in a special plastic cylindrical container, and the container was loaded to the machine. There were 6283 scans for a 360-degree scanning. The pictures acquired by the equipment were compiled to generate a 3D reconstruction. Each "stack" consists of ca. 1000 pictures. The resolution of the generated 3D model was limited to 1 voxel (a 3D pixel) which is approximately  $9.1 \mu\text{m}$ . The operation of the equipment and the image file generation were completed by S. Rørvik (SINTEF Industri). A computer program ImageJ with a plugin called "BoneJ" [52] was used for bubble analysis. A function called "Particle Analyser" provided by this plugin was used to obtain the characteristics of all single detected bubbles. The measuring limit of the image analyzing function was  $9 \mu\text{m}$ , which means bubbles with diameters under  $9.1 \mu\text{m}$  were not detected.

#### 3.2.7 X-ray diffraction

All heat treated quartz sands and fused silica samples were taken to perform XRD measurement. This machine model (D8 Focus) equipped with LynxEye<sup>TM</sup> SuperSpeed Detector operates with  $\text{CuK}\alpha$  radiation with a wavelength of  $1.54 \text{ \AA}$ .

Each type of heat treated quartz sands was crushed for ca. 5 minutes to achieve a suitable average particle size. The surface layer of each fused silica sample was polished with the steps presented in Table 3.4. The polished samples were cleaned with ethanol in an ultrasonic cleaner for 10 minutes.

For dried quartz sand samples, a typical sample holder was used. It was filled with pressed quartz sand samples. For fused silica or solid samples, a deep sample holder was used. Small amount of rubber was placed underneath the sample in order to fix the position of the sample. The height of the measured surface of the fused silica sample was aligned with the the edge of the sample holder. The parameters for the experiment is shown in Table 3.5.

**Table 3.5** XRD configuration parameter for measuring both heat treated quartz sands and fused silica

<b><math>2\theta</math> range</b>	<b>Steps</b>	<b>Step time</b>	<b>Divergence slit</b>
15° - 100°	6612	0.25 s	1 mm

## 4 Results

### 4.1 Validating experiments

Different validating experiments were performed before the main part of the experiments began, due to the use of new process and novel experimental setup. The results that had important implications are presented in this section.

#### 4.1.1 Production of fused silica

The development of the process for producing fused silica samples were started with a different setup. Several trial experiments were performed. The melting experiment parameters were revised after every trial test. A rectangular alumina with molybdenum lining was firstly used for melting of quartz sand. The holding period at the melting temperature ( $1800^{\circ}\text{C}$ ) was 1 hour instead of 5 hours. Figure 4.1 shows one of the resulting fused silica samples after a trial melting test with the mentioned setup. It can clearly be observed that there was a large amount of cristobalite existing on the surface. Some parts of the molybdenum lining were attached to the silica sample.

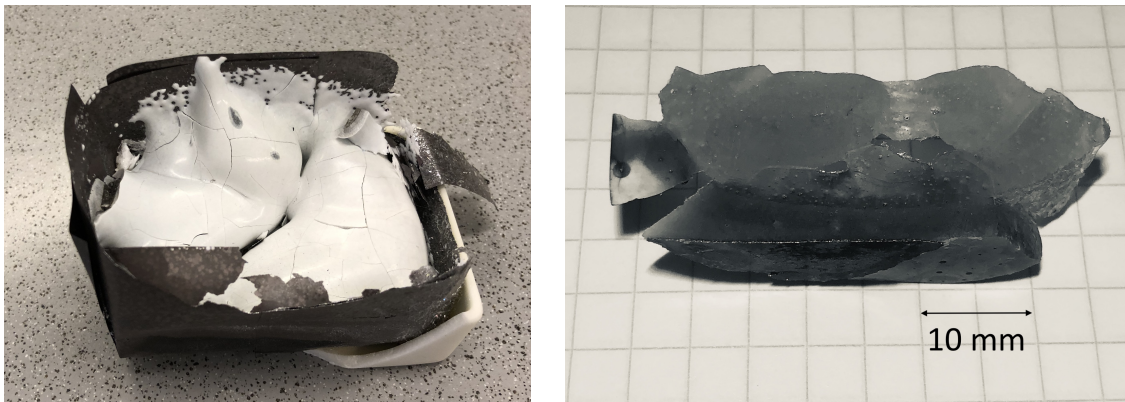


**Figure 4.1** A silica glass sample after a trial melting test with 1 hour holding period at  $1800^{\circ}\text{C}$ . Left: a sample in a cracked alumina crucible. Right: a part of the sample consisting of molybdenum lining, cristobalite, and glass

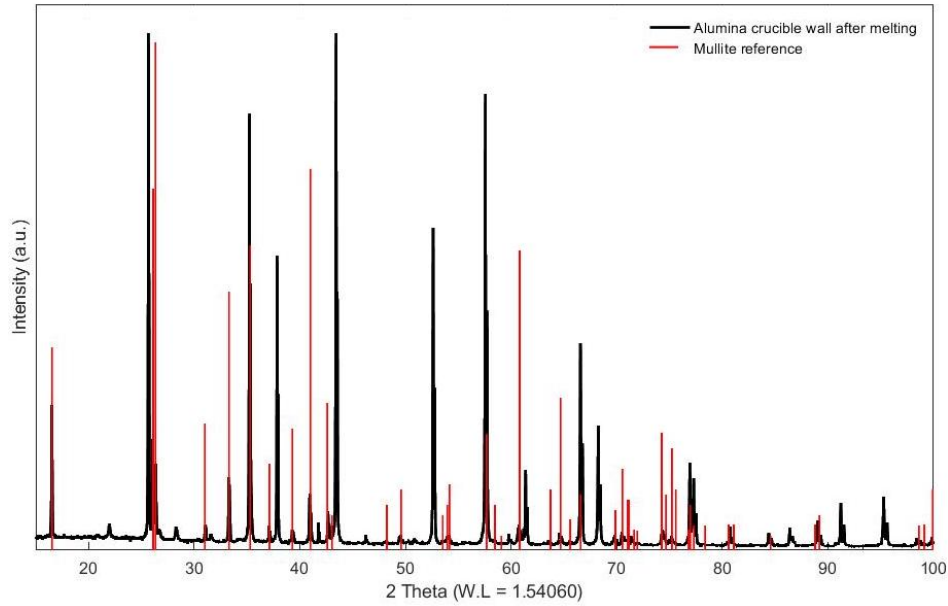


**Figure 4.2** XRD pattern of the melting crucible wall after the melting of quartz, with the mullite reference in red

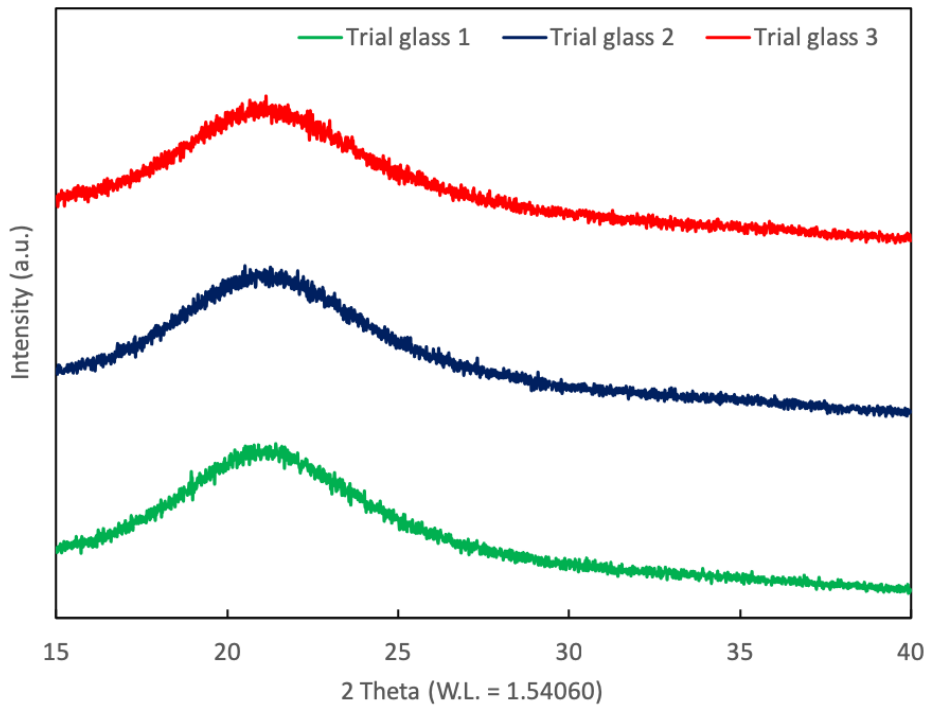


**Figure 4.3** XRD patterns of the top surfaces of 3 trial silica glasses (The quartz sand was heat treated at 600°C for 1 hour) in normalized intensity

After the melting method was finalized, 3 more trial melting tests were performed with the drying profile of

600°C for 1 hour. These extra melting tests were to ensure a high stability of the process. The appearances of these trial fused silica samples were similar as the one shown in Figure 4.7. The composition of the melting crucible wall after the melting was analyzed by XRD. The result is shown in Figure 4.2. The presence of mulite was observed from the result. These trial samples were used for validating tests for the setup and experimental parameters for viscosity and OH-content measurements. The surfaces of the 3 trial fused silica samples were taken to perform XRD. Figure 4.3 shows the XRD patterns of those 3 samples. There was not any trace of crystalline phase. The broad peaks correspond to the amorphous silica phase.

#### 4.1.2 Viscosity measurement

Several validating viscosity measurements were performed with commercial fused silica crucible provided by TQC. The method was the same as the one in Section 3.2.5, except the shorter holding period (15 minutes) at all the temperature steps. Figure 4.4 shows that no displacement was detected at 1400°C and 1450°C. A displacement curve, as shown in Figure 4.12, with negative creeps at all temperature steps is fundamental in order to calculate the viscosities. Afterwards, it was decided to increase the holding periods at 1400°C and 1450°C from 15 minutes to 1 hour, while those at 1500°C and 1550°C were the same.

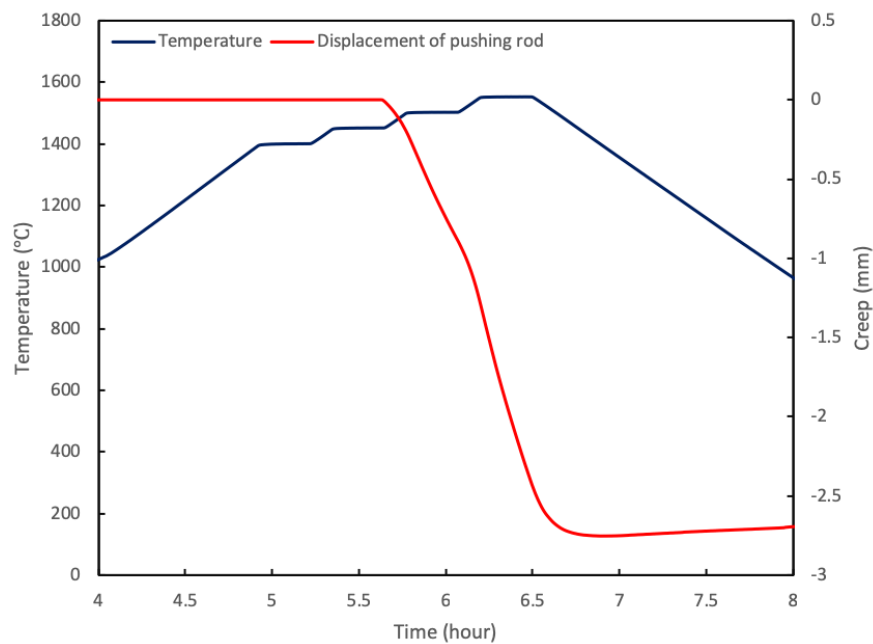


**Figure 4.4** Creep of a trial fused silica sample (dried at 600°C for 1 hour) at each temperature step over time

Another validating viscosity measurement with updated holding periods was performed with another trial fused silica sample (dried at 600°C for 1 hour). The method was the same as in Section 3.2.5. Figure 4.5 shows a barely indented surface with a thick, complete layer of cristobalite formed. It was then decided that the top layer (5 mm) of the sample should be removed for all samples, so that the viscosity and OH-content measurements were done at the vertical position of 5 mm below the original top surface.



**Figure 4.5** A trial fused silica sample with a thick, complete layer of cristobalite after a validating viscosity measurement. Left: indented surface. Right: cross-section

The measurement was performed again after the decision of removing the top surface layer was made, and an expected displacement curve (Figure 4.12) was obtained.

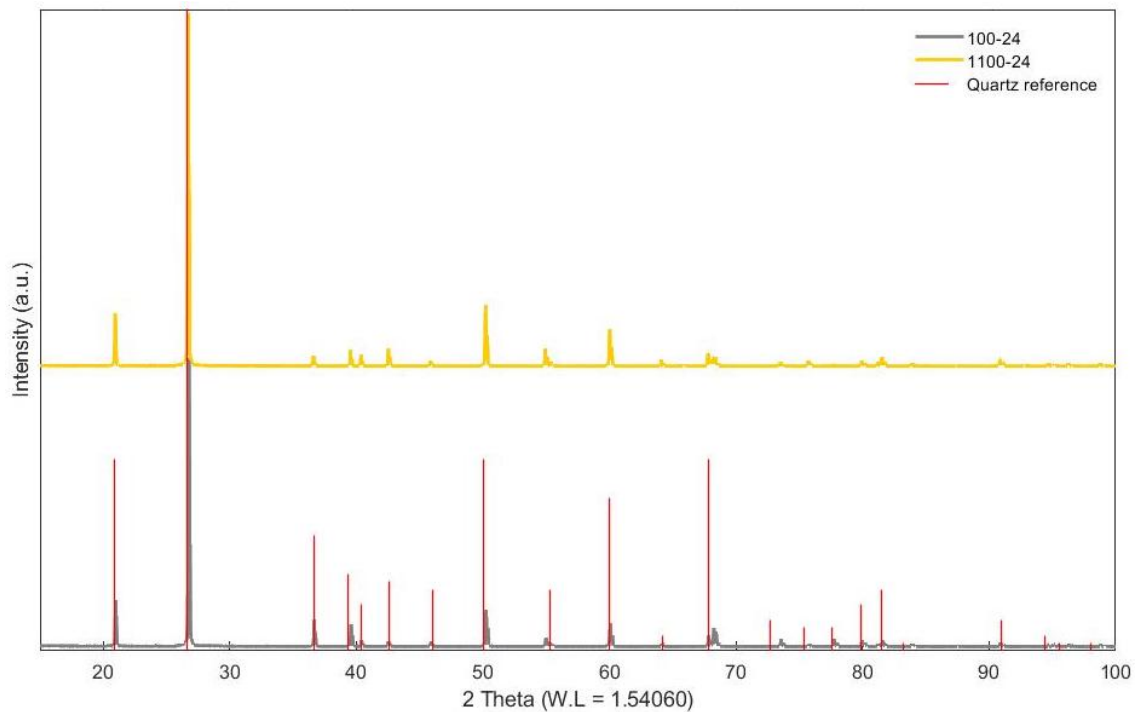
#### 4.2 Heat treatment

Heat treatment was also done separately during the production of fused silica. Two crucibles were placed in the furnace and heated in parallel with the same drying profile. The weight losses were calculated after the heat treatment of quartz sands. Table 4.1 shows the net weights of quartz sands before and after the heat treatment, as well as the calculated weight loss after the heat treatment. The moist content in the quartz sand was ca. 3.5 - 4%.



**Table 4.1** Weight loss of quartz sands after drying

Samples	Crucible	Net weight of sand before (g)	Net weight of sand after (g)	Weight loss (%)
100-24	#1	112.0	108.3	3.7
	#2	115.6	112.0	3.7
600-01	#1	102.3	99.1	3.2
	#2	113.5	109.9	3.6
900-01	#1	115.7	112.1	3.6
	#2	128.2	124.2	4.1
900-24	#1	113.7	110.0	3.7
	#2	122.0	118.1	3.9
1100-01	#1	115.9	111.9	4.0
	#2	126.3	122.0	4.3
1100-24	#1	109.4	105.6	3.8
	#2	124.8	120.7	4.1

**Figure 4.6** XRD patterns of two dried quartz sands (100-24 and 1100-24) in normalized intensity, with pure quartz reference in red

Quartz sands that were dried with two extreme profiles in the matrix (100-24 and 1100-24hr) were taken to perform XRD. Figure 4.6 shows the XRD patterns of both heat treated quartz sands. No additional peaks

that do not belong to the reference of quartz can be observed. It was ensured that no foreign material was picked up after the drying process.

### 4.3 Fused silica production

Figure 4.7 shows the general appearance of all the fused silica samples before cutting, except for 100-24. The production process for 100-24 was different from the others due to the separation of heat treatment and melting, as mentioned in Section 3.2.1.

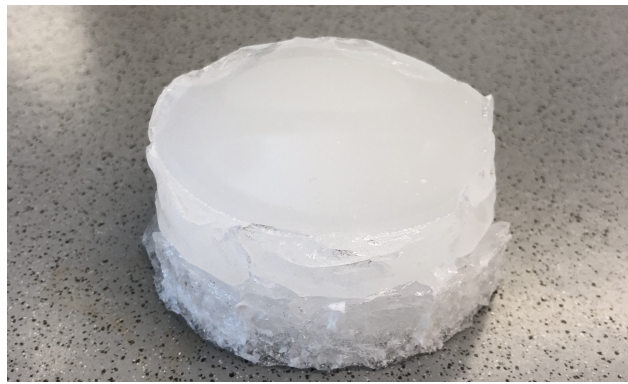


**Figure 4.7** The appearance of sample 600-01 before cutting

A much higher cooling rate from the melting temperature (1800°C) was expected due to the loss of power. Random milky white spots were observed on the top surface of resulting sample of 100-24. The results of all the experiments with 100-24hr were marked with \* before the sample name. All the results of 100-24 were not considered in the discussion and conclusion.

XRD was performed with all FTIR sample #1 (except 100-24) to confirm the absence of any crystalline phase. Their XRD spectra can be seen in Figure 4.8.

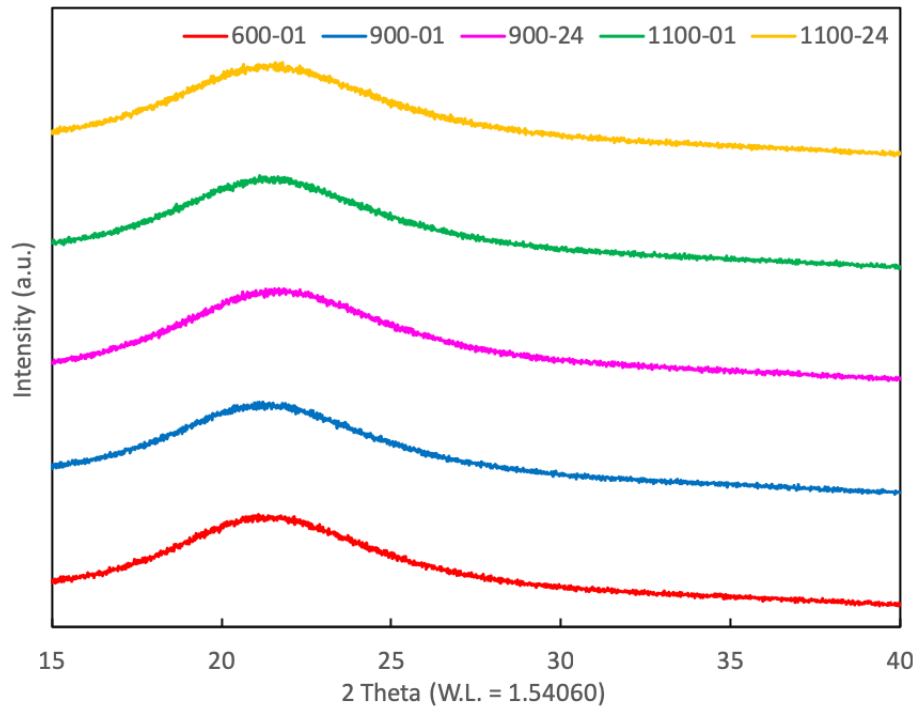


**Figure 4.8** XRD spectra of the surfaces of all FTIR sample #1 except 100-24

#### 4.4 OH-content

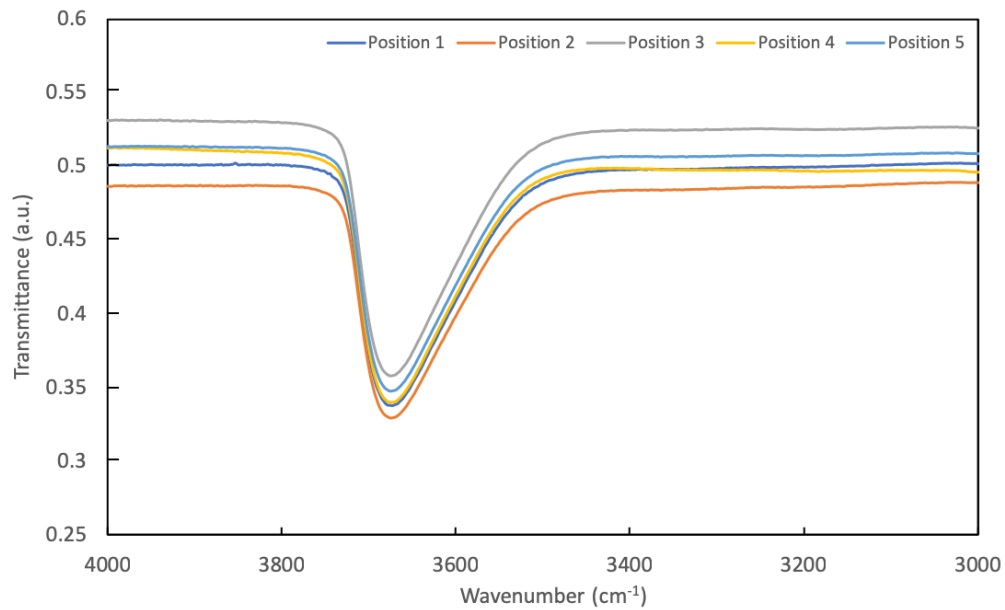


**Figure 4.9** The transmittance at different measured positions (shown in Figure 3.8) of sample 900-01(1)

The FTIR spectra of a fused silica sample (900-01(1)) are shown in Figure 4.9. The remaining spectra (with the same relative scale of transmittance) of other samples can be found in Appendix A.2. The spectrum clearly showed the peak at ca.  $3650\text{ cm}^{-1}$ , which represents the absorption band of bridged Si-OH species.

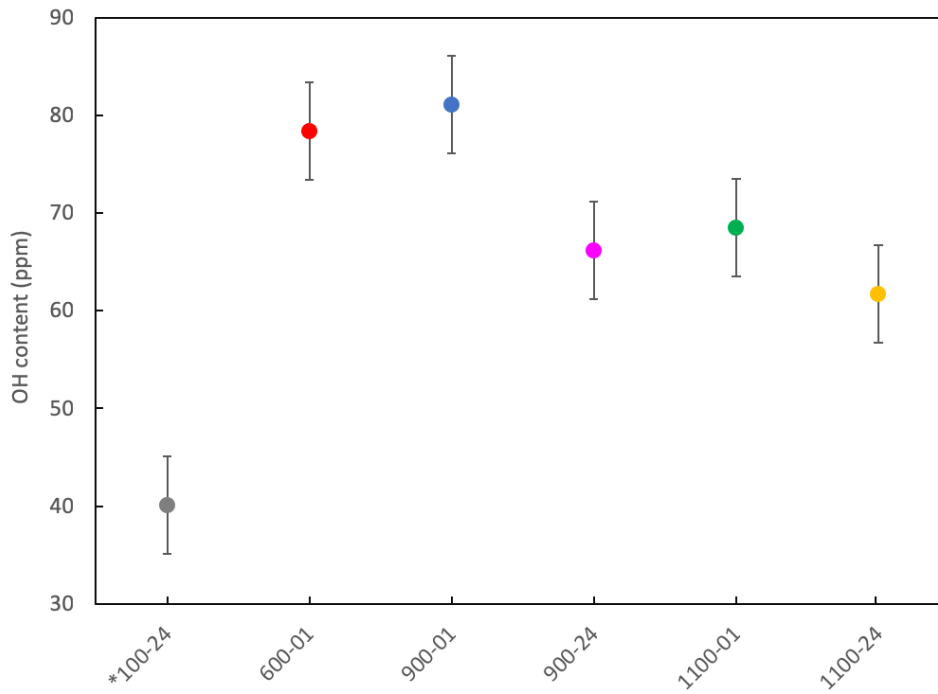
**Table 4.2** The OH-contents in all fused silica samples (Three parallels for each sample)

Samples	Average thickness (mm)	Average OH-content (ppm)	Error (ppm)	
<b>100°C 24hr</b>	#1	2.0	40	4.2
	#2	1.9	45	3.0
	#3	1.9	41	1.1
<b>600°C 1hr</b>	#1	2.2	78	4.2
	#2	2.0	77	9.2
	#3	2.3	62	6.1
<b>900°C 1hr</b>	#1	2.1	81	2.5
	#2	2.0	78	4.3
	#3	2.3	78	1.2
<b>900°C 24hr</b>	#1	2.0	66	11.2
	#2	2.1	63	3.9
	#3	2.2	58	5.3
<b>1100°C 1hr</b>	#1	2.3	69	7.6
	#2	2.4	49	5.6
	#3	2.6	53	8.8
<b>1100°C 24hr</b>	#1	1.9	62	2.1
	#2	1.8	57	3.2
	#3	2.0	56	2.4

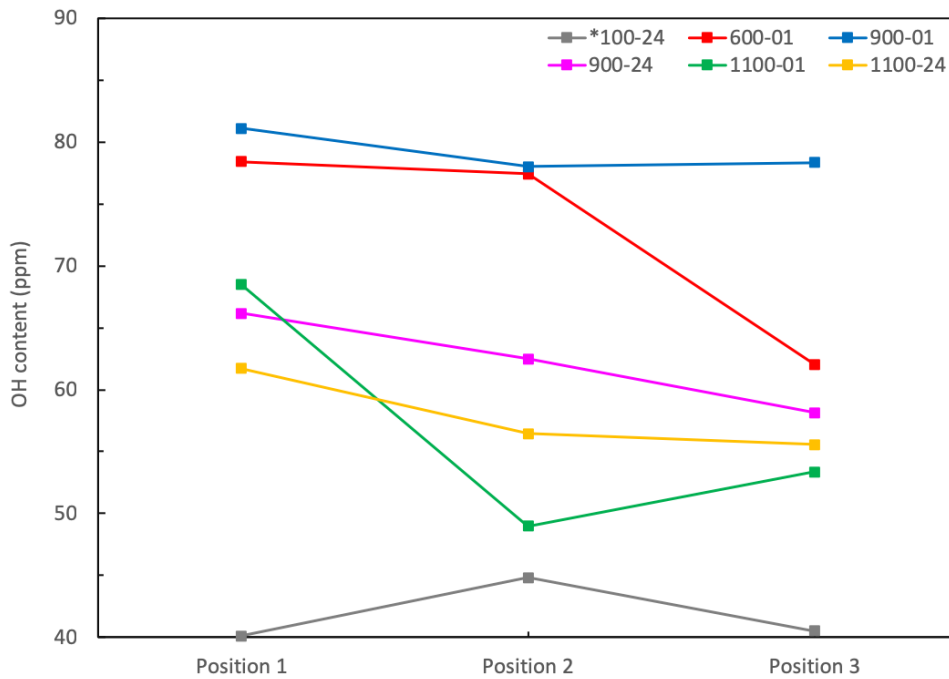
Table 4.2 summarizes the average OH-contents in all samples. The average thickness of each sample, which was one of the critical calculation parameters, was also shown in the same table. As mentioned in Section 3.2.4, sample 1 to 3 for OH-content measurement represented the vertical positions of the sample, where sample 1 represented the closest to the top surface.

Figure 4.10 shows the OH-contents in position 1 of all fused silica samples. It was decided to focus on the OH-contents at position 1 while relating it to viscosity because position 1 was at the same vertical position where the viscosity measurement was performed. It shows that 900-01 had the highest OH-content (81 ppm), while 1100-24 had the lowest OH-content (62 ppm). A decline of OH-content was also observed

among the samples with the same drying temperature.



**Figure 4.10** OH-contents in all FTIR samples #1 (shown in Figure 3.5). The viscosity measurement was performed at the same Z-position



**Figure 4.11** OH-contents in different vertical positions of all fused silica samples

The trends in the OH-contents in sample 1 to 3 of different fused silica samples are shown in Figure 4.11. The majority of the results exhibited a decreasing trend in OH-contents from sample 1 to 3 (top to bottom).

#### 4.5 Viscosity

There were minor differences in loadings for each viscosity measurement. The difference was considered in the calculation of the viscosities. The loadings for each measurement can be found in Appendix A.3.

Figure 4.12 shows the movement of the pushing rod at different temperature steps, with the sample 900-01(1). Higher indenting rate was observed with increasing temperature.

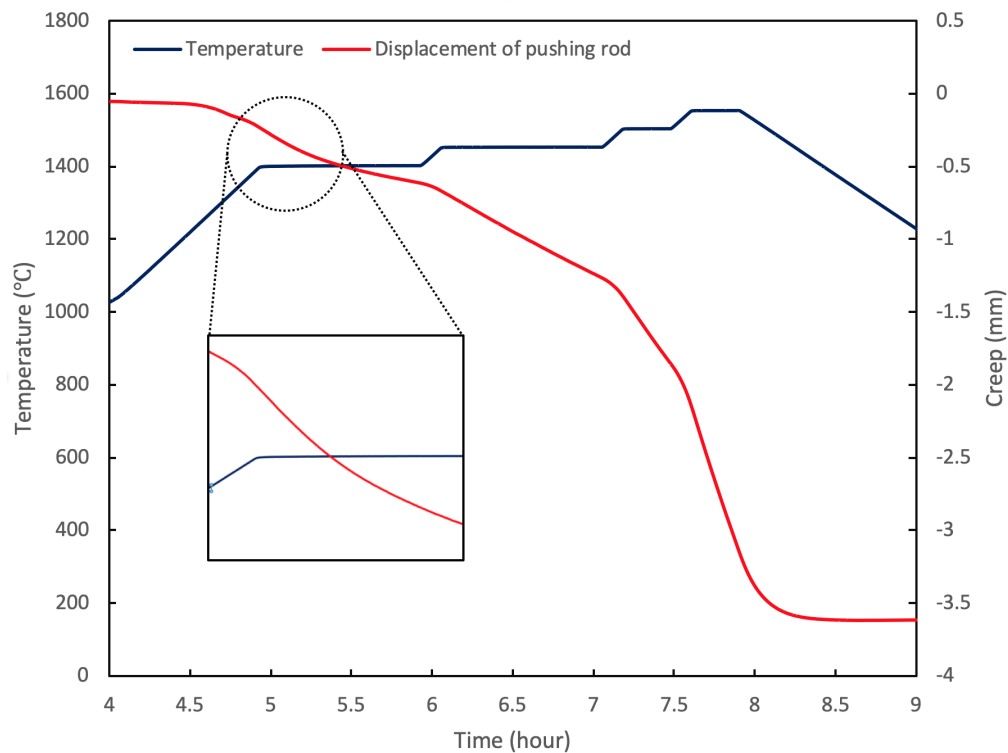


**Figure 4.12** The displacement behavior of 900-01(1) at each temperature step over time in hour, with a zoom-in illustration of the relaxation period at the beginning of 1400°C

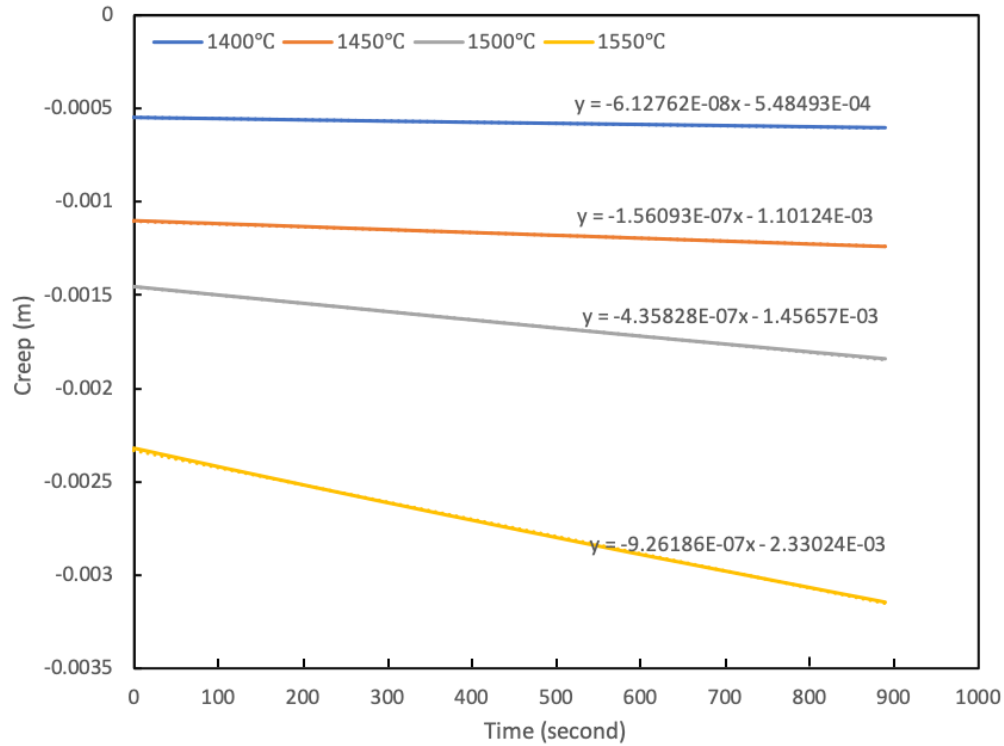


**Figure 4.13** The creep rates of 900-01(1) at all temperature steps

**Table 4.3** Viscosities (on log scale) of all fused silica samples at each temperature step (two parallels for each sample)

Sample	$\text{Log}_{10}$ (viscosity/Pa·s)				
	1400°C	1450°C	1500°C	1550°C	
*100-24	#1	9.6	9.3	8.9	8.5
	#2	9.7	9.3	8.8	8.5
600-01	#1	9.5	9.1	8.7	8.4
	#2	9.5	9.1	8.7	8.4
900-01	#1	9.6	9.2	8.8	8.4
	#2	9.7	9.2	8.8	8.5
900-24	#1	9.7	9.3	8.8	8.5
	#2	9.8	9.3	8.8	8.5
1100-01	#1	9.7	9.3	8.9	8.5
	#2	9.6	9.2	8.8	8.5
1100-24	#1	9.7	9.3	8.9	8.5
	#2	9.6	9.3	8.9	8.5

The creep rate at each temperature step was generated by using the data recorded during the last 1000

seconds (100 data in total) at each step, which can be seen in Figure 4.13. It was done to exclude the measured values in the relaxation period at the beginning of each temperature step. The creep rates (slopes), which can also be seen in the same figure, were used to calculate the viscosities. The calculation method can be seen in Section 3.2.5.

All the calculated viscosities (in log scale) at each step for all samples are presented in Table 4.3. On a log scale, the difference in viscosities among all the samples was relatively small.

The creep rates at different temperatures from which the viscosities were calculated, as well as the indented depth during the whole holding periods, are summarized in Table 4.4. More attention should be given to the creep rate at 1500°C, which is a common CZ pulling temperature used in the industry. The biggest difference in the creep rates at 1500°C was 0.74 mm/hr (600-01(1) and 1100-24(2)). Notable differences between 2 samples from the same type of glass were also observed. The loading forces for the indentation were slightly different but it was small enough (ca. 0.64% difference) to be neglected. A summary of the loading forces used for different samples can be seen in Table A.1.

**Table 4.4** Creep rates at different temperature steps and the indented depth from the beginning of 1400°C step to the end of 1550°C

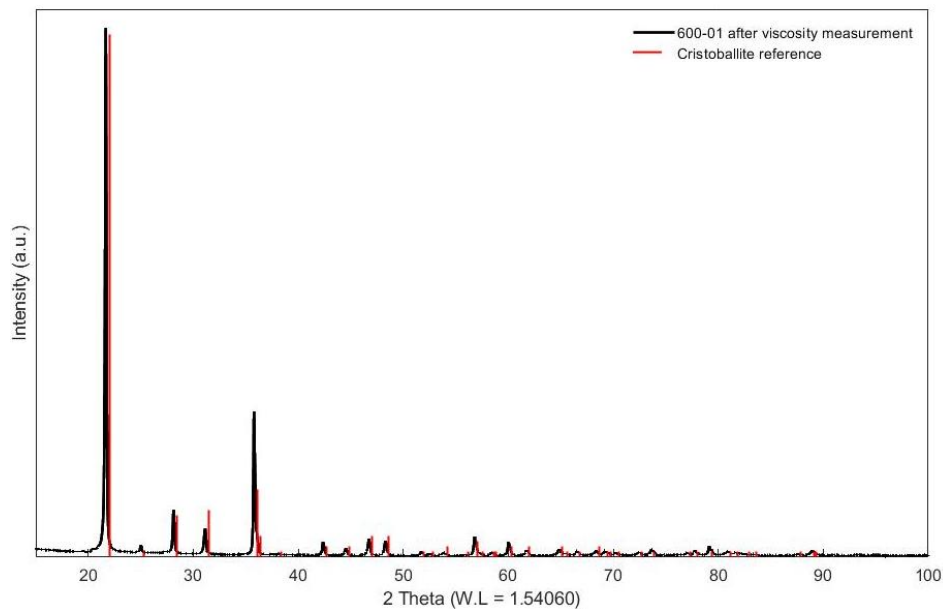
Sample	Creep rate (mm/hr.)				Total indented depth from 1400°C to 1550°C (mm)	
	1400°C	1450°C	1500°C	1550°C		
<b>*100-24</b>	#1	0.2	0.5	1.3	2.9	2.6
	#2	0.2	0.5	1.4	3.3	2.7
<b>600-01</b>	#1	0.3	0.8	1.9	3.6	3.5
	#2	0.3	0.8	1.9	3.9	3.6
<b>900-01</b>	#1	0.2	0.6	1.6	3.3	2.9
	#2	0.2	0.6	1.4	3.0	2.6
<b>900-24</b>	#1	0.2	0.4	1.4	3.1	2.6
	#2	0.2	0.5	1.4	3.0	2.5
<b>1100-01</b>	#1	0.2	0.5	1.3	2.7	2.4
	#2	0.2	0.5	1.5	3.2	2.8
<b>1100-24</b>	#1	0.2	0.5	1.2	2.8	2.4
	#2	0.2	0.5	1.3	2.9	2.5



**Table 4.5** Activation energies of viscosity for all the samples in different temperature ranges (kJ/mol)

Samples	Temperature range (°C)			
	1400 - 1450	1450 - 1500	1500 - 1550	
<b>*100-24</b>	#1	5.3	7.1	6.2
	#2	6.1	7.9	6.5
<b>600-01</b>	#1	6.3	7.0	5.2
	#2	6.2	6.6	5.4
<b>900-01</b>	#1	6.5	7.5	5.9
	#2	7.5	7.1	5.7
<b>900-24</b>	#1	6.0	8.1	6.4
	#2	7.6	7.8	6.1
<b>1100-01</b>	#1	6.6	7.2	5.8
	#2	6.2	7.6	5.8
<b>1100-24</b>	#1	7.0	6.5	6.6
	#2	5.3	7.2	6.6

The activation energies of viscosity in different temperature ranges for all samples was calculated by Equation 2.11, and presented in Table 4.5. Most of the samples had the highest activation energy of viscosity in the temperature range of 1450° to 1500°C.

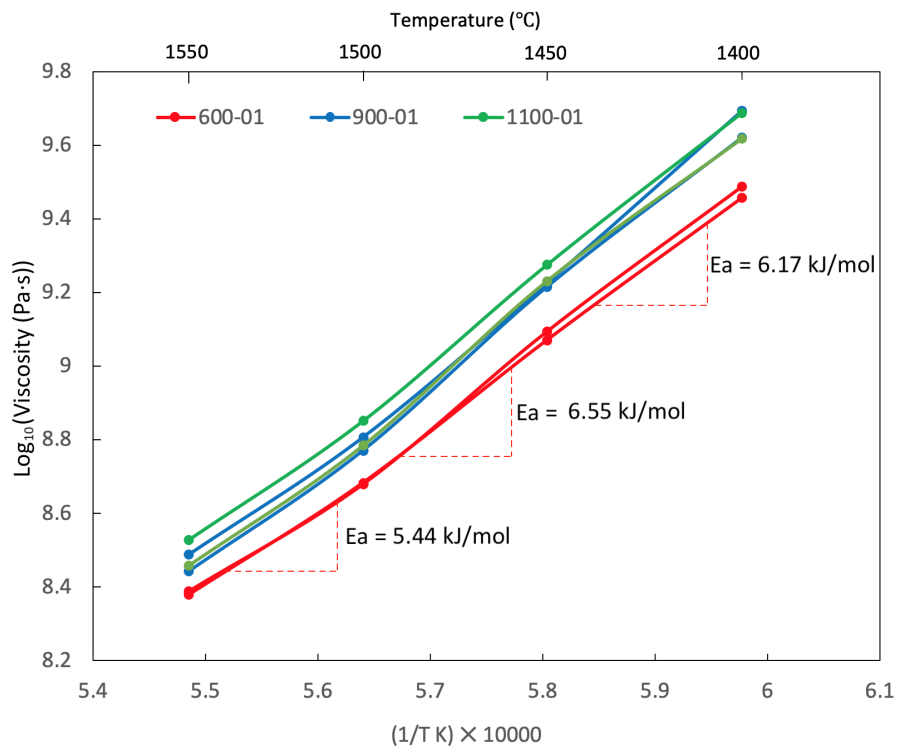
**Figure 4.14** The indented surface of 600-01(2) after viscosity measurement in normalized intensity, with cristobalite reference in red

Visually all the samples were covered by a milky white layer after the viscosity measurement. The composition of the indented layer of 600-01(2) was analyzed by XRD after the viscosity measurement. The result is shown in Figure 4.14, and it confirmed that the milky layer on the sample was cristobalite.

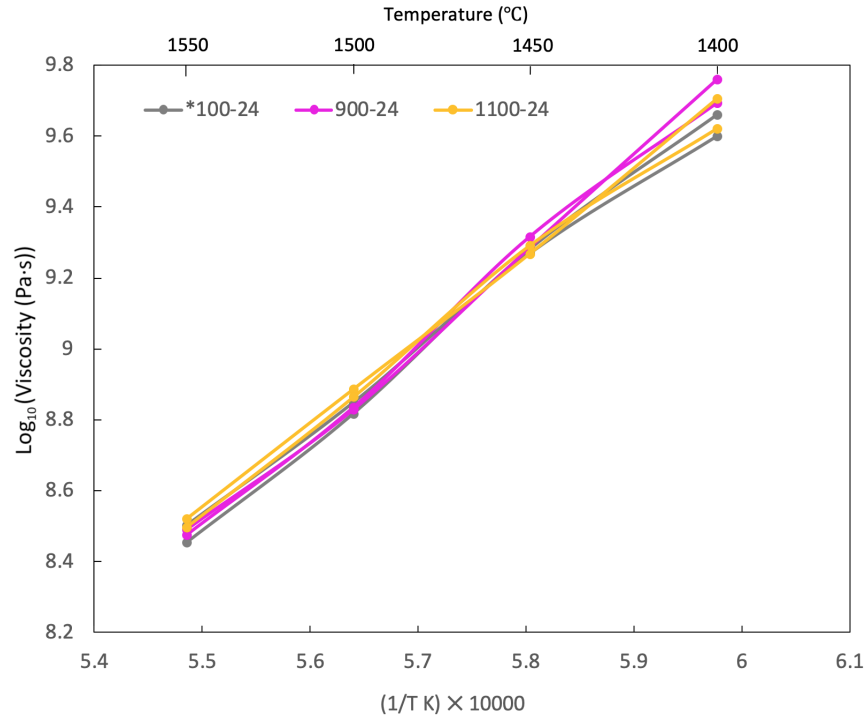
### Controlled drying period

Figure 4.15 and 4.16 show the viscosities of the samples that were dried at different temperatures for 1 and 24 hours respectively. An example of the calculation of the activation energy of viscosity was also included in Figure 4.15. The calculation was done by applying Equation 2.11. All the calculated activation energies can be found in Table 4.5. From the graph, the lower viscosity of 600-01 was clearly identified compared to that of the other samples. However, the viscosities of 900-01 and 1100-01 were very similar.

The viscosities of all the samples that were dried for 24 hours at different temperatures were also very close. A slight difference in the linearity of the viscosity curves was observed especially for 900-24. No serious conclusion should be made by considering sample 100-24 as its production process was different from the others, as mentioned in Section 4.3.



**Figure 4.15** Effects of different drying temperatures (for 1 hour) on viscosity, with the activation energies  $E_a$  of viscosity for 600-01(2)



**Figure 4.16** Effects of different drying temperatures (for 24 hour) on viscosity

**Controlled drying temperature**

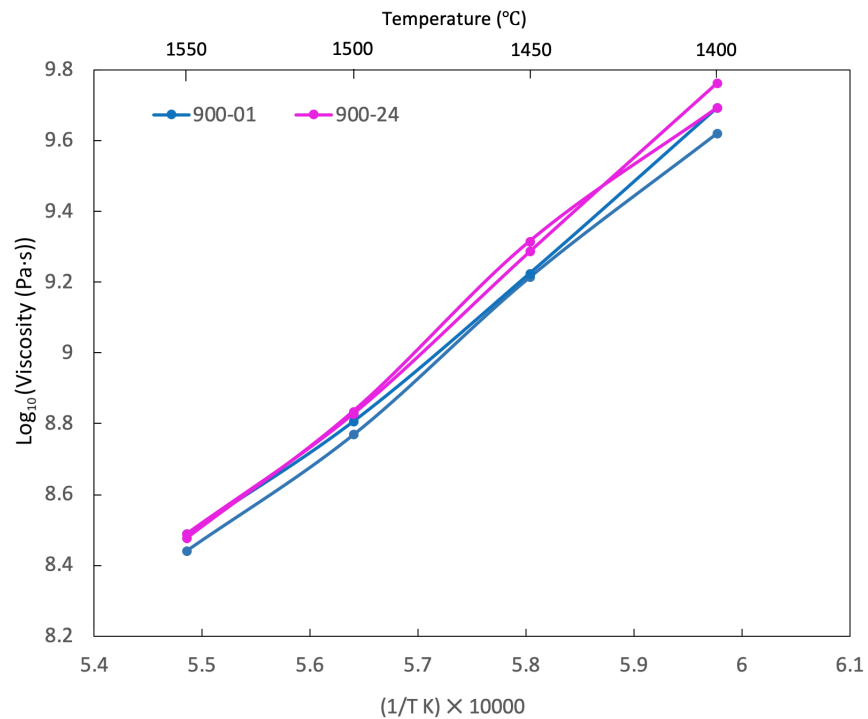


**Figure 4.17** Effects of drying time (at 900°C) on viscosity

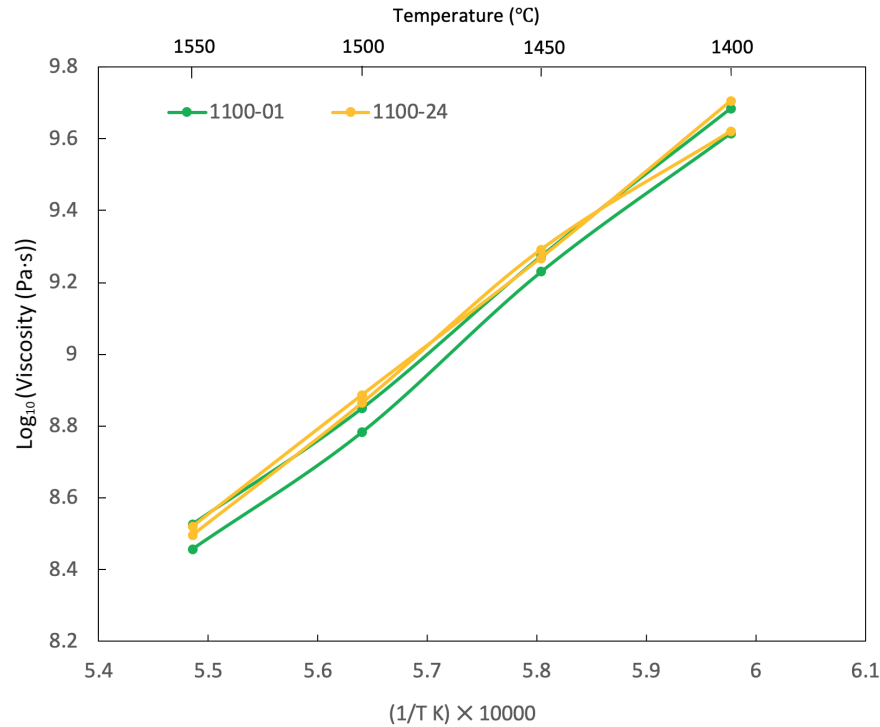


**Figure 4.18** Effects of drying time (at 1100°C) on viscosity

Figure 4.17 and 4.18 show the viscosities of the samples that were heat treated for different period of time at 900° and 1100°C respectively. In both cases, the viscosities of the samples that were heat treated for 1 hour were slight lower, compared to 24 hour. A variation of their linearities was also observed from both figures.

## 4.6 Bubble characterization

FTIR sample number 1 of 600-01, 900-01, and 1100-01 (shown in Figure 3.5) were selected to perform  $\mu$ -CT scanning for bubble characterization. In this section, the data processing was done by 3-dimensional analysis.

### 4.6.1 Bubble volume

The total measured bubble volumes and the samples' porosities are presented in Table 4.6. The porosity was obtained by dividing total pore volume by the analyzed sample volume. While 600-01 and 1100-01

#### 4. RESULTS

had similar total bubble volumes, the data shows a ca. 15% higher total bubble volume for 900-01. The porosities of all samples were found to be 2.4 - 2.8 vol%.

**Table 4.6** Total bubble volume and calculated porosity of samples that were heat treated for 1 hour

Sample	Analyzed sample volume (mm <sup>3</sup> )	Total bubble volume (mm <sup>3</sup> )	Total porosity (%)
600-01	411.1	9.9	2.4
900-01	411.1	11.5	2.8
1100-01	411.1	9.9	2.4

#### 4.6.2 Bubble distribution along Z-axis

The bubble distribution trend among sections from the top to bottom surface along Z-axis was studied and shown in Figure 4.19. The direction of the axis can be seen in Figure 3.8. The analyzed volume was separated into 6 sections, and the volume of each section was 15 x 15 x 0.3 mm<sup>3</sup>. The bubble volume was generally higher in the middle sections, while it showed little difference between the numbers of bubbles in each section for all the samples. It implies that the average sizes of bubbles in middle sections were greater.

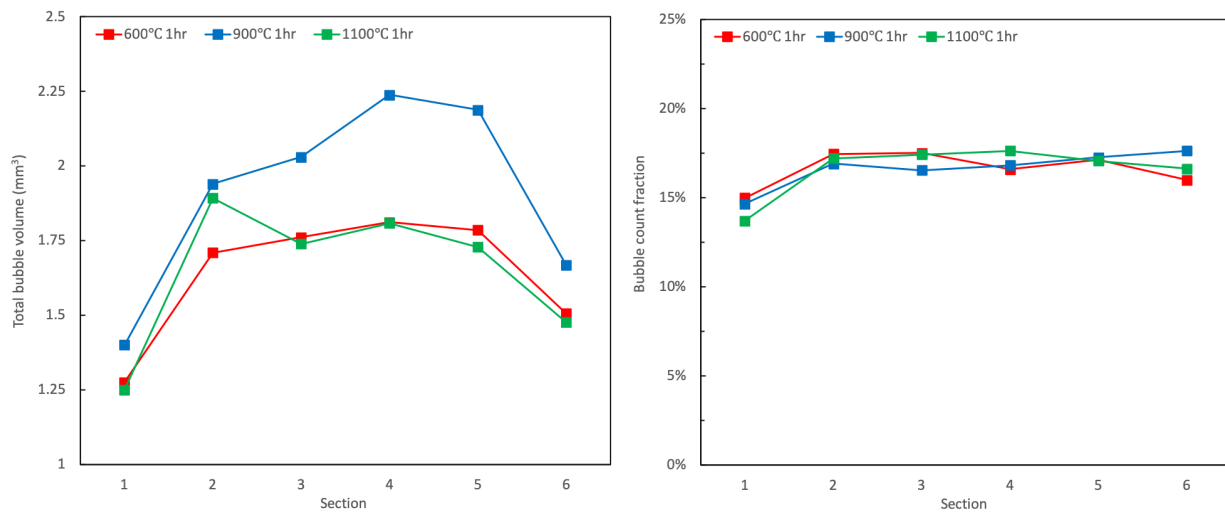


**Figure 4.19** Bubble volume and bubble amount distribution from the top to bottom surface, along Z-axis

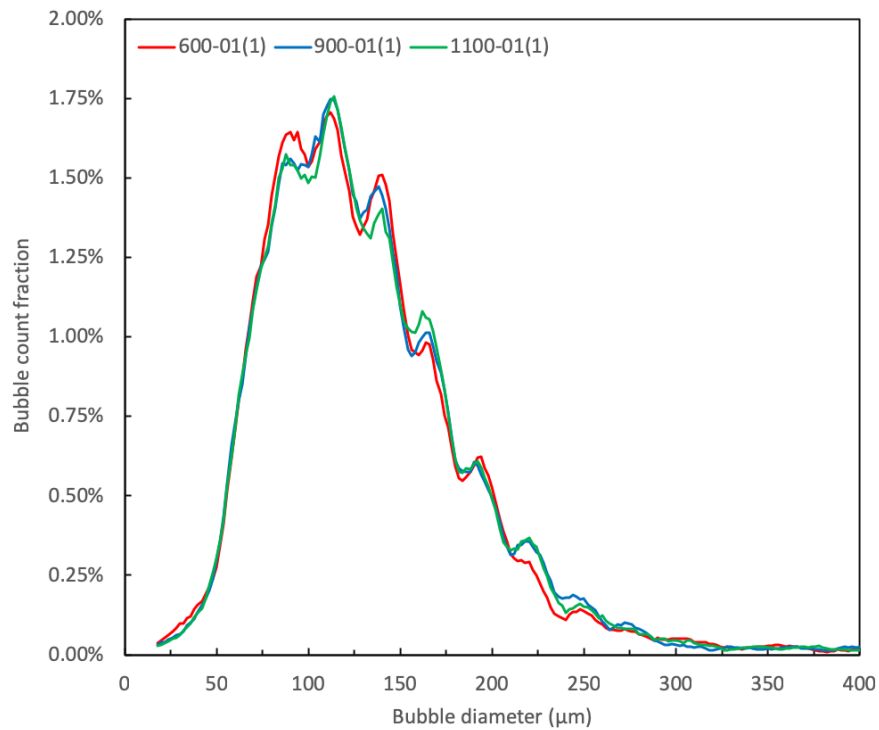
### 4.6.3 Number of bubbles

The total number of bubbles and the average bubble concentration are summarized in Table 4.7. It was noticed that both number of bubbles and the bubble concentration were similar. The total number of bubbles in 600-01 was 5.4% higher than that in 1100-01.

**Table 4.7** Bubble concentration in the analyzed volume

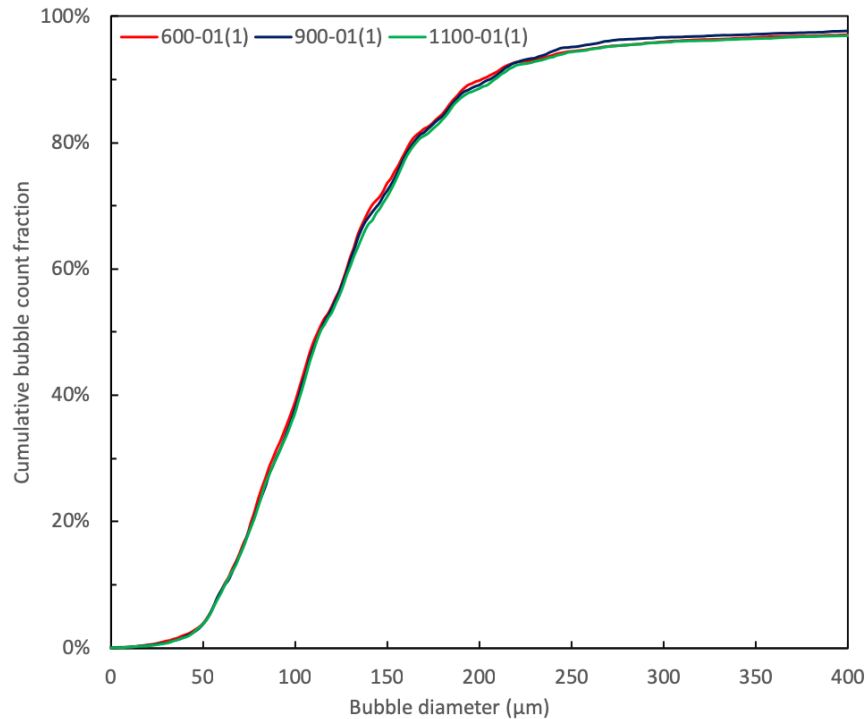
Sample	Analyzed sample volume (mm <sup>3</sup> )	Total number of bubbles	Average bubble concentration (#/mm <sup>3</sup> )
<b>600-01</b>	411.1	11469	28
<b>900-01</b>		11395	28
<b>1100-01</b>		10885	26

Figure 4.20 and 4.21 show the plot of bubble count fraction and cumulative bubble count fraction, respectively, against the bubble diameter. The curves in Figure 4.20 represented the average of 10 neighbor data.



**Figure 4.20** Bubble diameter distribution of the three examined fused silica samples

The bubble size distribution for all samples were very similar. For all the samples, the greatest amount (ca. 1.75%) of bubbles had the diameter of ca. 110  $\mu\text{m}$ . Ca. 93% of the bubbles had a diameter below 300  $\mu\text{m}$ , for all the samples. Ca. 4% of the bubbles had a diameter of over 2 mm, and they were considered as calculation error and neglected.



**Figure 4.21** Cumulative bubble diameter distribution of the three examined fused silica samples

#### 4.6.4 Local examination

A smaller volume ( $1.8 \times 1.8 \times 1.8 \text{ mm}^3$ ) at the centre of X-Y plane of all samples was examined. Their 3D morphologies are shown in Figure 4.22. This volume of 600-01, 900-01, and 1100-01 contained 139, 151, and 136 bubbles respectively.

The same volume at one of the corners of X-Y plane of all samples was also checked to understand the randomness of the bubble distribution. Their 3D images can be found in Appendix A.4. Table 4.8 lists out the number of bubbles and the total bubble volumes of different samples in different examined positions. From the existing data, 1100°C 1hr had the most consistent bubble distribution when its global porosity

was compared to results of different local examinations.

**Table 4.8** Properties of bubbles in a smaller analyzed volume ( $1.8 \times 1.8 \times 1.8 \text{ mm}^3$ ) at different positions on XY plane

Sample		No. of bubbles	Total bubble volume ( $\text{mm}^3$ )	Total porosity (%)
600-01	Centre	139	0.12	2.1
	Corner	159	0.12	2.1
900-01	Centre	151	0.15	2.6
	Corner	163	0.13	2.2
1100-01	Centre	136	0.13	2.3
	Corner	137	0.14	2.3

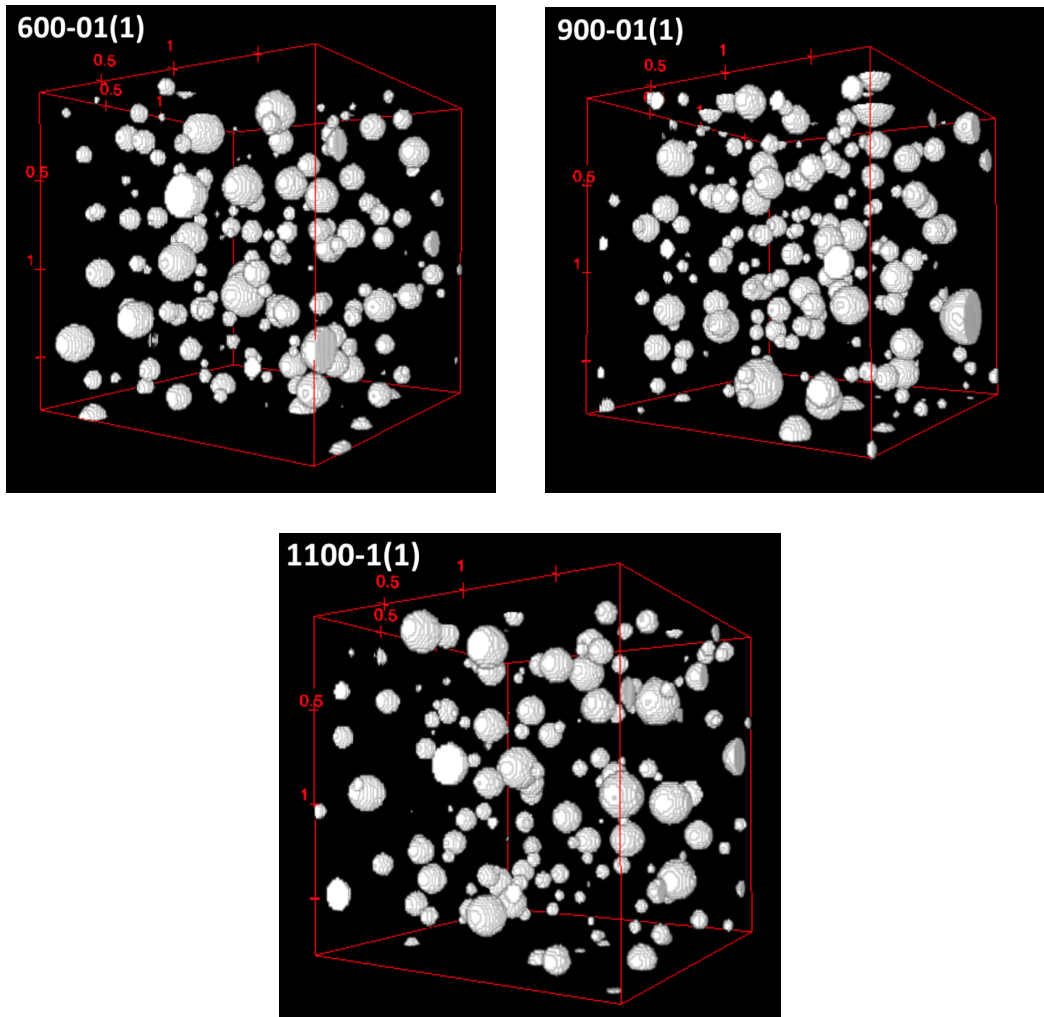


**Figure 4.22** 3D view of the entrapped bubbles in a volume of  $1.8 \times 1.8 \times 1.8 \text{ mm}^3$  at the centre of X-Y plane



## 5 Discussion

### 5.1 Validating experiments

A reliable experimental setup and process for fused silica production are needed to ensure the quality of the samples and the reliability of results. The design of melting crucibles and the heating profile were decided by considering the results of validating experiments.

#### 5.1.1 Development of experimental setup

A different crucible was used in the development stage. Molybdenum lining was firstly added inside the alumina crucible. It was observed that the molybdenum lining stuck onto the resulting silica glass wall, as shown in Figure 4.1, which was not easy to remove. Contamination could potentially happen by using either alumina and molybdenum as the crucible material. The reaction between alumina and silica could be observed visually after each melting. The melting crucible wall (without molybdenum) was taken to perform XRD to analyze the composition, the presence of mullite was observed from Figure 4.2. However, it was visually observed that the reacting zone was limited. It was then decided to perform the melting with alumina without molybdenum because it is a prevalent material for crucible at high temperature range and the potential reactions between silica and molybdenum was not well known. It was assumed that the diffusion of Al was minor as the diffusion rate of Al into the glass was probably slow, and the sides of the samples were also removed. There was also no trace of Al from the XRD results of different glass samples (Figure 4.8). The consideration of the effect of Al contamination was excluded from the discussion. The crucible shown in Figure 3.1 is not commercially available. The closed environment with windows on the top part of the wall prevented the silica from being contaminated by the refractory materials from the furnace compartment and allowed the water vapor from the sand to escape from the crucible. Pressed sands were used to ensure the same condition for the escape of water from the sand.

### 5.1.2 Development of melting procedure for fused silica

The intention of performing drying and melting of quartz sands in the same experiment and furnace was to minimize the variables and uncertainties. A trial melting test with only 1-hour holding time at the melting temperature was performed. Figure 4.1 shows a resulting trial glass sample in irregular shape and a thick layer of cristobalite. The furnace lost power in the middle of the melting stage during the production of sample 100-24. The furnace compartment was cooled without any control afterward. However, the appearance of sample 100-24 was very similar to the rest of the glass samples, with only minor white spots on the surface. It was assumed that the holding time at the melting stage has a much larger effect on glass formation compared to the cooling rate, as the required cooling rate for silica glass to form has a very high toleration, as mentioned in Section 2.2.2 [22]. Because the mechanical properties could be very different with such a high cooling rate, the results of 100-24 were not considered. The rest of the fused silica samples in this project also proved that 5-hour melting period gave a stable, promising outcome. It would be beneficial to perform more experiments to identify the shortest possible melting period that reduces the experimental time and energy usage.

## 5.2 OH-content in fused silica

The trend in OH-contents in the samples aligned with the hypothesis that either higher drying temperature or longer drying period lead to a lower OH-content. This is supported by the fact that a greater amount of water existing in the quartz sand was removed during the drying process. When the OH-contents in the samples that were dried at the same temperature with different periods (900-01 vs. 900-24 and 1100-01 vs. 1100-24) were compared, the samples dried for 24 hours had a lower OH-content. It is because the drastically longer drying period removed a greater amount of water in the sand. The OH-contents in 600-01 and 1100-01 also revealed that higher drying temperature results in a lower OH-content.

From Figure 4.10, 900-24, 1100-01, and 1100-24 had lower OH-contents compared to those of 600-01 and 900-01. There are two potential reasons for this observation. First, a higher amount of water was removed from the fluid inclusions of the quartz sands during the drying process for 900-24, 1100-01, and 1100-24. It can also be related to the humidity in the drying environment. As the whole production

process was done in an open furnace, the humidity in the furnace compartment was dependent on the humidity in the atmosphere on that specific day. It implies that the humidities during the production of each sample were different. However, more studies on the partial pressure of water in the atmosphere during each production are needed, in order to understand the effects on the OH-contents in different samples. Re-absorption of water by the quartz sand at the surface could be possible if the partial pressure of water in the atmosphere was higher. As mentioned in Section 2.3, silanol groups are the major sites for adsorption of water in silica. Ulvensøen [38] found that most of the isolated silanol groups were removed when the quartz sand was heated above 900°C. Less amount of water will be reabsorbed as there are less available silanol groups existing at the surface. The high OH-content observed from 900-01 can be explained by the inadequate drying period.

### 5.2.1 Trend in OH-contents along Z-axis of fused silica

The OH-contents at different Z positions of each fused silica sample were also measured and shown in Figure 4.11. A water concentration gradient was expected to be built up as the top surface was the only major interface for water to escape from the sand to the atmosphere. The majority of the results shows that the OH-contents decreased from the top, which is the opposite of the anticipation that the OH-content in the sample that was closest to the top should be the lowest. Only the top part of the samples (8 - 10 mm) were measured, while the bottom part (ca. 10 mm) of all fused silica samples were not used for any measurement. It is possible that the observed trends were just a local fluctuation. Measurement of OH-contents at the bottom part should also be performed before any conclusion is drawn. Another possibility is that the partial pressure of the vapor in the atmosphere was high enough to re-diffuse from the atmosphere to the sand close to the top interface, resulting in a higher OH-content.

According to the results from the previous project [25], the OH-contents in the BC layer of the used commercial crucibles decreased for as much as 90% of that in the new crucibles, while that in BF layer decreased for ca. 50%, which can be seen in Table A.2. It was explained by the diffusion of OH-groups to the entrapped bubbles. As the BC layer of the crucible is full of bubbles, the short distance from any position in the glass to the closest bubble is favorable for this event. This event would likely take place

during the production of our samples, as the period at high temperature range ( $>1000^{\circ}\text{C}$ ) after melting was around 8 hours, which was considerably long. The effect of this event depends on the amount of bubbles. Considering that the average porosity of our samples was over 5 times higher than that of the commercial crucible samples [44], the effect on OH-contents can be considerably high. Referring to the bubble distribution along Z-axis in Section 4.6.2, a variation of total bubble volume in different sections along Z-axis was observed. It can potentially explain the decreasing trends in OH-content from the top surface. The effect of the diffusion of OH-group to the bubbles depends on the availability of the bubbles and their volumes. However, the bubble characterization was performed only with FTIR sample 1. It can be possible that the bubble volumes in our samples increased globally from the top to the bottom, causing the reduced amount of present OH groups in the glass. A better evaluation on the effect of bubble distribution on the trend in OH-content can be done by performing the bubble characterization also with FTIR sample 2 and 3, or even with the whole fused silica sample.

### 5.2.2 OH-contents in commercial fused silica crucibles

The OH-contents in commercial fused silica crucibles made of the dried quartz sands from TQC were studied in the previous work of this project [25]. The summary of those results can be seen in Figure A.17. OH-contents in both bubble-composite- (BC) and bubble-free (BF) layer were measured. OH-contents in different HT samples were compared with the results in this project. Samples notations HT1 to HT4 represented the difference in the drying temperature. The drying temperature for the quartz sand was the lowest for HT1, while that was the highest for HT4. A decreasing trend in the OH-contents in HT1 to HT4 was observed. The OH-contents in BC layer varied from 18 to 38 ppm, while those in the BF layer ranged from 20 to 29 ppm. The OH-contents in the samples in this project ranged from 62 to 81 ppm. The average OH-content in our samples was almost double of that in the commercial crucibles. While their sample preparation and measurement methods were the same, the difference in the OH-contents can be related to the process of the drying as well as the fusion. Commercial crucibles are fused with very high power which may lower the OH-content. The commercial crucible samples were produced from quartz sands that were dried with a robust industrial process. It is expected that the moisture content in the sand can be removed in a more effective way, compared to the drying method used in this project.

### 5.3 Viscosity of fused silica

Considering the effect of drying parameters on viscosity directly, the fused silica sample that was dried at a higher temperature or longer period is expected to exhibit a higher viscosity. The difference in the viscosity that aligns with the hypothesis can be distinguished for most of the samples. However, the viscosities of the samples that were dried for 24 hours, were similar, which can be seen in Figure 4.16. The drying rate of the quartz sand will decrease as time increases. The drying temperature would be trivial to the water content removal if the drying period is very long.

#### 5.3.1 Activation energy of viscous flow

As mentioned in Section 2.5.2, the slope of the curve obtained by plotting the viscosity on the log scale against  $1/T$  is expected to remain unchanged [48]. However, variation of linearity was observed in Figure 4.15, 4.16, 4.17, and 4.18. The activation energies at the temperature ranges of  $1400^{\circ}\text{C} - 1450^{\circ}\text{C}$ ,  $1450^{\circ}\text{C} - 1500^{\circ}\text{C}$ , and  $1500^{\circ}\text{C} - 1550^{\circ}\text{C}$  for all the fused silica samples were calculated. An almost 100 times difference in the activation energy was observed when the values of our samples were compared to the values shown in Figure 2.7 [33]. The difference is still large when the difference in their measurement temperature range (ca.  $600^{\circ}\text{C}$  vs  $1500^{\circ}\text{C}$ ) is considered. The same equation (Equation 2.11) was also applied to calculate the activation energy of a commercial fused quartz with the viscosity data from Momentive<sup>TM</sup>, shown in Figure 2.11. The activation energy was found to be ca. 8.7 kJ/mol, assuming the viscosities at  $1400^{\circ}\text{C}$  and  $1600^{\circ}\text{C}$  are 10.5 and 8.5 log(P·s) respectively. This value is on the similar scale with the calculated activation energies of our samples. At this moment, we cannot draw any conclusions before any further study is conducted. The activation energy at the middle temperature range ( $1450^{\circ}\text{C} - 1500^{\circ}\text{C}$ ) was higher than that at the lower range ( $1400^{\circ}\text{C} - 1450^{\circ}\text{C}$ ) for most of the samples, followed by a decrease at the highest temperature range ( $1500^{\circ}\text{C} - 1550^{\circ}\text{C}$ ). It contradicts the expectation that the activation energy decreases linearly with increasing temperature, indicating that the system had changed in the temperature range of  $1400^{\circ}\text{C} - 1550^{\circ}\text{C}$ . The change in the activation energy can be an indicator of the behaviour of crystallization. The increases in activation energy from  $1400-1450^{\circ}\text{C}$  to  $1450-1500^{\circ}\text{C}$  among the samples were as much as 35%. From Figure 4.22 and A.15, there was not any observed major difference in the

bubble distribution from the 3D images, as well as the data. The observed trend in the activation energy changes was also similar for most of the samples. At this stage, it could be hypothesized that the bubble distribution did not have major contribution to the change of activation energy.

### 5.3.2 Comparison between commercial and lab-produced samples

The overall viscosity of the samples appeared to be low when it was compared to that of commercial fused silica. From Table 4.3, the viscosities of the samples varied from 8.68 to 8.89 log(Pa·s) at 1500°C, while the viscosity of commercial fused silica at the same temperature is ca. 9.5 log(Pa·s) (Provided by Momentive<sup>TM</sup>), shown in Figure 2.11. The viscosities of new commercial crucibles made of dried quartz sands from TQC were also measured with the same method in the previous work of this project. The summary of those results can be seen in Figure A.16. The range of the viscosities of the commercial crucibles were similar to those of the fused silica samples in this project [25]. No further conclusion should be drawn before the drying temperatures for the quartz sands for commercial crucibles are known.

The creep rates at different temperatures are summarized in Table 4.4. The creep rates for different samples were noticeably different. At 1500°C, it can be observed that the creep rate for 600-01 was almost 50% higher than that of 1100-24. With such a different creep rate at this temperature, a more obvious effect on the sagging situation of the quartz crucible during CZ process can be expected, considering the long holding period (typically ca. 24 hours) at a high temperature (ca. 1500°C) during the CZ process. However, these data cannot be directly translated to quantify the amount of sagging of the crucible during CZ process because of a totally different experimental condition. Instead, this set of data highlights the importance of the drying method for the quartz sand before fusion.

Two parallel viscosity measurements were performed for each type of samples to study the reproducibility of this novel setup. Very similar viscosity results were observed for most of the samples. Sample 1100-01 exhibited the biggest difference in viscosity from two parallel measurements. The difference was ca. 0.07 log(Pa·s) at every temperature step, while it was ca. 0.2 to 0.3 log(Pa·s) in average for the rest of the samples. When the viscosities at different temperatures were compared to the those of the commercial crucibles, which can be seen in Figure A.16, it was observed that the samples in this project showed better linearities

[25]. The existing measures for the sample preparation and the modification of the measurement process were able to produce results with good reproducibility.

### 5.4 Relationship between OH-content and viscosity of fused silica

OH-contents in FTIR samples #1 were considered to compare with their viscosities as FTIR sample #1 was at the same Z-position with that of the viscosity measurement sample. As discussed in Section 2.3, reduced viscosity is anticipated with higher OH-content. The majority of the results was in agreement with this statement. The hypothesis could be observed when the results of the samples with same drying temperature but different periods (900-01 vs. 900-24 and 1100-01 vs. 1100-24) were compared, shown in Figure 4.17 and 4.18. The results presented in Figure 4.15 partially supported the statement. The viscosities of 600-01 and 1100-01 reflected the difference in their OH-contents (78 and 69 ppm respectively).

The difference between the viscosities of some samples could not reflect the expected amount of difference in the corresponding OH-contents. From Figure 4.15, the viscosities of 900-01 and 1100-01 were very similar, while their OH-contents were comparatively different (81 and 69 ppm respectively). From the same figure, a considerably large variation in viscosity of 1100-01 can be observed. Within that range, it is still possible that the viscosity of 1100-01 was noticeably higher than that of 900-01, if only the highest curve of 1100-01 and the lowest curve of 900-01 were considered. From Figure 2.7, the average activation energy of viscous flow increased from ca. 110 kcal/mol (460 kJ/mol) to ca. 150 kcal/mol (628 kJ/mol) when the OH-content decreased from 763 to 110 ppm, which was a 653 ppm difference [33]. While the differences of the OH-contents among all the samples were only in the range of 62 - 81 ppm, the difference in their activation energies was expected to be minor. The results of the viscosities of some samples might not be able to show a distinct difference.

#### 5.4.1 Effect of cristobalite formation

Even though most of the results were in agreement with the inverse relationship between OH-content and viscosity, there were several contradicting observations. The results of the viscosity of 600-01 and 900-01 were not able to show the predicted relationship between OH-content and viscosity. While the OH-content

in 900-01 was slightly higher than that of 600-01, the viscosity of 900-01 was notably higher than that of 600-01, which can be seen in Figure 4.15. According to Section 2.3.1, the existing OH-groups in silica glass that cut the Si-O bonds increased the atom mobility, resulting in lower viscosity. At the same time, they facilitated the crystallization substantially. The formation of crystalline phase or nuclei of cristobalite will cause an increase in the calculated viscosity. From Figure 2.2,  $\beta$ -cristobalite has a much larger thermal expansion coefficient compared to that of silica glass [13]. With the presence of cristobalite, the measured displacement would be affected by the expansion of cristobalite. Therefore, it is possible that the effect of the cristobalite formed on the surface, interior, and possibly on bubbles' walls overshadowed the effect of increased atom mobility on the viscosity of the samples. However, the cristobalite formation condition of the samples should be well understood before its effect on the measurement can be quantified. Table 3.1 shows that the total concentration of Alkaline-earth elements (Mg and Ca) in quartz sand A was 0.5 - 0.6 ppm, which is considered to be low compared to the other impurities' concentrations [51]. It was assumed that the formation of cristobalite was not highly affected by the presence of Mg and Ca, as the formation of a complete layer of cristobalite requires a concentration of typically 100 ppm, as discussed in Section 2.2.3 [27]. At this stage, avoiding crystallization during the viscosity measurement would be the easiest and the most effective way to prevent the measurement results from being affected. It can be done by a control of atmosphere (removal of O<sub>2</sub> and H<sub>2</sub>O), as discussed in Section 2.2.3.

### 5.5 Possible effects of entrapped bubbles on viscosity

It is believed that bubbles in the samples weakened the mechanical strengths of the samples during viscosity measurement. It would result in a higher creep rate and, consequently, a lower viscosity. From Table 4.8, the porosities of the 3 samples at the centre on XY plane ranged from 2.1% to 2.6%. Paulsen *et al.* [44] found that the bubble volumes in the commercial fused silica crucibles increased for 70 - 90% after the heat treatment at 1400°C for 24 hours. Bubble expansion was expected during the viscosity measurement, considering the similar temperature range during the measurement (1400°C - 1550°C). Though there was not sufficient information to predict the degree of expansion due to the very different heating period compared to that in our viscosity measurement. In this case, the porosities of different samples could vary more after the expansion. The measured viscosities of different samples could be affected differently.



Performing bubble characterization with all samples can help understand more if there is a trend of bubble characteristics among different samples.

Incorporated OH groups in the fused silica samples can facilitate the crystallization. The presence of H<sub>2</sub>O and O<sub>2</sub> can catalyze crystallization, as discussed in Section 2.2.3 [24]. If these two substances existed in the entrapped bubbles, the walls of the bubbles could be the major sites for the formation of cristobalite in the interior. In this case, it is possible that the entrapped bubbles caused an increase in viscosity, as the cristobalite provided local mechanical support during the indentation. The expansion of cristobalite at high temperature range would be measured by the displacement sensor. Analyzing the gas composition in the bubbles would help predict the interior crystallization situation and evaluate the effect on the viscosity more accurately. XRD or microscopy can also be used to confirm if any crystalline phase was present in the interior of the samples after the viscosity measurement.

### 5.6 Bubbles of fused silica samples and commercial fused silica crucible

The properties of bubbles in the fused silica samples (600-01, 900-01, and 1100-01) are presented in Section 4.6. The porosities, bubble concentrations, and bubble size distributions of these samples were similar. It implies that different drying temperatures did not have a major contribution to bubble formation.

These results were compared with fused silica produced by different commercial quartz sands, studied by Guerra *et al.* [43], shown in Section 2.4.3. The results of sample QP.KY (an as-received imported high purity quartz sand) were considered due to its more similar impurities' concentrations with those in quartz sand A. The average bubble concentration in our samples was 26 - 28/mm<sup>3</sup>, while that in sample QP.KY was 0.38±0.15/mm<sup>3</sup>. The bubble concentration in our samples was 50 - 120 times higher than that in sample QP.KY. As the information about the raw material of QP.KY was not available, the properties of the raw materials of our samples and QP.KY were not known. For QP.KY, the production was done by Verneuil process (or flame fusion), while our samples were produced in an alumina crucible in an open furnace. Considering these differences, no conclusion should be drawn before knowing their most important glass production parameters including the atmosphere, temperature, and so on.

These results were also compared with different commercial crucibles, studied by Paulsen *et al.* [44]. The

average porosity of our samples was ca. 5 times higher than that of the as-received commercial samples, while the bubble concentrations (# per mm<sup>3</sup>) were 18 - 50% lower. The peaks of the bubble diameter of our samples and those of the commercial samples can be seen in Figure 2.12 and 4.20 respectively. The peaks of bubble diameter of our samples occurred at ca. 110 μm, while those of the commercial samples occurred at ca. 20 μm. The majority of the existing bubbles in the commercial samples was comparatively small. As the raw materials of our samples and the commercial crucibles were the same, the difference could be related to their manufacturing processes. As discussed in Section 2.4.1, during industrial-scale fused silica production, vacuum is applied from the outer surface of the mould where the fusion of silica is done. Most of the bubbles formed in the fused silica will migrate towards the outer surface, and be sucked out during the glass production process. Neither vacuum environment nor controlled atmosphere was available during the production of the samples in this project. It is expected that the absence of a vacuum environment, or a controlled atmosphere, during the glass production contributed to the observed difference in bubble distribution between the commercial and our samples. In case of the presence of carbon, the bubble formation during the silica melting can be related to the reduction of silica by existing carbon, described in Equation 5.1.



Analyzing the gas composition in the bubbles would help understand the mechanism of bubble formation during the melting, which is fundamental for minimizing the total volume of bubbles in the silica glass.

The main impurities in the commercial fused silica crucible and our fused silica samples could also be different. Carbon is expected to be present in the commercial crucible as the production of the crucible is commonly done in a graphite crucible, while our fused silica samples were produced in alumina crucible. The bubble formation during the production can be affected by different impurities.

## 6 Conclusion

A process involving both drying and melting of high purity quartz sand was established. Consistent fused silica samples were successfully produced after optimizing the heating profile and the selection of melting crucible materials and shapes by validating experiments. The process of viscosity measurement was further optimized after considering the observations from the previous works of this project, resulting in a better reproducibility. Results from XRD showed that the fused silica samples were free from crystalline phase.

A sample set consisting of six different fused silica samples were produced based on different combinations of drying temperatures and periods. Several conclusions were drawn from the observations:

- The majority of the results exhibits the inverse relationship between OH-content and viscosity of fused silica
- Effect of drying temperatures on OH-contents is more obvious with 1-hour drying period compared to 24-hour
- Optimal drying parameters have a major contribution to the mechanical performance of the crucible during the CZ process

There were some uncertainties that could influence the results. There was limited control on the amount and volume of bubbles in the samples, which could affect the results of both OH-content and viscosity. The bubble distributions in the 3 samples (600-01, 900-01, and 1100-01) were found to be random.

## 7 Further work

Due to the limited amount of samples, the samples at different horizontal position were used for viscosity and OH-contents measurement. The results of viscosity and OH-content would be more reliable if the variation of the measuring positions (relative distance to the crucible wall) can be kept minimum. The melting process and equipment should further be optimized in order to minimize the existing uncertainties. Controlled atmosphere during melting and viscosity measurement will help reduce the uncertainties and, consequently, more promising results.

Composition analysis of the samples should be done at each stage to have a better understanding on the possible events during each process, especially after reheating of fused silica (viscosity measurement). Analysis of both exterior and interior of the samples will provide more information about the cristobalite formation behavior during viscosity measurement. It will also be beneficial to measure the OH-contents in the samples after the viscosity measurement. The fused silica sample produced by the developed process should be further examined due to the observation of severe cristobalite formation on the top surface after re-heating, which can be seen in Figure 4.5. As XRD could not detect any crystalline phase on the top surface of the fused silica sample, use of Raman spectroscopy can be considered.

Same characterization can be performed with the fused silica samples with the same thermal treatment of quartz sand but different melting technique. The contribution of the melting procedure to the measurement result can be evaluated by comparing with the results of this project.

## References

- [1] National Academy of Engineering. "Make solar energy economical". URL: <http://www.engineeringchallenges.org/challenges/solar.aspx> (visited on 02/01/2019).
- [2] Wafer World Inc. "The Czochralski Process". URL: <http://www.top-alternative-energy-sources.com/Czochralski-process.html> (visited on 01/18/2019).
- [3] K.M. Davis and M. Tomozawa. "Water diffusion into silica glass: Structural changes in silica glass and their effect on water solubility and diffusivity". *Journal of Non-Crystalline Solids* 185.3 (1995), pp. 203–220.
- [4] W Holand and G. Bell. "Glass-ceramic technology" (2002).
- [5] A. F. Holleman and Egon Wyberg. *Brewer, William, San Diego/Berlin: Academic Press/De Gruyter* (2001).
- [6] "The Quartz Page. Overview of silica polymorphs". URL: [http://www.quartzpage.de/gen\\$\\\_\\$mod.html](http://www.quartzpage.de/gen$\_$mod.html) (visited on 01/10/2019).
- [7] David C. Palmer. "Chapter 3. STUFFED DERIVATIVES OF THE SILICA POLYMORPHS: Physical Behavior, Geochemistry, and Materials Applications". Dec. 1994, pp. 83–122.
- [8] Tapan K. Gupta and Jau-Ho Jean. "Origin of cristobalite formation during sintering of a binary mixture of borosilicate glass and high silica glass". *Journal of Materials Research* 9.4 (1994), 999–1005.
- [9] Sandford S. Cole. "The Conversion of Quartz into Cristobalite Below 1000°C, and Some Properties of the Cristobalite Formed\*". *Journal of the American Ceramic Society* 18.1-12 (1935), pp. 149–154.
- [10] Irena Markovska. "Structure, Thermodynamic Properties, Solubility and Synthesis of the Different Modifications of Silica". Jan. 2011, 95 – 143.
- [11] Lucia Pagliari, Monica Dapiaggi, Alessandro Pavese, and Fernando Francesco. "A kinetic study of the quartz–cristobalite phase transition". *Journal of the European Ceramic Society* 33.15 (2013), pp. 3403–3410.

- [12] Y. Fei. "Thermal expansion". *Ahrens TJ, editor. Mineral physics and crystallography: a handbook of physical constants 2* (1995), pp. 29–44.
- [13] Pamela O'Connor.
- [14] Carol S. Mariani and Linn W. Hobbs. "Network properties of crystalline polymorphs of silica". *Journal of Non-Crystalline Solids* 124.2 (1990), pp. 242–253.
- [15] A C.D. CHAKLADER and A L. ROBERTS. "Transformation of Quartz to Cristobalite". *Journal of the American Ceramic Society* 44 (June 2006), pp. 35–41.
- [16] M.E. Kjelstadli. "Kinetics and mechanism of phase transformation from quartz to cristobalite". *Master's thesis, NTNU* (2015).
- [17] S. Mitra. *Trans J. Brit. Ceram. Soc.* 65 (1977), pp. 71–74.
- [18] Kjell Wiik. "Kinetics of Reactions Between Silica and Carbon". *PhD thesis, NTNU* (1990).
- [19] "Quartz vs. Fused Silica: What's the Difference?" (Sept. 2015). URL: <https://www.swiftglass.com/blog/quartz-vs-fused-silica-whats-the-difference/> (visited on 03/23/2019).
- [20] W. David Kingery. "Introduction to Ceramic" (1975).
- [21] Katharina Vollmayr, Walter Kob, and Kurt Binder. "How do the properties of a glass depend on the cooling rate? A computer simulation study of a Lennard-Jones system". *The Journal of Chemical Physics* 105.11 (1996), pp. 4714–4728.
- [22] S.W. Martin. "Fundamentals of the glass transition: The glass transition is a kinetic transition with thermodynamic signatures". *Lehigh University*.
- [23] S. Malo, O. Pérez, and M. Hervieu. "Spherulite-shaped cristobalite by fused silica devitrification". *Journal of Crystal Growth* 324.1 (2011), pp. 268–273.
- [24] Tosoh Corporation. "Fused Silica Glass". URL: <http://www.gmassoc.com/pdf/Tosoh\%20SGM\%20-\%20Fused\%20Silica\%20Glass.pdf> (visited on 04/02/2019).
- [25] T.C. Cheung. "Next generation of quartz crucible for production of Czochralski solar cell". *Specialization project, IMA, NTNU* (Dec. 2018).

- [26] N.G. Ainslie, C.R. Morelock, and D Turnbull. “Devitrification kinetics of fused silica”. *Symposium on Nucleation and Crystallization in Glasses and Melts* (Jan. 1962), pp. 97–107.
- [27] Xinming Huang, Takeshi Hoshikawa, and Satoshi Uda. “Analysis of the reaction at the interface between Si melt and Ba-doped silica glass”. *Journal of Crystal Growth* 306 (Aug. 2007), 422–427.
- [28] Keiji Yamahara, Xinming Huang, Susumu Sakai, Akira Utsunomiya, Yasushi Tsurita, and Keigo Hoshikawa. “Surface of Silica Glass Reacting with Silicon Melt: Effect of Raw Materials for Silica Crucibles”. *Japanese Journal of Applied Physics* 40 (Feb. 2001), p. 1178.
- [29] Nina G Stenina. “Water-related defects in quartz”. *Bulletin of Geosciences* 79 (Jan. 2004).
- [30] D. T. Griggs and J. D. Blacic. “Quartz: Anomalous Weakness of Synthetic Crystals”. *Science* 147.3655 (1965), pp. 292–295.
- [31] V.G. Plotnichenko, V.O. Sokolov, and E.M. Dianov. “Hydroxyl groups in high-purity silica glass”. *Journal of Non-Crystalline Solids* 261.1 (2000), pp. 186–194.
- [32] S. Fujita, A. Sakamoto, and M. Tomozawa. “Behavior of water in glass during crystallization”. *Journal of Non-Crystalline Solids* 320.1 (2003), pp. 56–63. URL: <http://www.sciencedirect.com/science/article/pii/S0022309303000772>.
- [33] P.W. McMillan and Chlebik A. “The effect of hydroxyl ion content on the mechanical and other properties of soda-lime-silica glass”. *Journal of Non-Crystalline Solids* 38-39 (1980). XIIth International Congress on Glass, pp. 509–514.
- [34] Sumio Sakka, Kazumasa Matsuita, Tsutomu Watanabe, and Kanichi Kamiya. “Effects of Small Amounts of Water on the Viscosity, Glass Transition Temperature and Vickers Hardness of Silicate Glasses”. *Journal of the Ceramic Association, Japan* 89.1034 (1981), pp. 577–584.
- [35] Yongheng Zhou and Zhenan Gu. “The study of removing hydroxyl from silica glass”. *Journal of Non-Crystalline Solids* 352.38 (2006), pp. 4030–4033.
- [36] Merve Yesilbas and Jean-François Boily. “Particle Size Controls on Water Adsorption and Condensation Regimes at Mineral Surfaces”. *Scientific Reports* 6 (Aug. 2016), p. 32136.
- [37] Michelle L Gee, Thomas W Healy, and Lee R White. “Hydrophobicity effects in the condensation of water films on quartz”. *Journal of Colloid and Interface Science* 140.2 (1990), pp. 450–465.

- [38] Anna Ulvensøen. “Interaction of water with quartz sand surfaces studied by diffuse reflectance IR spectroscopy”. *Specialization project, IMA, NTNU* (Dec. 2018).
- [39] Katsuhiko Kemmochi and Yasuo Ohama. “Method for making a silica glass crucible” (2008). European Patent, EP2022765A1.
- [40] “Picture of a quartz glass crucible”. URL: <http://www.ferrotec.co.jp/images/english/products/pv/crucible.jpg> (visited on 01/02/2019).
- [41] Vladimir Fokin, Alexander Karamanov, Alexander Abyzov, Jörn Schmelzer, and Edgar Zanotto. “Stress-induced Pore Formation and Phase Selection in a Crystallizing Stretched Glass”. *BOOK chapter "Glass - Selected Properties and Crystallization" pp. 471-479, De Gruiter, Ed. J. W. Schmelzer* (Jan. 2014).
- [42] John A. Bones. “Conversation with SINTEF Industri, Sustainable Energy Technology Senior Research Scientist Senior Project Manager” (2018).
- [43] Christiano Guerra, Eduardo Ono, Murilo Santos, and Carlos Kenichi Suzuki. “Study of Bubbles Elimination in Silica Glass Produced by Flame Fusion from Brazilian Natural Quartz Powder”. *Materials Science Forum* 798-799 (June 2014), pp. 375–380.
- [44] Ove Paulsen, Stein Rørvik, Astrid M.F. Muggerud, and Mari Juel. “Bubble distribution in fused quartz crucibles studied by micro X-Ray computational tomography. Comparing 2D and 3D analysis”. *Journal of Crystal Growth* 520 (2019), pp. 96–104.
- [45] LibreTexts-Chemistry. “How an FTIR Spectrometer Operates” (2019). URL: [https://chem.libretexts.org/Bookshelves/Physical\\_and\\_Theoretical\\_Chemistry\\_Textbook\\_Maps/Supplemental\\_Modules\\_\(Physical\\_and\\_Theoretical\\_Chemistry\)/Spectroscopy/Vibrational\\_Spectroscopy/Infrared\\_Spectroscopy/How\\_an\\_FTIR\\_Spectrometer\\_Operates](https://chem.libretexts.org/Bookshelves/Physical_and_Theoretical_Chemistry_Textbook_Maps/Supplemental_Modules_(Physical_and_Theoretical_Chemistry)/Spectroscopy/Vibrational_Spectroscopy/Infrared_Spectroscopy/How_an_FTIR_Spectrometer_Operates) (visited on 11/01/2018).
- [46] Bert Sloots. “Measuring the low OH content in quartz glass”. *Vibrational Spectroscopy* 48.1 (2008). PAPERS PRESENTED AT THE 4TH INTERNATIONAL CONFERENCE ON ADVANCED VIBRATIONAL SPECTROSCOPY, CORFU, GREECE, 10-15 JUNE 2007 - PART I, pp. 158–161.



- [47] M. Sakai and S. Shimizu. "Indentation rheometry for glass-forming materials". *Journal of Non-Crystalline Solids* 282.2 (2001), pp. 236 –247.
- [48] Ove Paulsen. "Memo - Viscosity measurement of fused silica glass, SINTEF Industri" (2018).
- [49] Malcolm M. Haring. "The Theory of Rate Processes (Glasstone, Samuel; Laidler, Keith J.; Eyring, Henry)". *Journal of Chemical Education* 19.5 (1942), p. 249.
- [50] Michael Ojovan. "About activation energy of viscous flow of glasses and melts". *MRS Proceedings* 1757 (Jan. 2015).
- [51] The Quartz Corp. "NC4A, High Purity Quartz Sand" (2015).
- [52] M Doube, MM Kłosowski, I Arganda-Carreras, F Cordelières, RP Dougherty, J Jackson, B Schmid, JR Hutchinson, and SJ Shefelbine. "BoneJ: free and extensible bone image analysis in ImageJ" (2010).

## A Appendices

### A.1 Matlab script for OH content calculation

```
data = load('DataFromFTIR.dpt');  
y = data(1:length(data),2); x=data(1:length(data),1);  
[ycorrect,baseline] = bf(y,5,'confirm'); d = thickness(data);  
Tmin = min(1-abs(ycorrect)); beta=(1/d)*log(1/Tmin);  
factor = (17*10000)/(77.5*2.21); OHppm=factor*beta;
```

### A.2 FTIR Spectra

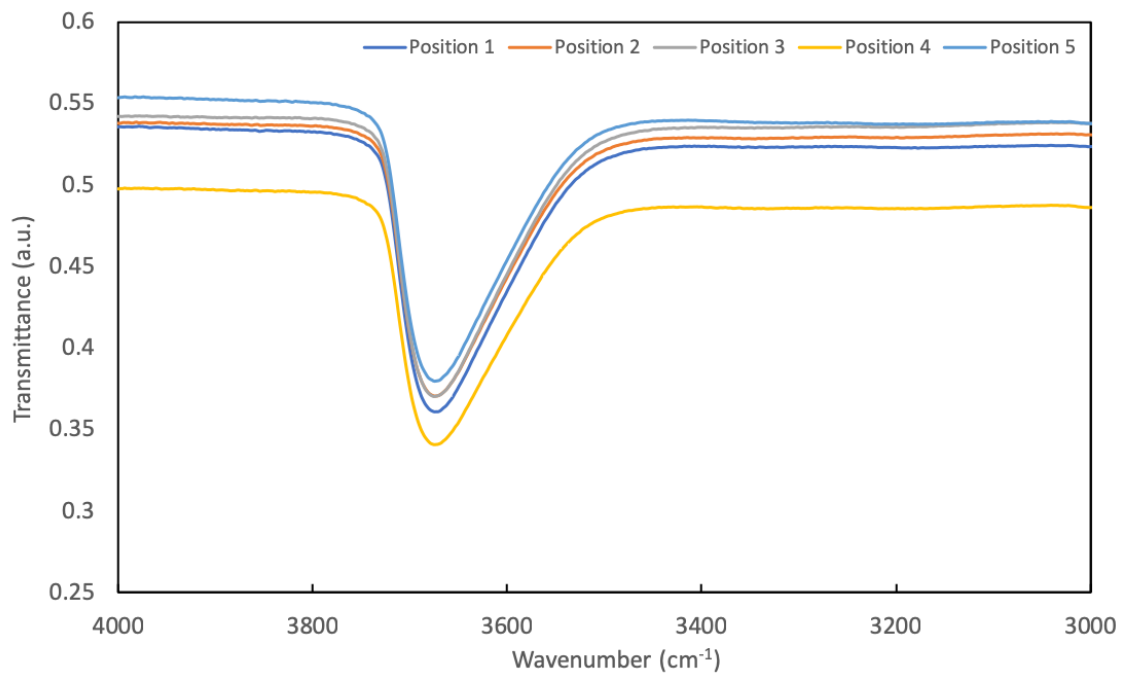


**Figure A.1** The transmittance at different measured positions (shown in Figure 3.8) of sample 600-01(1)

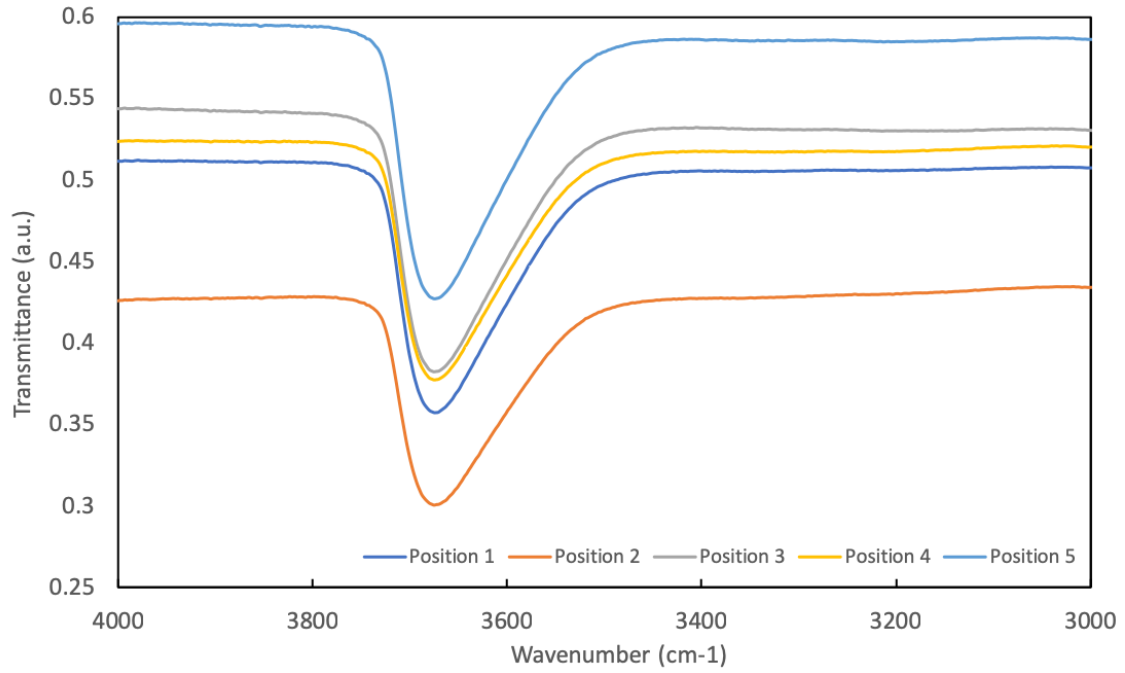


**Figure A.2** The transmittance at different measured positions (shown in Figure 3.8) of sample 600-01(2)

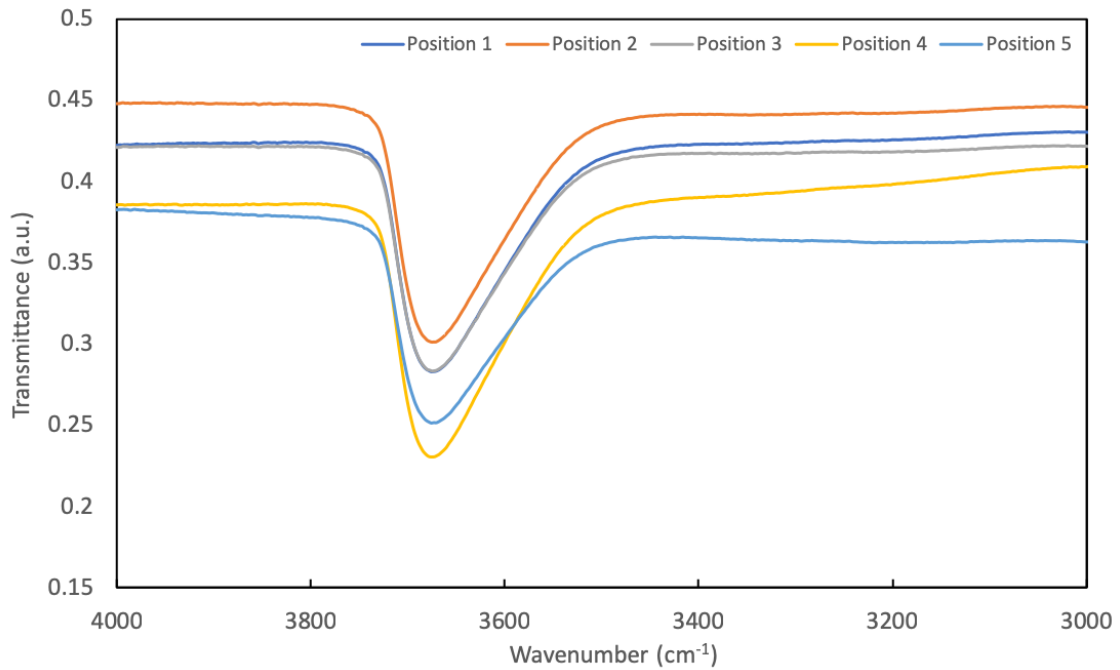


**Figure A.3** The transmittance at different measured positions (shown in Figure 3.8) of sample 600-01(3)

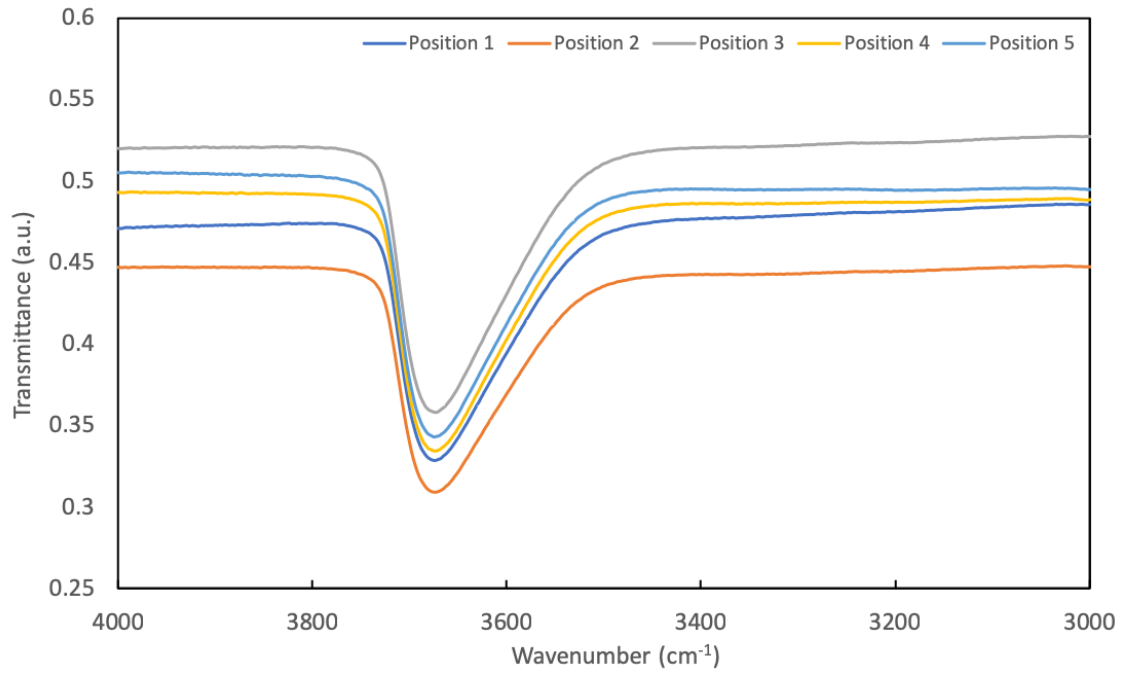


**Figure A.4** The transmittance at different measured positions (shown in Figure 3.8) of sample 900-01(2)

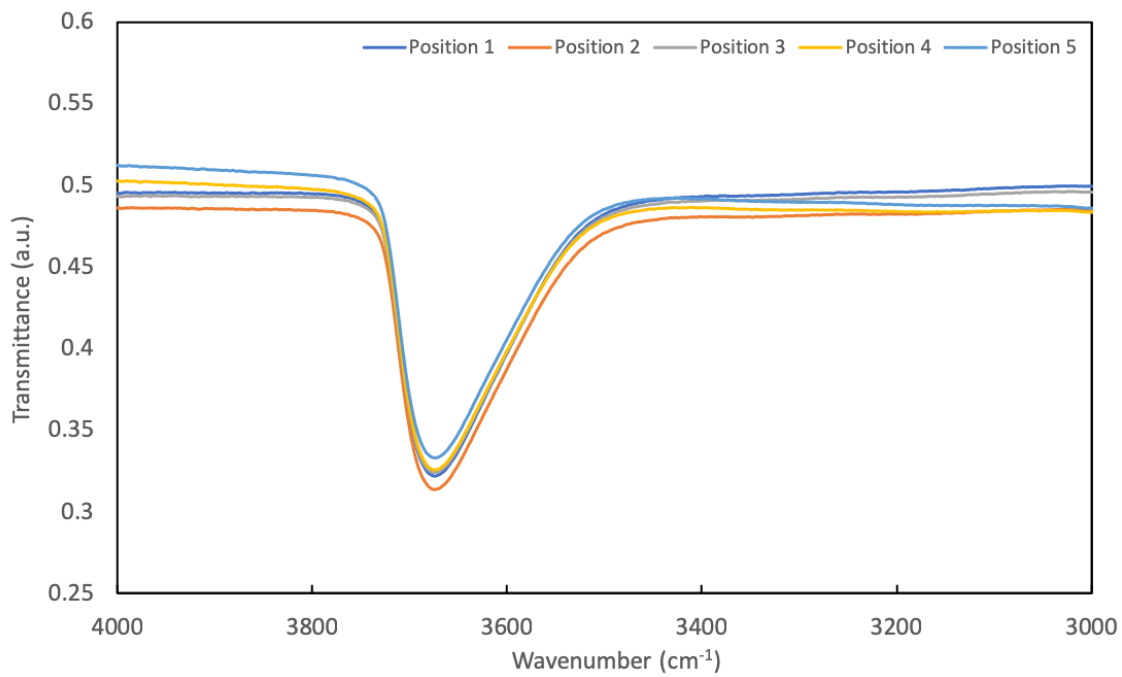


**Figure A.5** The transmittance at different measured positions (shown in Figure 3.8) of sample 900-01(3)

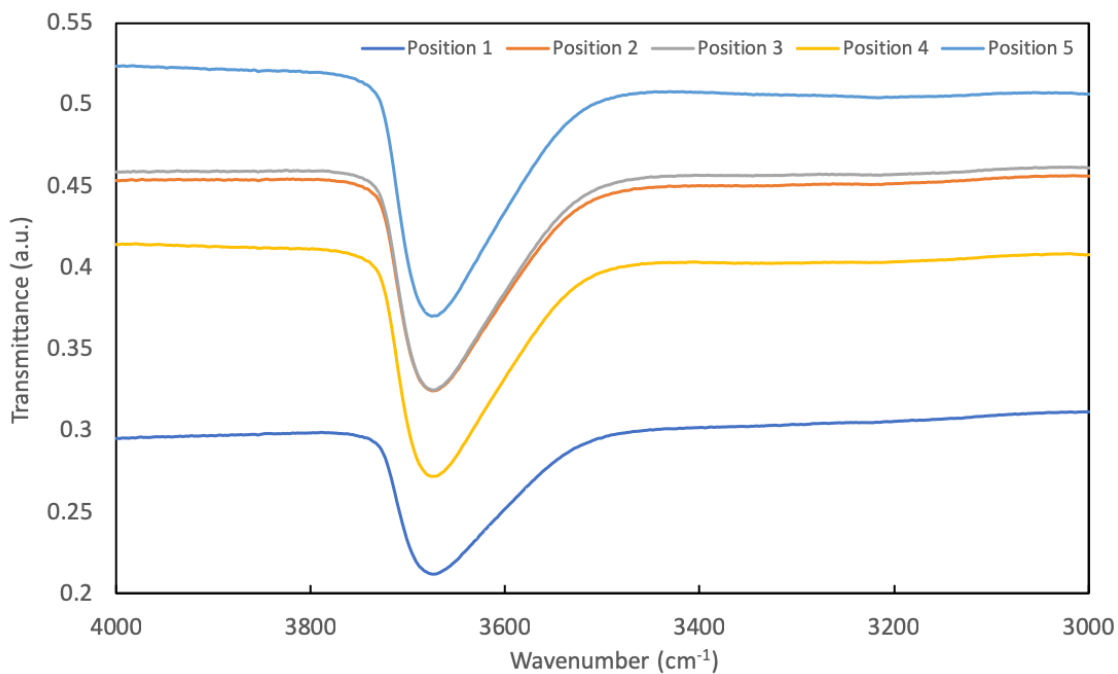


**Figure A.6** The transmittance at different measured positions (shown in Figure 3.8) of sample 900-24(1)

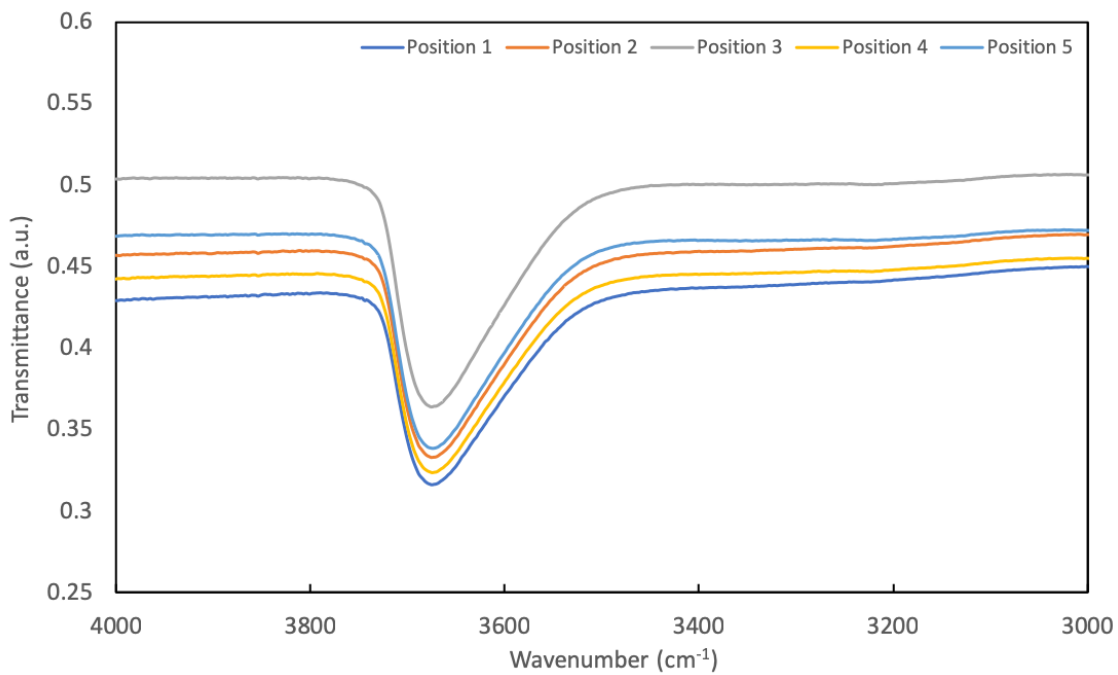


**Figure A.7** The transmittance at different measured positions (shown in Figure 3.8) of sample 900-24(2)

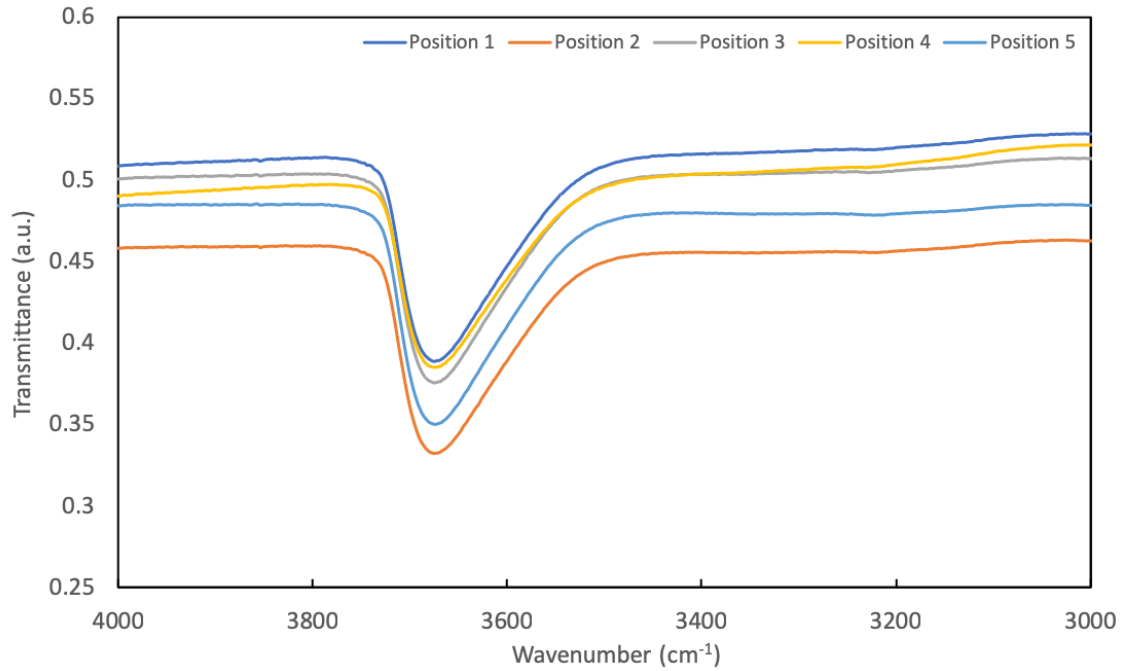


**Figure A.8** The transmittance at different measured positions (shown in Figure 3.8) of sample 900-24(3)

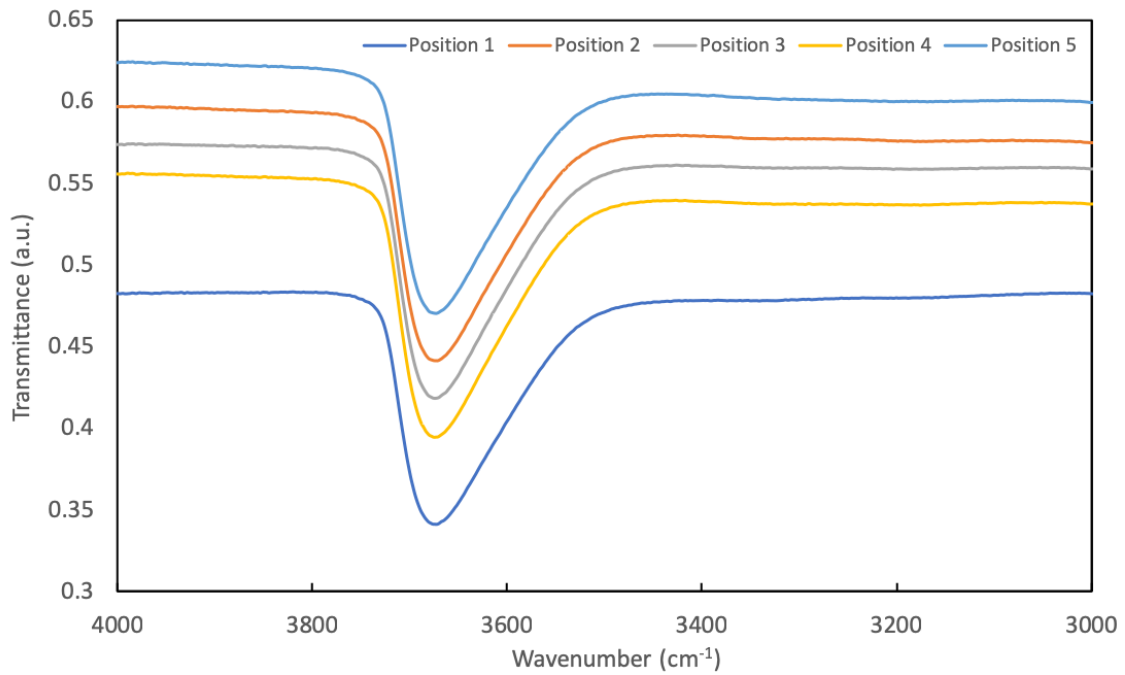


**Figure A.9** The transmittance at different measured positions (shown in Figure 3.8) of sample 1100-01(1)

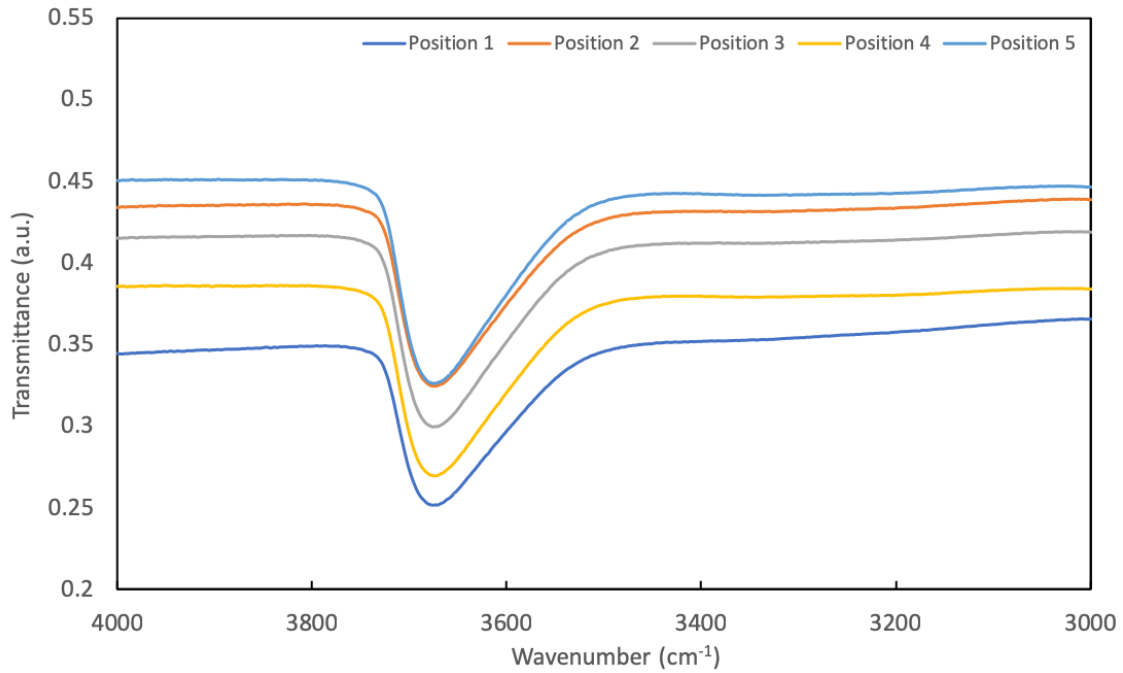


**Figure A.10** The transmittance at different measured positions (shown in Figure 3.8) of sample 1100-01(2)

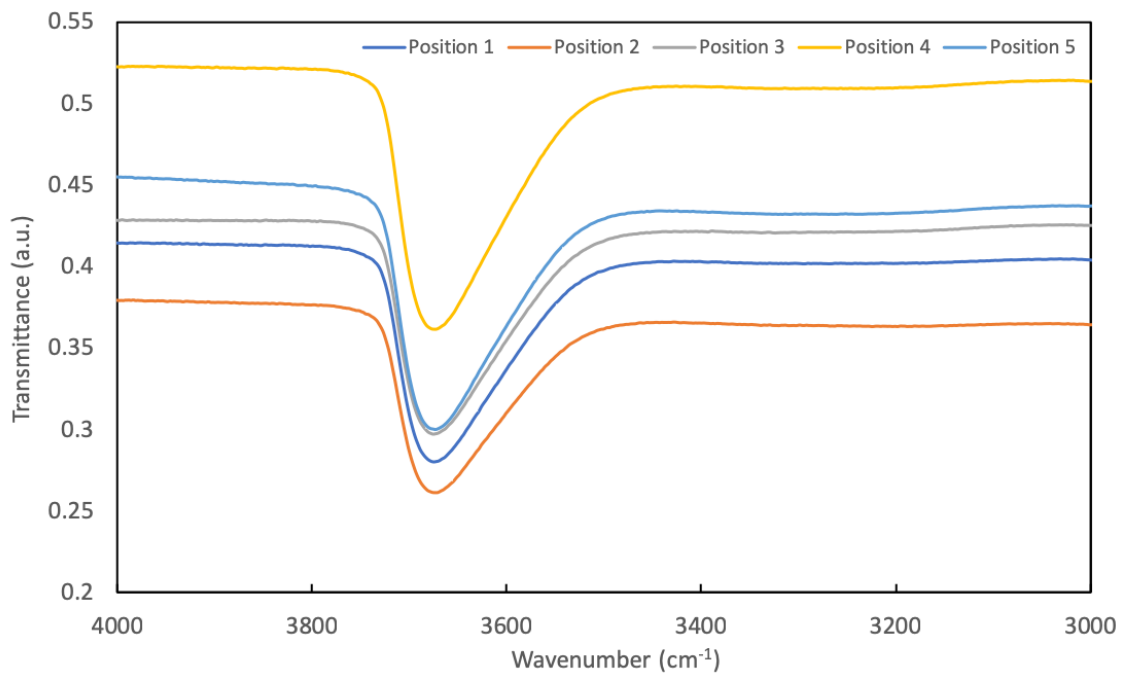


**Figure A.11** The transmittance at different measured positions (shown in Figure 3.8) of sample 1100-01(3)

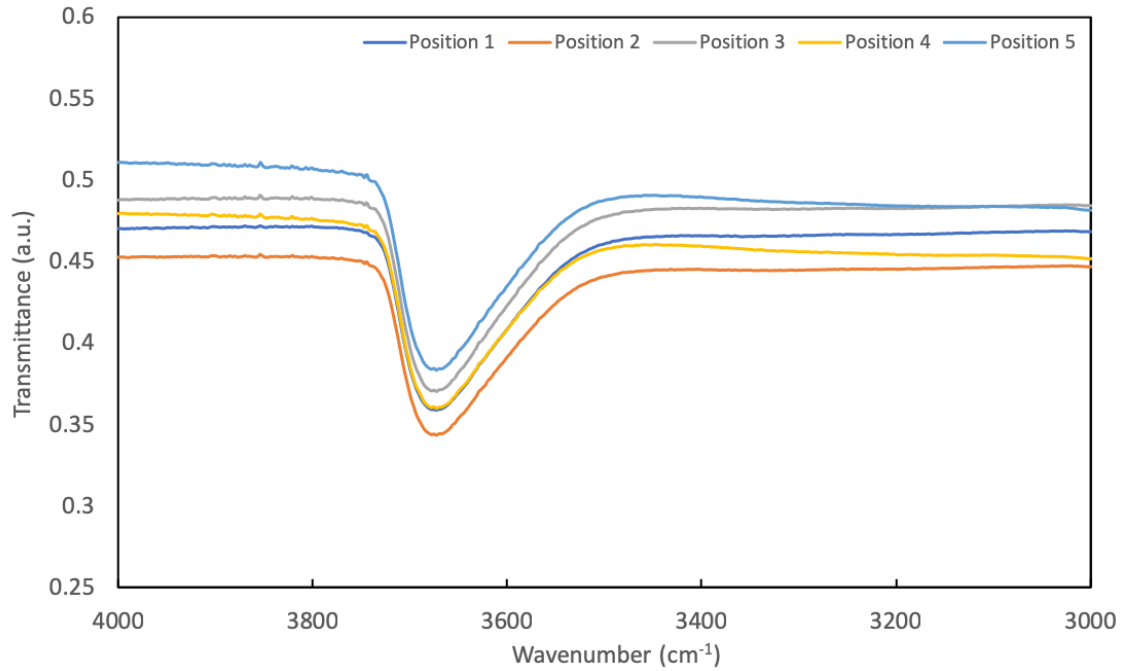


**Figure A.12** The transmittance at different measured positions (shown in Figure 3.8) of sample 1100-24(1)

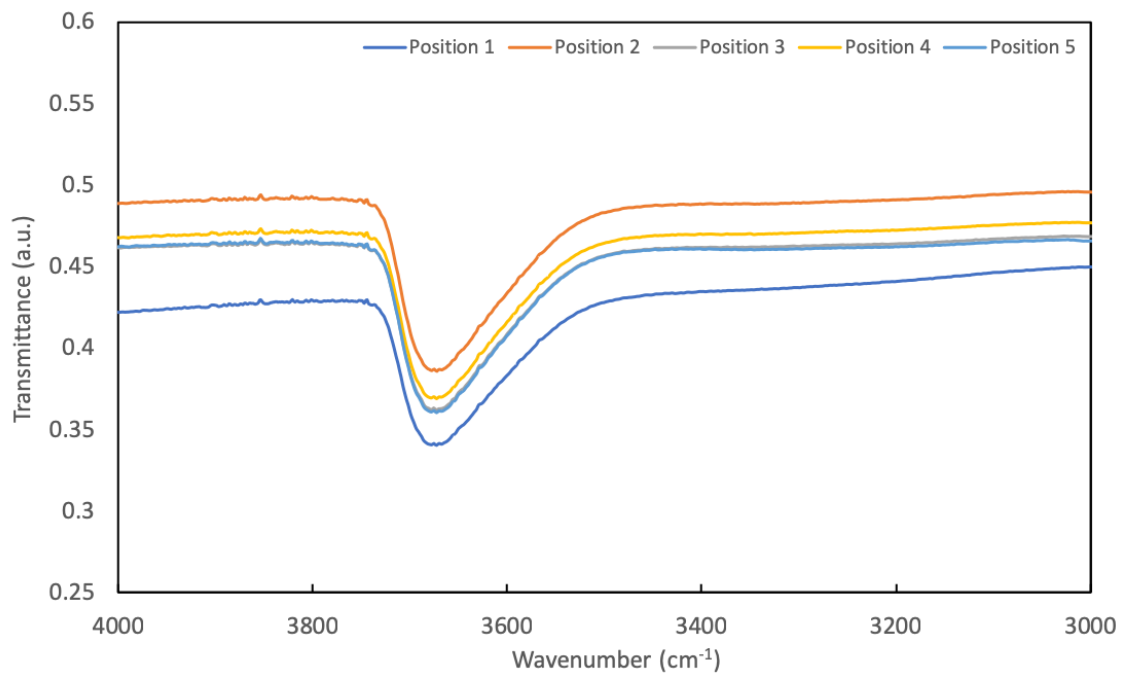


**Figure A.13** The transmittance at different measured positions (shown in Figure 3.8) of sample 1100-24(2)



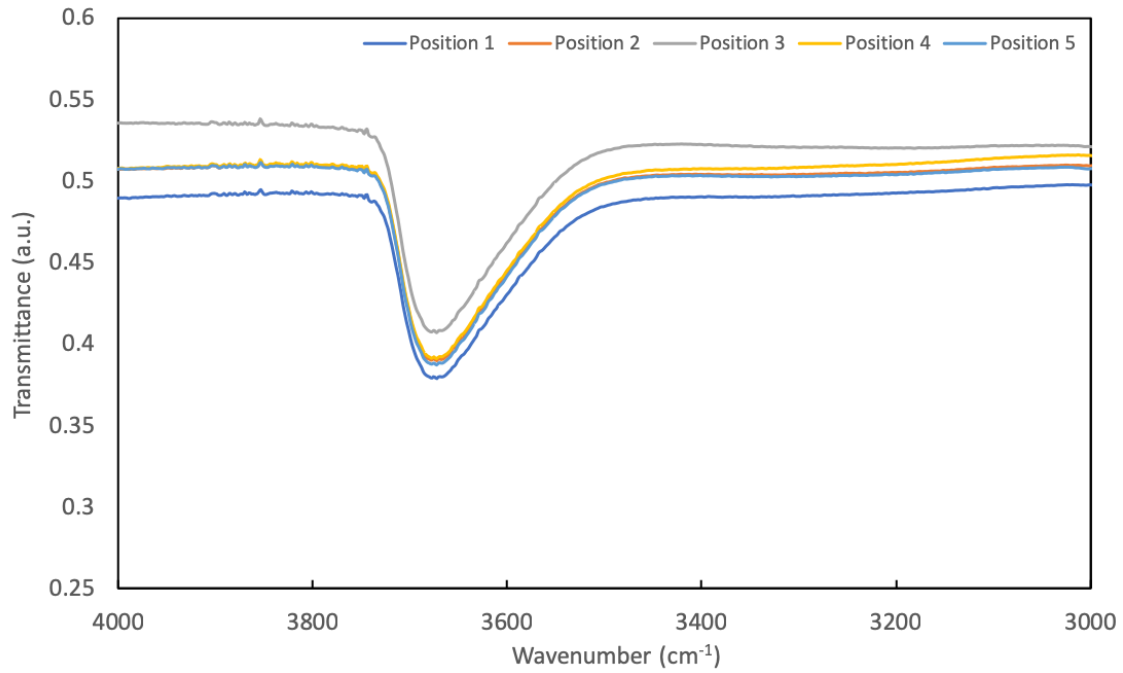


**Figure A.14** The transmittance at different measured positions (shown in Figure 3.8) of sample 1100-24(3)

### A.3 The measured loadings for each viscosity measurement

**Table A.1** Loadings for each viscosity measurement

Fused silica samples	100-24		600-01		900-01		900-24		1100-01		1100-24	
	#1	#2	#1	#2	#1	#2	#1	#2	#1	#2	#1	#2
<b>Loading (N)</b>	4.09	4.11	4.11	4.09	4.10	4.09	4.10	4.10	4.10	4.09	4.10	4.10

**A.4 3D images of bubbles in a volume of  $1.8 \times 1.8 \times 1.8 \text{ mm}^3$  at a corner on XY plane**

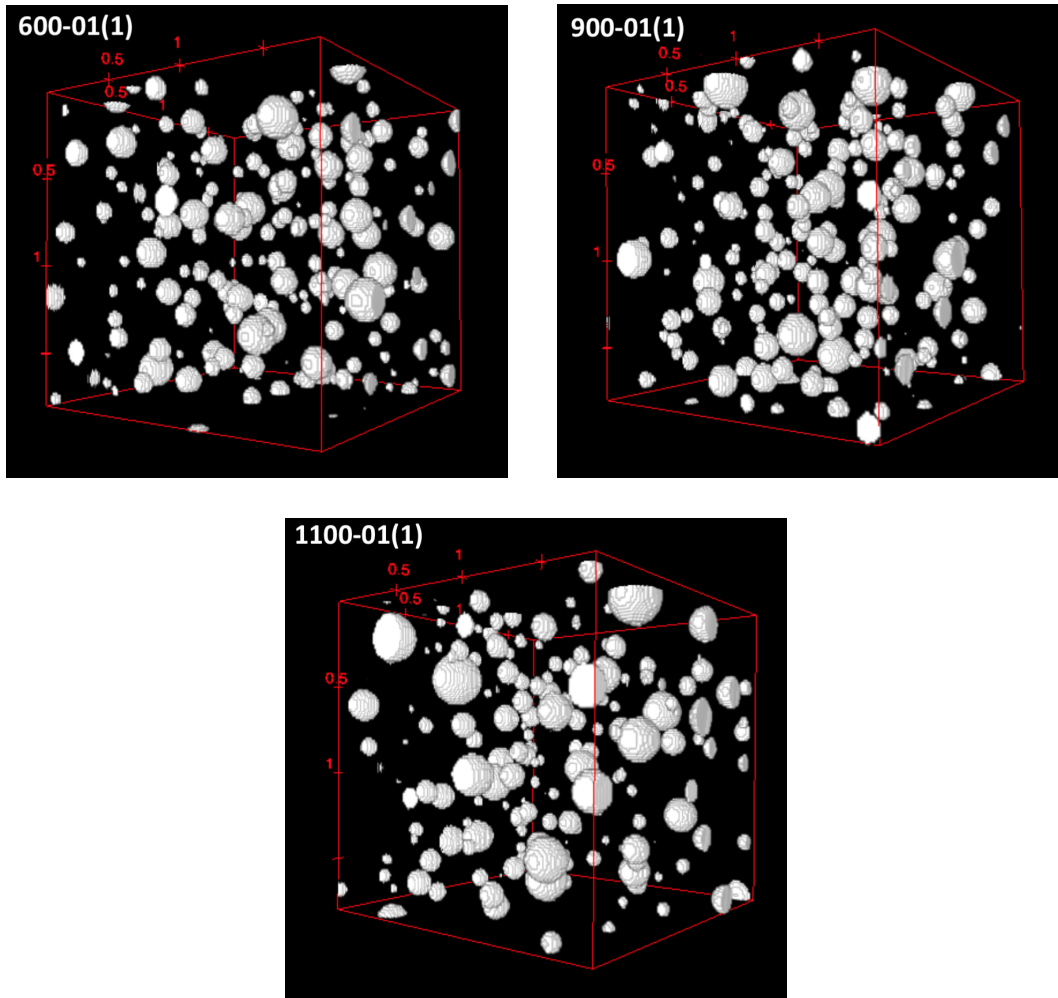


**Figure A.15** 3D view of the entrapped bubbles in a volume of  $1.8 \times 1.8 \times 1.8 \text{ mm}^3$

## A.5 Viscosities and OH contents in commercial fused silica crucibles provided by TQC

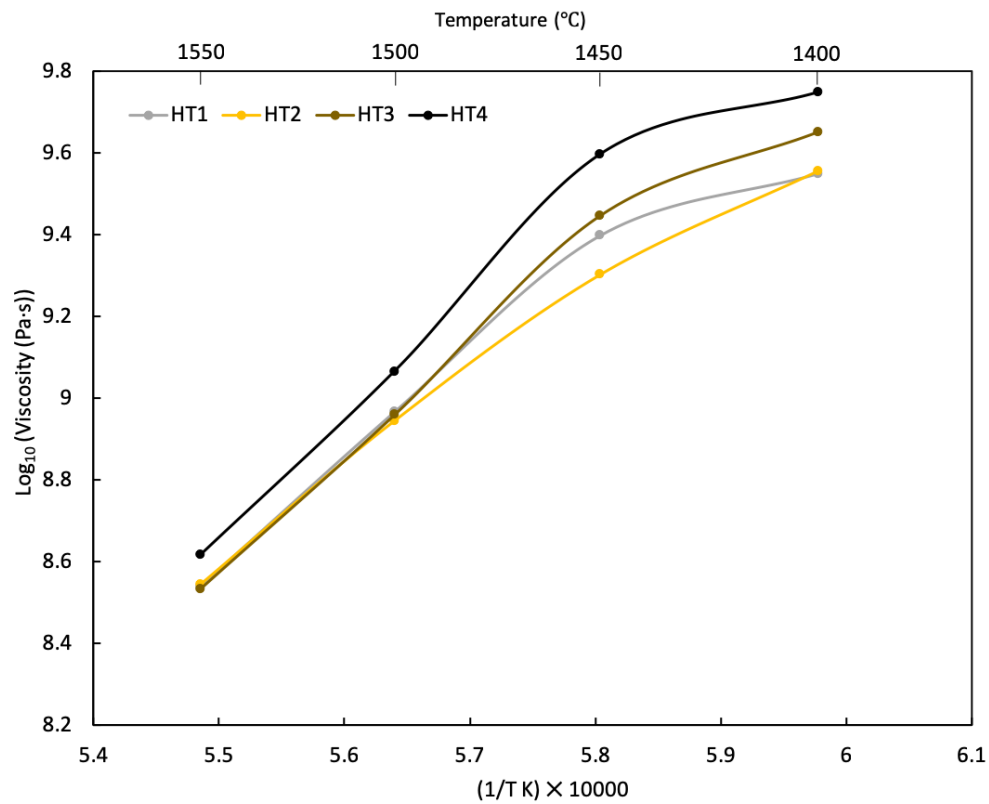


**Figure A.16** The viscosities of commercial fused silica crucibles that were heat treated at different temperatures, provided by TQC. HT1 and HT4 represent the lowest and highest temperature respectively [25]

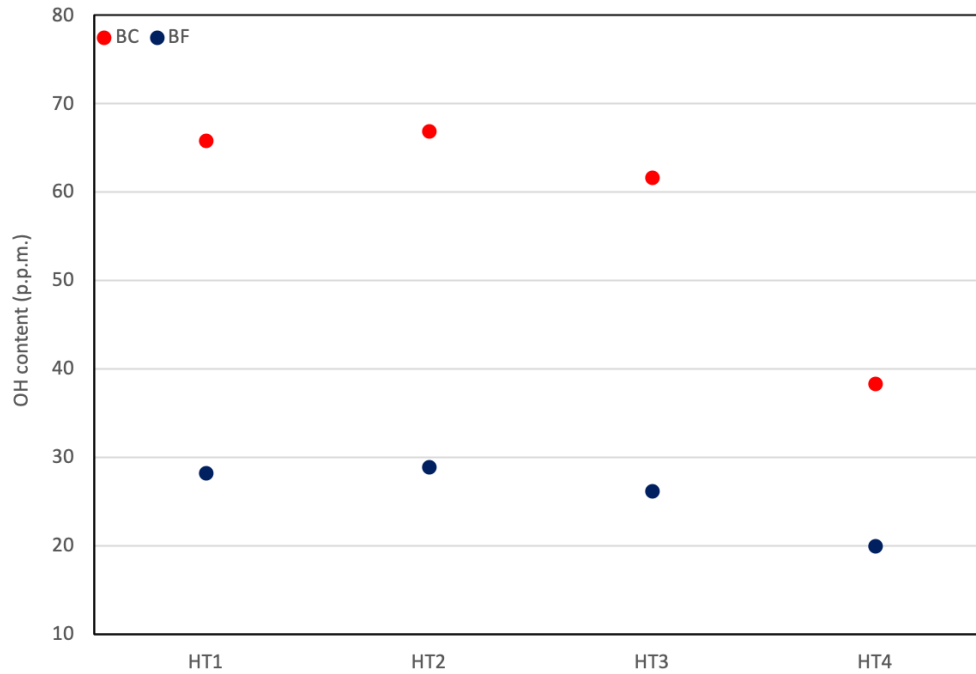


**Figure A.17** The OH contents in some commercial fused silica crucibles that were heat treated at different temperatures, provided by TQC. BC and BF represent the OH contents in bubble-composite and bubble-free layer respectively. HT1 and HT4 represent the lowest and highest temperature respectively [25]

**Table A.2** Summary of the OH contents in commercial crucibles provided by TQC. BC and BF represent the OH contents in bubble-composite and bubble-free layer respectively. HT1 and HT4 represent the lowest and highest temperature respectively [25]

Quartz sand	New (ppm)			Used (ppm)		
	BC	BF	Total	BC	BF	Total
HT1	37.7	28.2	<b>65.9</b>	9.3	14.6	<b>23.9</b>
HT2	38.0	29.0	<b>67.0</b>	2.9	17.6	<b>20.5</b>
HT3	35.5	26.2	<b>61.7</b>	-	-	-
HT4	18.3	20.0	<b>38.3</b>	-	-	-